CONNECTING CORONAL HOLES AND OPEN MAGNETIC FLUX THROUGH OBSERVATION AND MODELS OF SOLAR CYCLES 23 AND 24

by

Christopher Alan Lowder

A dissertation submitted in partial fulfillment
of the requirements for the degree

of

Doctor of Philosophy

in

Physics

MONTANA STATE UNIVERSITY
Bozeman, Montana

July 2015

DEDICATION

To Sara, who has followed our mutual center of mass system, wherever it may wander about this strange world...

ACKNOWLEDGEMENTS

To my advisors, Jiong Qiu and Robert Leamon, I extend my absolute gratitude. Every step of this path through my graduate work was supported by their advice and encouragement.

The entire department of physics at Montana State University has been a constantly supportive and engaging community throughout my work as a graduate student. I extend particular thanks to Dana Longcope and Richard Canfield for discussion of this project throughout the design and implementation. Data use from the SDO, STEREO, and SOHO missions, along with several additional datasets in the text proved crucial in this work.

This work was supported by the NASA Living with a Star (LWS) program.

TABLE OF CONTENTS

TABLE OF CONTENTS – CONTINUED

LIST OF TABLES

LIST OF FIGURES

LIST OF FIGURES – CONTINUED

LIST OF FIGURES – CONTINUED

Figure Page

LIST OF FIGURES – CONTINUED

LIST OF FIGURES – CONTINUED

LIST OF FIGURES – CONTINUED

LIST OF FIGURES – CONTINUED

LIST OF FIGURES – CONTINUED

ABSTRACT

Coronal holes are regions of the Sun's surface that map the footprints of open magnetic field lines as they extend into the corona and beyond, into the heliosphere. Mapping their footprint 'dance' throughout the solar cycle is crucial for understanding this open field contribution to space weather. Coronal holes provide just this proxy.

Using a combination of SOHO:EIT, SDO:AIA, and STEREO:EUVI A/B extreme ultraviolet (EUV) observations from 1996-2014, coronal holes can be automatically detected and characterized throughout this span, enabling long-term solar-cycle-timescale study. I have developed a routine to enable automated computer recognition of coronal hole boundaries from these EUV data. The combination of SDO:AIA and STEREO:EUVI A/B data provides a new viewpoint on understanding coronal holes. As the two STEREO spacecraft drift ahead of and behind the Earth in their orbits, respectively, they are able to peek 'around the corner', providing the ability to image nearly the entire solar atmosphere in EUV wavelengths, using SDO data in conjunction.

On the far-side of the Sun, evolving open magnetic field structures impact space weather, despite being un-observable until rotating into view by Earth. By combining our numerical models of solar magnetic field evolution with coronal hole observations, comparison of far-side dynamics becomes possible. Model constraints and boundary conditions are more easily fine-tuned with these global observations.

Long-term and transient coronal holes both play an important role as observational signatures of open magnetic field. Understanding the dynamics of boundary changes and distribution throughout the solar cycle yields important insight into connecting models of open magnetic field.

INTRODUCTION

Since ancient times, astronomers have glanced at the sun and pondered the nature and role it played in the context of humanity. These early observations were clearly not quite of the consistency or scale that we now possess. However, that spirit of early discovery and understanding still drives this field to this day.

For the majority of human history, the sun has been seen via the naked eye as a bright fireball in the sky. Occasionally, this disc would be peppered with series of dark spots, sometimes large enough to be visible without telescopic magnification. Spanning from the pages of mythology to more detailed scientific consideration, the sun has played a crucial and central role in human history.

Solar Structure and Background

Modern technological advances have pushed our observational powers forward, beyond mapping out these curious sunspots by hand on parchment. With the addition of large ground-based and even space-based observatories, our ability to view the sun in a variety of wavelengths has expanded quite quickly. Under the lens of these additional wavelengths of light, a much more complex picture emerged of the structure of our sun. Below the visible surface of the sun, seismic measurements allow study of the internal structure. Above the surface, the atmosphere reveals itself as a complex and dynamic set of structures and phenomena. At the surface, through measurements

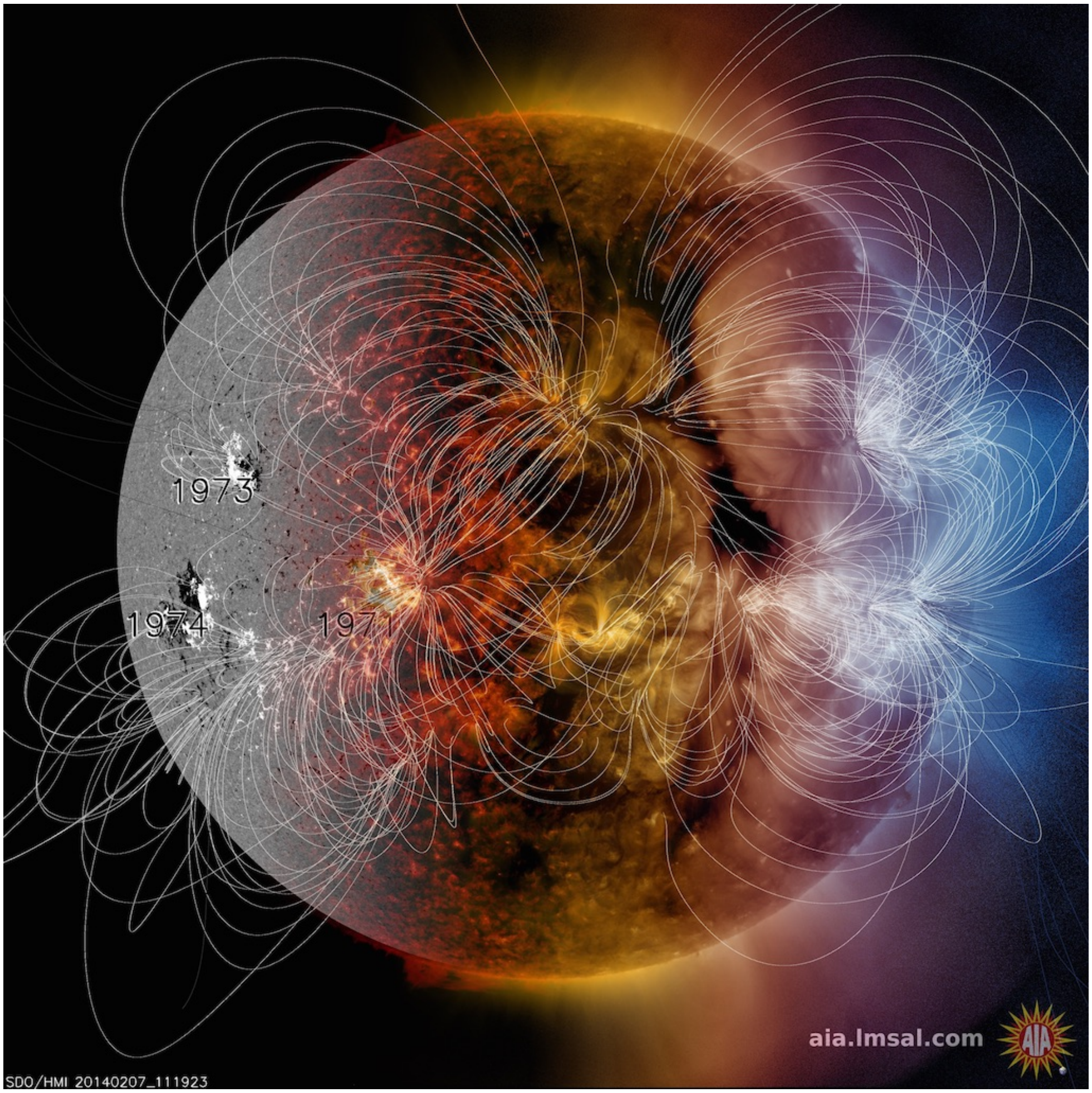

Figure 1.1. A composite image assembled from *SDO*/HMI and *SDO*/AIA data. From left to right, HMI LOS magnetic field, AIA 304Å, 171Å, 193Å, 211Å, and 335Å. A calculated potential magnetic field solution is plotted above each image as a series of field lines.

of the Zeeman effect, even invisible magnetic field lines can be measured and studied. Observation of complex structure and dynamics above the surface are linked to and governed by magnetic fields generated from below.

Our sun, while being a gravitationally bound sphere of material, contains a myriad of internal and external structure and dynamics. The photosphere, an opaque layer, defines the visible ‘surface’ of the sun. Below this, temperature and pressure begins to rise, until reaching the core at the center of our star. Here, these intense temperatures and pressures allow for fusion processes to generate heat to balance this internal gravitational pressure. This heat is radiated outward, through the interior of the sun. As we now rise back out towards the photosphere, these radiative processes give way to convection, generating large scale plasma motion.

These internal plasma motions generate magnetic fields within the interior of the sun. Within the interior, the plasma density is quite high. The resulting plasma pressure from this high density relatively outweighs the magnetic field pressure. The plasma beta,

$$\beta = \frac{8\pi p}{B^2}, \tag{1.1}$$

gives a measure of the relative ratio between plasma pressure, p, and magnetic pressure. Within the interior, this plasma beta is relatively high. As a result, magnetic fields are driven by the motion of plasma. These lines of magnetic field are then transported, twisted, and stretched by internal motion of plasma.

Looking above the photosphere we find the chromosphere, transition region, and eventually the solar corona. Within the corona, densities have dropped off significantly as compared with beneath the photosphere. The resulting plasma beta is then quite low, with magnetic field driving the motion of plasma.

At the transition between solar interior and exterior, magnetic fields extend outward and pierce through the photosphere. At these points of extension, reduced visible wavelength emission results in dark patches at the photosphere. These dark patches are sunspots, and rotate and evolve with the surface motions of solar plasma. These visible phenomena are the manifestation of more complex magnetic activity.

Figure 1.1 displays a composite image of a series of concurrent solar observations. From measurements of magnetic field at the photosphere to high-temperature coronal plasma emitting in the extreme ultraviolet, the complexity of connecting these observations is certainly a challenge. Temperatures within these observations range from 50,000 K to 2×10^7 K, while traced magnetic field lines scale from the solar surface at one solar radius (1 $R_\odot$), all of the way out to 2.5 $R_\odot$. While connecting these myriad observations and drawing physical conclusions poses issues, the potential for insight into the mystery of the sun drives the field forward.

The Solar Activity Cycle

While early efforts at systematically cataloging the range of solar activity were somewhat smaller in scale than modern efforts, they provide a rich history for mining the prior activity of our local star. Modern observations only span a very limited range of time, especially in comparison with the variation of time-scales observed in the sun. Thus, to more fully understand the evolution and patterns of solar activity, delving back into historical observations proves crucial.

Despite the complexity of the solar atmosphere, observational signatures in visible light reveal very little. Regions of enhanced magnetic activity near the visible photosphere reveal themselves in visible light via the appearance of sunspots. These regions provide one useful observational signature of solar activity. Luckily, with even early telescopic assistance, these regions posed a curious problem for early astronomers to observe and characterize.

Some of the earliest sunspot observations date back to Theophrastus of Athens in 325 BC, who noted the appearance of dark spots on the sun. Chinese astronomers began methodically observing sunspots as early as 23 BC (Priest, 2014). In the western part of the world, Brother John of Worcester in 1128 noted the existence of these sunspot features. Later, more detailed, observations by Schwabe (1844), spanning 1826 to 1843, revealed that the number of these sunspot features appeared to oscillate in number over the course of years, with roughly an eleven year cycle.

By ‘connecting the spots,’ so to speak, the number of these sunspot features grow to a maximum, and then begin a decline back towards a minimum, to begin this cycle anew.

Later observations by Hale (1908) suggested that these sunspot regions were in fact the visible light signatures of regions of strong solar magnetic field. Subsequent detailed observations led to the discovery that these sunspot regions, while potentially magnetically complex, retained some aspect of a positive and negative magnetic pole. In the simplest bipolar sunspot configuration, one sunspot contains magnetic field emerging from the photosphere, while an opposite adjacent sunspot contains field descending into the photosphere. Detailed observations of these sunspot pairs revealed that this polarity followed a hemispheric trend, with one orientation of leading sunspot magnetic polarity in the northern hemisphere, with the opposite in the south. This hemispheric trend was also observed to reverse itself following the 11 year sunspot number cycle (Hale et al., 1919).

Thus, while the number of sunspots undergoes an 11 year cycle, the existence of this polarity reversal extends the magnetic solar activity cycle to a full 22 year cycle to return to the original hemispheric polarity trend. Figure 1.2 displays the smoothed hemispheric sunspot number in a series of observations spanning the range 1992 to 2014. Red denotes the northern hemisphere, with blue counting the south. The area between these two curves is shaded to denote the hemisphere.

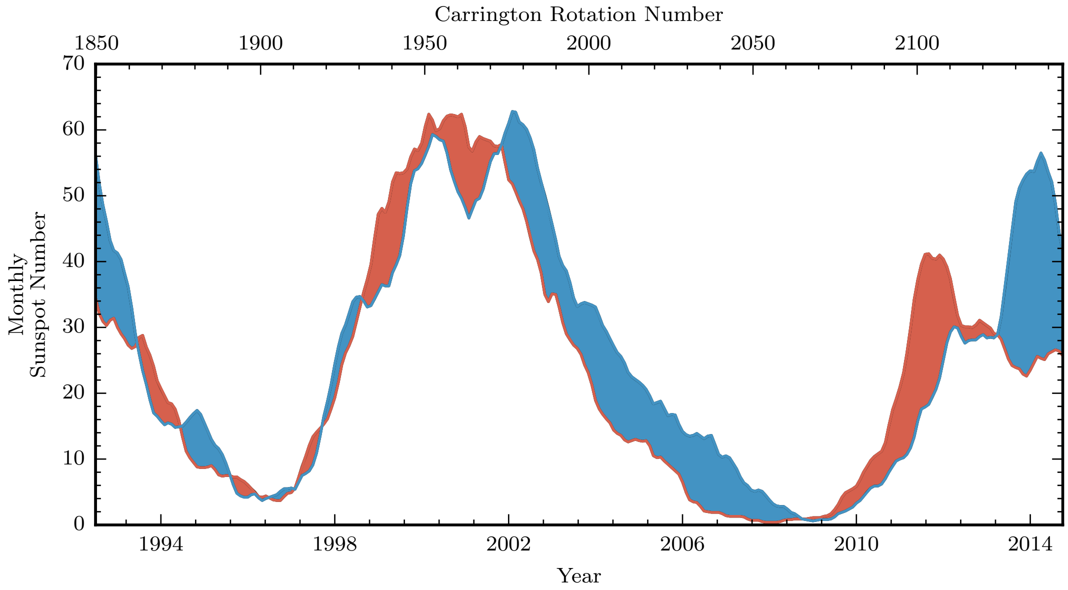

Figure 1.2. Hemispheric sunspot number for northern and southern hemispheres in red and blue, respectively. (WDC-SILSO, Royal Observatory of Belgium, Brussels)

While the variation in the hemispheric sunspot count seems a simple diagnostic of the solar activity cycle, a large degree of detail varies from cycle to cycle. Some cycles are more magnetically active than others, with some spans of time having hardly any solar activity (Maunder, 1904). In addition, a large number of tertiary physical observables follow this overall magnetic activity cycle, observable both on the sun and in-situ as space weather. These range from the total solar irradiance, properties of the photospheric magnetic field, solar wind speed, cosmic ray flux, and a variety of other observables. Coronal holes are one such consequence of this cycle, waxing, waning, and repositioning themselves throughout the course of evolution through the solar activity cycle.

Coronal Holes

Extreme ultraviolet (EUV) observations of the corona, the outermost layer of the solar atmosphere, first shed light onto the subject of coronal holes. Here, and in these wavelengths, coronal holes were discovered to appear as dark patches (Tousey et al., 1968). Later observations discovered these features in x-ray wavelengths as well. These dark patches correspond with the location of open magnetic field as it extends outward from the photosphere into the heliosphere. Unlike the closed magnetic field lines connecting portions within active regions and the quiet sun, these field lines are open directly into the heliosphere. Plasma in the solar corona lying along these open magnetic field lines is free to move outward along these field lines, creating the solar wind and leaving behind a density depletion, and hence a reduced EUV and x-ray emission (Cranmer, 2009).

Considering the multi-wavelength snapshot of the sun in Figure 1.1, coronal holes are apparent in comparison with the other solar features. Magnetic field lines are computed and traced in this figure as solid white lines. While the majority of field lines displayed in this figure are closed, a handful are open. Tracing these open field lines back down to their photospheric origin, note that they are rooted within a dark patch as measured in EUV near the northern pole, a coronal hole.

As coronal holes are tied to the global magnetism of the sun, they too vary over the course of the solar activity cycle. Several studies have considered the evolution of coronal holes through the solar cycle, and the connection with open magnetic field (Harvey & Recely, 2002; Wang, 2009). In particular, Harvey & Recely (2002) considered the properties of polar coronal hole throughout solar cycles 22 and 23, and found this same cyclic variation within polar coronal holes.

With the advances of space-based solar observatory missions, consistent and high-quality EUV data are routinely available, making long-term observations of coronal holes possible. The *Extreme-ultraviolet Imaging Telescope* (EIT; Delaboudinière et al., 1995) has provided nearly continuous EUV observations spanning from 1996 until 2010. Following this instrument was the *Atmospheric Imaging Assembly* (AIA; Lemen et al., 2012), which continues to provide regular EUV images at enhanced resolution and with additional wavelength filters. These instruments alone provide observation of Earth-side coronal holes from 1996 to present (2015), allowing study of one and one-half solar cycles. While these data certainly do not extend back quite as far as sunspot counts, they certainly yield consideration of the most recent cycles.

Petrie & Haislmaier (2013) have studied the global coronal structure, in conjunction with evolution of active regions. Multiple studies have probed the connection between coronal hole properties and the associated solar wind activity. Rotter et al. (2012) find a correlation between peaks in coronal hole area and solar wind speed. Zhao & Landi (2014) have studied the evolution of polar and equatorial coronal holes and their associated solar wind sources, finding each to be a separate source, varying independently during the course of solar cycles 22, 23, and 24. de Toma (2011) consider in more detail the evolution of coronal holes during the solar minimum period between cycles 23 and 24 in detail. They find that low-latitude coronal holes during this period provided a crucial component of the high-speed solar wind. As these holes decayed away as the cycle progressed, changes in the source of the fast solar wind resulted. Neugebauer et al. (2002) have used Ulysses data, outside of the plane of more traditional observations, to study the higher latitude sources of solar wind. Comparison with coronal holes provided confirmation of these wind sources. Modeling efforts by Antiochos et al. (2011) have sought to connect sources of the solar wind to their coronal hole sources.

To further enhance study of coronal holes, the *Extreme Ultraviolet Imager* (EUVI; Howard et al., 2008) instruments allow a unique perspective. Launched on two spacecraft on orbits drifting 'ahead' and 'behind' of Earth, they extend not only continuous far-side observations of coronal holes, but also enhanced coverage of the polar regions of the sun throughout solar cycle 24.

By combining these observations, coronal holes provide a unique puzzle piece for deciphering the causes and properties of the solar magnetic activity cycle.

Coronal Field Modeling

As coronal holes map out the boundaries of open magnetic field, they provide an observational signature with which to constrain global coronal field models. Determining the structure of open magnetic field is critical, as a source of the fast solar wind and as a measure of the total flux open to the heliosphere.

At the present moment, consistent and reliable measurements of the coronal magnetic field are not available. Our knowledge of the coronal magnetic field is driven by models, using direct measurements of the photospheric magnetic field as input boundary conditions, with various model assumptions and compromises. The MDI and HMI missions have provided extraordinary full-disc magnetogram datasets, spanning two decades. However, these measurements are limited to the Earth-side of the sun at any particular moment. Evolution of the open-closed topology of the global corona can be greatly aided by coronal hole measurements to constrain and adjust these driving models.

Potential Field Source Surface (PFSS) Model

The potential field source surface (PFSS) models are most commonly used to describe the global magnetic field. This class of models employs two surfaces at the bottom and top boundaries, and computes the magnetic field in-between these two surfaces. The bottom boundary is at the photosphere, and the measured longitudinal component of the photospheric magnetic field is used as the boundary condition. The top surface, called the source surface, is set at a few solar radii from the solar center; at this source surface, it is assumed that magnetic field is purely radial. Between these two surfaces, the field is assumed to have no electric current. This field must then satisfy,

$$\nabla \times \mathbf{B} = 0, \tag{1.2}$$

and thus the magnetic field can be expressed as a function of a scalar potential,

$$\mathbf{B} = -\nabla \Phi_M. \tag{1.3}$$

Regardless of model assumptions, the divergence of the magnetic field must be zero,

$$\nabla \cdot \mathbf{B} = 0. \tag{1.4}$$

With this, the scalar potential must then satisfy Laplace's equation,

$$\nabla^2 \Phi_M = 0. \tag{1.5}$$

This solution then provides a potential magnetic field within this domain (Schatten et al., 1969; Wang & Sheeley, 1992). While these assumptions and simplifications do somewhat limit these models, they do provide fairly accurate snapshots of the global coronal field topology. While useful as a series of snapshots in the evolution of the coronal field, they do not always provide an accurate picture of the dynamics of this coronal field evolution.

The model employed for this work uses a synoptic magnetogram of photospheric magnetic field. These maps are gathered using slices of magnetic field measurements, a few degrees about the Earth-facing central heliospheric longitude. These slices are then stacked over the course of a solar rotation, 27.2753 days, building a map of photospheric magnetic field over the course of a rotation. This methodology does introduce the potential for magnetic field information that can be up to one rotation out-of-date. The upper boundary in this model, the source surface, is a variable in this model. This value can be best matched via a variety of methods, from coronal hole boundaries, to white light corona images, all the way out to IMF measurements of the resulting heliospheric magnetic field. The value 2.5 $R_\odot$ is most commonly used, calculated by Hoeksema et al. (1983).

Comparisons have been made between model computed open-field boundaries and observational coronal hole boundaries (Wang et al., 1996). Most studies conclude that computed open field and observed coronal hole boundaries are in reasonable agreement within the polar regions. Low-latitudes are where most discrepancies crop up in these comparative efforts.

The manual or computational comparison of boundaries over any reasonable time-span is a significant effort. Reducing this comparison to a single qualitative factor for comparison allows for a much faster and long-spanning comparison, at the loss of spatial information. For instance, the total unsigned open magnetic flux, or the total coronal hole enclosed flux, can be compared with in-situ measurements of magnetic field data at Earth. These data consist of a time-series of data at a single point in space. For comparison with total open magnetic flux, the uniformity of the magnetic field magnitude across a sphere of radius 1 AU is assumed.

Much of the criticism of the PFSS model focuses on the two major assumptions of the model. The observationally-based photospheric boundary condition of the model does lead to out-dated information, as the far-side of the sun is not directly observable via magnetic field data. In addition, the lack of current within the corona is not accurate by any means. Solutions exist to address some of these problems, outlined in the sections below. To solve the first criticism, flux transport models can be employed to model the evolution of the far-side of the sun. To address the second criticism, non-potential models of magnetic field have been developed. Full-Magnetohydrodynamic (MHD) simulations are also an available avenue of consideration, however, the computational constraints make extensive high-resolution models unfeasible for time-spans more than a few rotations.

Non-Potential Models

Non-potential models, in particular nonlinear force-free field models attempt to better match observational constraints, in particular through the addition of electric current in the space above the photosphere. Force-free magnetic field models allow for the introduction of an electric current, such that a zero Lorentz force is demanded,

$$\mathbf{j} \times \mathbf{B} = 0. \tag{1.6}$$

Evolving a coronal field through a series of these force-free equilibria allows a similar look at the global field topology(van Ballegooijen et al., 2000; Yeates et al., 2010). However, here, some of the major problems with the potential model have been addressed. A flux transport model is employed to evolve the photospheric boundary field, yielding a more accurate picture of the far-side of the sun. The addition of current also more accurately describes the true physics of the corona. Here, in addition, a more detailed look is possible at the dynamics of coronal evolution. Eruptive events and other more dynamic processes are now possible to compute and compare.

Flux Transport Models

For any of these models, boundary conditions are crucial. To constrain the photospheric magnetic field, synoptic observations can provide a time-lagged snapshot over one solar rotation. However, to capture the dynamics of the evolution of the far-side magnetic field, a flux transport model is required to drive these un-observed fields forward. This surface magnetic field is most often driven forward by several processes. A diffusion term acts to decay away spatial gradients in magnetic field strength. In addition, a surface velocity field acts on these magnetic field elements, with a latitudinal and longitudinal component. By evolving magnetic field elements, and updating the Earth-side with either pure or characterized observations, a reasonably accurate picture of the far-side evolution is possible (Yeates et al., 2007). Within the scope of variable parameters within a flux transport model, Baumann et al. (2004) considered the effect of surface flow and diffusion on the global coronal magnetic field, confirming these as primary 'knobs' to control model field evolution. An earlier result from (Wang et al., 2002) confirmed that the meridional flow (latitudinal component of the surface flow) varying from one solar cycle to the next allowed for a better matching of total open magnetic flux. For many of these models, a potential or non-potential model is then used to compute a coronal field from this evolving boundary condition.

An Overview of the Problem at Hand

Numerical modeling has been the only approach to provide truly global magnetic field configurations within the corona and inner heliosphere. Space weather forecasts, in particular, rely heavily on these model outputs. Configuration and evolution of open magnetic field plays a major role in these efforts. Pinning down this parameter is of critical importance.

Single-point measurements of open magnetic flux, such as those contained in the OMNI database, are a simple tool for the comparison of total open magnetic flux. This dataset is collected from a variety of spacecraft sources, providing an in-situ (near-Earth) measurement of the magnetic field at this point in space (King &

Papitashvili, 2005). Assuming that this value at 1 AU is representative in magnitude with the field on a sphere of radius 1 AU from the sun, a total open magnetic flux can be computed. Half of this open field exits this spherical surface, with a presumed equal and opposite flux returning. From this, the total open magnetic flux can be calculated as $\Phi_{OMNI} = 4\pi R_{L1}^2 |B_x|$, taking the component of the magnetic field along the Earth-sun line (Lockwood, 2002). However, these measurements often result in far greater amounts of computed OMNI open magnetic flux than are observed at their photospheric origins (Yeates et al., 2010). This overabundance of open magnetic flux in comparison with models and observations raises some doubt as to the truth of the assumption of a uniform field at this radius. We propose an alternative and independent approach of measurement of the total open magnetic flux through the tracking and characterization of coronal hole boundaries. The consistent EUV full-disc observations from EIT and AIA-EUVI make this an ideal time to conduct this study, with an established database spanning 1.5 solar cycles. The combination of this data provides a comprehensive look that has not yet been fully explored.

In comparison with measurements of open magnetic flux from PFSS models, the static nature of the model must be considered. Boundary conditions for these models are often averaged over the course of one solar rotation, with portions of the surface containing information out of date by days. Eruptive events such as coronal mass ejections (CMEs) and other events (not be captured by the static nature of PFSS model boundary conditions) can contribute towards larger in-situ measurements of open magnetic field (Lepri et al., 2008). As these phenomena commonly originate closer to the solar equator, this motivates the need to further consider the contribution of low-latitude open flux and the contribution towards the total distribution. The OMNI dataset, consisting of a single-point measurement in space, simply cannot provide the spatial detail required for this comparison.

While a handful of studies have considered polar and low-latitude coronal holes and open field separately, most of these studies have not been systematic in the time-spans considered. A handful of rotations are often compared, mostly in a qualitative manner, without sustained and quantitative study over the span of years. Gathering consistent data over the course of multiple solar activity cycles is crucial for deciphering the behavior of these quantities.

Efforts have been made to address the connection between the structure of coronal hole distribution and the evolution of the fast solar wind, especially with regard to low-latitude sources. However, again, consistent and systematic data are needed for detailed comparison.

With these pieces in place, connections begin to form between these avenues of research. Models provide an opportunity to study the sun as a laboratory-in-a-box, being able to adjust parameters and simulate years of solar evolution in a matter of hours. While countless solar models have been run, with data most likely summing up into the range of petabytes, only a subset of these studies have the open magnetic field as a target of interest. As a subset of these studies, even fewer note the distribution of open magnetic field as it is rooted in the photosphere. And as an even smaller subset of this subset, a handful of studies track all of this over the span of a solar cycle (or two).

The research contributing to this dissertation has established a database of coronal hole boundaries, spanning nearly two solar activity cycles. This provides a unique and valuable tool for matching models and observations. The solar cycle dependence of coronal holes are explored here in details not yet considered. Prior to this work, no study has traced the role of both polar and low-latitude coronal holes in connection with modeled open magnetic field over the span of solar cycles. Guided by these new observations of the latitudinal distribution of magnetic open flux, modifications to PFSS and flux transport models lead to new insight into surface flow profiles. In addition, far-side coronal hole observations by multiple spacecraft has improved the coverage and accuracy of the data. With the inclusion of high-cadence data, more stringent constraints can be placed on models.

Connecting coronal hole observations with modeled open magnetic field in this dissertation provides an avenue to advance research of open magnetic field throughout the solar activity cycle.

Chapter 2, Coronal Hole Detection and Open Flux Measurements, lays out the framework for the automated detection of coronal holes. Early measurements from this dataset are presented here. Chapter 3, Coronal Holes and Open Flux in Solar Cycles 23 and 24, updates this dataset to extend further into solar cycle 24. These measurables are explored in more detail, tying the pieces together into a coherent view. Chapter 4, A Flux Transport Model for Computation of Open Magnetic Field, lays the framework for modeling open flux over the span of a solar activity cycle. Model results and extensions are used to connect back with observations of coronal hole enclosed flux, probing at the driving mechanisms behind the structure and evolution of open magnetic field.

CORONAL HOLE DETECTION AND OPEN FLUX MEASUREMENTS

Contribution of Authors and Co–Authors

Manuscript in Chapter 2

Author: Chris Lowder

Contributions: Conceived and implemented study design. Constructed code to analyze data sets. Wrote first draft of the manuscript.

Co–Author: Dr. Jiong Qiu

Contributions: Helped to conceive study. Provided feedback of analysis and comments on drafts of the manuscript.

Co–Author: Dr. Robert Leamon

Contributions: Helped to conceive study. Provided feedback of analysis and comments on drafts of the manuscript.

Co–Author: Dr. Yang Liu

Contributions: Provided access and usage assistance with a dataset in use for this study. Provided feedback on study design.

Manuscript Information Page

Chris Lowder, Jiong Qiu, Robert Leamon, Yang Liu
The Astrophysical Journal
Status of Manuscript:
____Prepared for submission to a peer–reviewed journal
____Officially submitted to a peer–reviewed journal
____Accepted by a peer–reviewed journal
_x_Published in a peer–reviewed journal

Published by the American Astronomical Society
Published February, 2014, ApJ 783, 142

Introduction

Coronal holes are observationally regions of diminished emission in the extreme ultraviolet (EUV) and X-ray wavelengths, as compared to the quiet sun background level. The earliest observations of coronal holes were made in EUV wavelengths. Tousey et al. (1968) noted from spectroheliograms obtained by rocket experiments that EUV emission in polar regions seemed weaker than in surrounding regions. More detailed spectroscopic observations were made possible by instruments onboard Skylab, which yielded some of the early measurements of the chromosphere, transition region, and corona properties in coronal holes (Huber et al., 1974). Coronal holes have since then been observed in many wavelengths from radio, near infrared (He I 10830 line), white-light, to EUV and X-rays both on disk and from the limb; and their properties have been extensively studied, including the temperature, density, flow velocity, energy flux, lifetime, and magnetic fields. Detailed reviews of the plasma and magnetic properties of coronal holes have been given by Zirker (1977); Harvey & Sheeley (1979); Cranmer (2009).

There has been long-standing interest in studying coronal holes because of their association with large scale solar magnetic fields and solar winds. Coronal holes are considered to map regions on the Sun's surface where magnetic field lines are open to the heliosphere (Wang, 2009, and references therein). Simply put, as coronal plasmas and energy flow outward along open magnetic field lines, the coronal density in these regions is decreased, resulting in diminished X-ray and EUV emission. Long-lived coronal holes that exist for days or months are often found in high-latitude regions, such as polar caps. Some of the long-lived coronal holes also extend into low-latitude regions. They are usually associated with fast solar wind in a quasi-steady state, as originally proposed by Parker (1958). In addition to long-lived holes, there are regions of depleted EUV emission that evolve rapidly, expanding and refilling in a matter of hours. These transient coronal holes, or coronal dimmings, are most likely associated with a depletion of coronal material following a coronal mass ejection (CME) which is magnetically anchored in these regions (Rust, 1983; Thompson et al., 2000; Yang et al., 2008; Aschwanden et al., 2009).

Models have been developed to study the large scale magnetic fields on the Sun and to calculate the open magnetic flux budget in the heliosphere. These models include extrapolation models, such as the widely used Potential Field Source Surface (PFSS) model (Schatten et al., 1969; Wang & Sheeley, 1992), as well as more sophisticated MHD models (See review by Mackay & Yeates, 2012). All models use observed photospheric magnetograms or some variation of them (Schrijver & De Rosa, 2003) as the boundary condition. These models compute open magnetic field lines that extend to the heliosphere, and calculate the total open flux to compare with in-situ measurements of Interplanetary Magnetic Field (IMF) by satellites such as Ulysses (Balogh et al., 1992; Mackay & Yeates, 2012).

To validate models, the foot-prints of model computed open field lines on the Sun's surface are sometimes compared with observed coronal holes. It was shown that the global pattern of the open-field foot-points computed by either MHD or PFSS models during one solar rotation in general matches the long-lived coronal hole boundaries observed in the chromosphere He I 10830 line or EUV/X-rays (Levine, 1982; Wang et al., 1996; Neugebauer et al., 1998), in particular in polar caps. However, to our knowledge, systematic measurement of magnetic flux directly from observed coronal holes has been done rarely; Harvey & Recely (2002) provides one of the very few direct measurements of open flux from polar holes detected in the He I 10830 line covering a decade from 1990 to 2000. Furthermore, more than thirty years ago, Harvey & Sheeley (1979) raised the question of the relative contribution of magnetic open flux by coronal holes of all kinds, including strong polar holes, weak low-latitude holes, and possibly miniature coronal holes in young active regions. Recently, it was shown that low-latitude long-lived holes contribute significantly to the open flux during the solar maximum (Neugebauer et al., 2002; Luhmann et al., 2002; Schrijver & De Rosa, 2003), and it was also proposed that contribution by some short-lived coronal holes associated with CMEs may not be negligible (Riley, 2007). Note that these studies applied PFSS or MHD models, as well as inference from the in-situ IMF measurements, to reach these conclusions. It is important to test these suggestions from observations of coronal holes and direct measurements of magnetic flux in the holes at different latitudes.

The *Extreme-ultraviolet Imaging Telescope* (EIT; Delaboudinière et al., 1995) onboard the *Solar and Heliospheric Observatory* (SoHO) has been observing the corona since 1995, and therefore provides a stable database suitable for systematic tracking and characterization of EUV coronal holes for the past one and and one-half solar cycle. In 2010, the *Solar Dynamics Observatory* (SDO) was launched; meanwhile (at the time of original publication), the *Solar Terrestrial Relations Observatory* (STEREO) A and B have reached vantage points that are separated from SDO by nearly ±90 degrees. As of July 2015, STEREO-A has re-established contact after transiting behind the sun. STEREO-B lost contact before this transit, which has not been re-established. Therefore, the EUV telescope *Atmospheric Imaging Assembly* (AIA; Lemen et al., 2012) onboard SDO in conjunction with the *Extreme Ultraviolet Imager* (EUVI; Howard et al., 2008) onboard STEREO A and B have been able to provide nearly full coverage of the solar atmosphere observed in EUV wavelengths. These data can be employed to obtain continuous, consistent, full solar surface observations of coronal hole boundaries for the present solar cycle 24.

In this chapter, we utilize these available databases to track and characterize EUV coronal holes, and make a comparison of magnetic flux directly measured from these holes with open flux computed by the widely used PFSS model. The analysis and model are performed for the past solar cycle (1996 - 2011) observed by EIT, as well as the two years when the Sun has been observed by EIT, AIA, and EUVI. Because a large amount of data over a long period are analyzed, we limit the scope of the present study to a cadence of 12 hours for AIA/EUVI observations and 24 hours for EIT observations; therefore, the focus is on relatively long-lived coronal holes, but not transient holes. In the following text, we will describe the data and analysis method in Section 2. Section 3 will present the results of coronal hole tracking and measurements of magnetic flux from the holes in comparison with the PFSS model. Discussions and conclusions are given in Section 4.

Methodology

To analyze coronal holes, we employ the EUV full-disk images obtained by EIT from 1996 May to the end of 2010 and by AIA and EUVI since 2010 May. Photospheric magnetic field measurements are obtained by Michelson Doppler Imager (Scherrer et al., 1995) onboard SoHO from 1996 to 2010, and then by Helioseismic and Magnetic Imager (Scherrer et al., 2012) since 2010 April. We develop an automated procedure to detect coronal holes using these data, and study some properties of coronal holes, including their persistency, latitude distribution, and magnetic flux. These properties are then compared with the PFSS model results.

Table 2.1. Data coverage for each instrument source

		Start		End	
Source	Observable	CR	Date	CR	Date
SOHO/EIT	EUV 195Å	1909.96	1996 05 31	2105.27	2010 12 31
SDO/AIA	EUV 193Å	2096.76	2010 05 13	2133.17	2013 01 30
STEREO/EUVI	EUV 195Å	2096.76	2010 05 13	2133.17	2013 01 30
WSO Harmonics	B_r	1893.00	1995 02 23	2113.00	2011 07 29
Synoptic *SOHO*/MDI	B_r	1911.00	1996 06 28	2104.00	2010 11 26
Synoptic *SDO*/HMI	B_r	2096.00	2010 04 22	2134.00	2013 02 21

Observations

Table 2.1 displays the availability of each dataset in use. As mentioned previously, one of the benefits of using a combination of data sources from AIA and EUVI A/B is the ability to have near full surface observations. For the example observation provided, 2010 June 29, the two STEREO spacecraft have separated in their orbits to provide a nearly full surface view. Several months later, full coverage was achieved by the three spacecraft, and this complete coverage has continued for several years to come. Figure 2.1 displays the coverage overlap between the three instruments. Contours are marked at 0.95 $R_\odot$ for the field of view of each instrument. AIA, EUVI:A, and EUVI:B are centered at Carrington longitude 190, 265, and 120 degrees, respectively.

The brief overlap between the EIT and AIA-EUVI datasets will serve as a crucial comparison between the two sources. EUVI and EIT observations in 195 Å measure

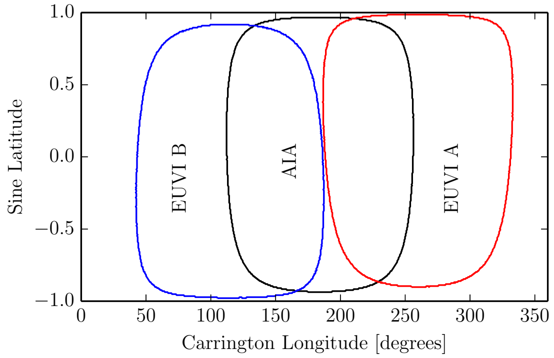

Figure 2.1. Available instrument coverage for 2010 June 29. Contours are marked for each instrument field of view, truncated at 0.95 $R_\odot$ for purposes of illustration. The fields of view for AIA, EUVI:A, and EUVI:B are centered at Carrington longitude values of 190, 265, and 120 degrees, respectively. Note the enhanced polar viewing angles achieved with the EUVI instruments.

emission primarily from Fe XII. AIA observations in 193 Å measure primarily emission from Fe XII, but with additional emission from Fe XXIV whose formation temperature is about 10 MK. Since coronal holes are characterized by low-temperature plasmas (Cranmer, 2009), the difference in the wavelengths between EIT and AIA-EUVI is unlikely to bias the coronal hole detection. On the other hand, detection of the boundaries of coronal holes, especially relatively smaller holes, may be affected by scattered light from adjacent bright features. EIT images may be subject to a higher level of scattered light (Shearer et al., 2012). The effect of the scattered light in different instruments will manifest itself when we make the comparison of hole detection, and will be discussed later.

Accompanying the EUV observations by the above-mentioned instruments, MDI and HMI provide the magnetic field measurements. Processed charts of radial magnetic field strength are employed from both MDI and HMI observations. MDI charts are corrected to account for missing polar field information due to inconvenient solar tilt angles throughout the year. The details of this correction are discussed in Sun et al. (2011). Considering the pass-off of data from MDI to HMI in our studies of open magnetic flux, validating observations between these two instruments is crucial. Effects such as instrument degradation and sensitivity are key. A more detailed study of the inter-calibration between the two measurements is available from the work of Liu et al. (2012).

Thresholding Routine

Building on the work of Krista & Gallagher (2009), we have developed an enhanced routine for automated coronal hole detection, capable of working with multiple input sources of data. The routine first identifies dark features in EUV images, and then utilizing synoptic maps of calculated radial magnetic field, this routine is able to distinguish between coronal holes (dominated by one magnetic polarity) and filament channels (mixed polarity).

Each EUV image is processed using the standard SolarSoftWare IDL (SSWIDL) software routines for each particular instrument (Freeland & Handy, 1998). The AIA images are read into memory and processed using `read_sdo.pro` and `aia_prep.pro`,

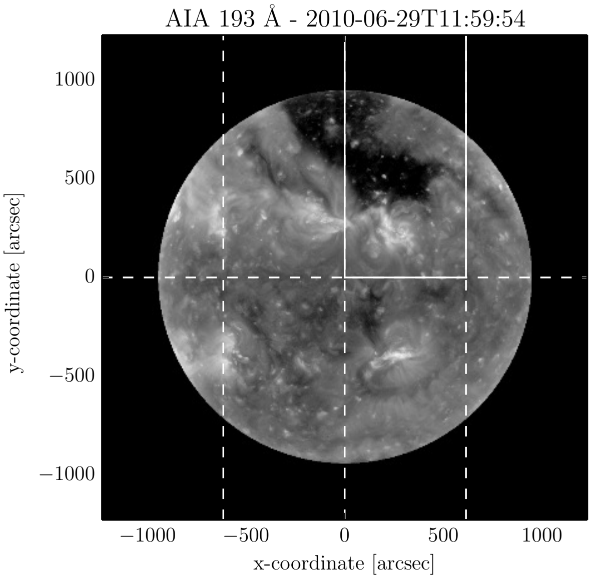

Figure 2.2. Full-disk EUV data taken at 193 Å by the AIA instrument aboard SDO. The thresholding routine proceeds to partition this data into eight sub-arrays, on each of which the code runs the thresholding calculation. Each sub-array contains a differing mixture of bright and dark features. The solid boxed sub-array marks the sub-array being considered in Figure 2.3.

respectively. The EUVI:A/B images are read and processed using the `secchi_prep.pro` routine. The EIT images are read and processed using the `eit_prep.pro` routine. A mask is applied to each respective image to remove off-limb information. Each of the processed and cropped EUV images is subdivided into eight sub-arrays for further analysis as described below. Figure 2.2 illustrates this sub-array arrangement.

Gallagher et al. (1998) have shown that a histogram of EUV intensity corresponds to the contribution from multiple sources. More importantly, by thresholding an image in the valley between contributing peaks in EUV intensity histograms, features can be separated. Following this experience, we use the EUV intensity histogram

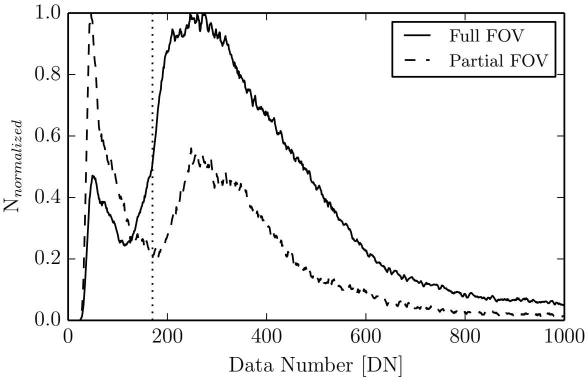

Figure 2.3. Histogram of the sub-array marked in Figure 2.2, calculated in terms of data number for the recorded image. This figure displays a limited range of the full extent of the data, and has been boxcar smoothed with a width of 10 DN for clarity of the underlying form of the data. The solid curve and dashed curve refer to the full field of view, and the marked subarray, respectively. The vertical line indicates the local minimum value that is appropriate as a thresholding value in DN. Note that this local minimum is not always readily detectable in the full field of view data.

to define the threshold for coronal holes. It was also suggested that this method works better by partitioning a full-disk EUV image into a few sub-frames (Krista & Gallagher, 2009). Partitioning reduces the overlap between features in an intensity histogram, as there are simply fewer contributing sources, particularly the quiet sun emission, in the narrow field of view. Consider a histogram of EUV intensity, measured in DN, as displayed in Figure 2.3. The EUV intensity histograms of the full field of view and the sub-array are displayed in the solid curve and dashed curve, respectively. Each curve is normalized for comparison.

The histogram of the partial frame exhibits sharper peaks than in the full histogram. The two peaks seen in the partial field of view at 50 DN and 250 DN correspond to coronal holes and quiet sun, respectively. The local minimum between the quiet sun peak and coronal hole peak defines the threshold between these two features. By plotting the contour at this threshold on the original EUV image, we find this threshold rather reliably outlines the coronal hole boundary. In contrast, the full field of view histogram displays a very broad and slightly shifted peak, pushing against the lower-intensity coronal hole peak, indicative of an over-dominant contribution by the quiet sun emission. By partitioning the image into sub-arrays, particularly in those sub-frames where coronal holes are present, the quiet-sun contribution is minimized. In addition, the shape of each sub-array is vertical in nature to better capture contribution from both polar coronal holes and quiet regions.

An EUV intensity histogram is calculated for each sub-array, and numerical first and second derivatives are taken. The quiet sun DN value is defined from the median of the on-disk image. From our experiments, the coronal hole threshold is close to half of the quiet sun DN value. The routine searches for a local minimum closest to half of the quiet sun DN value in each sub-array to define the threshold value. If a local minimum does not exist within 0.3-0.7 DN_{QS}, the sub-array is discarded. After each threshold value is computed a full field of view thresholding value is computed from the mean of the valid sub-array threshold values. This final threshold is then applied to the full FOV image to find coronal hole boundaries.

This code was then tested with and used to gather results from several instruments, AIA, EUVI-A and B, and EIT. Despite using multiple instruments with differing calibrations, this modified routine has proven consistent with maintaining relatively stable coronal hole thresholding values as well as coronal hole boundaries over a long time period. Consider Figure 2.4, which displays the thresholding value for EIT, AIA, EUVI-A, and EUVI-B. The values are displayed as a ratio to the quiet sun value, to avoid dimensionality. Quiet sun values were determined through the median data number within each frame. This ratio value stays relatively stable throughout the dataset shown.

It is seen that the threshold relative to the quiet sun intensity is markedly different for different instruments. The mean threshold to quiet sun ratio is 0.53, 0.33, 0.32, and 1.18, for AIA, EUVI A, EUVI B, and EIT, respectively. The difference must be partly due to the different instrument calibration, sensitivity, and scattered light level. It is noted that the threshold for EIT is rather large, perhaps due to higher scattered light levels; for EIT, this value also drifts up after 2003, maybe due to detector degradation. There are high frequency fluctuations in this ratio for each of the instruments, which may reflect frame-to-frame changes. For this study focusing on relatively long-lived coronal holes that persist for many days, we consider the short-term fluctuations unimportant. These fluctuations introduce subsequent fluctuations

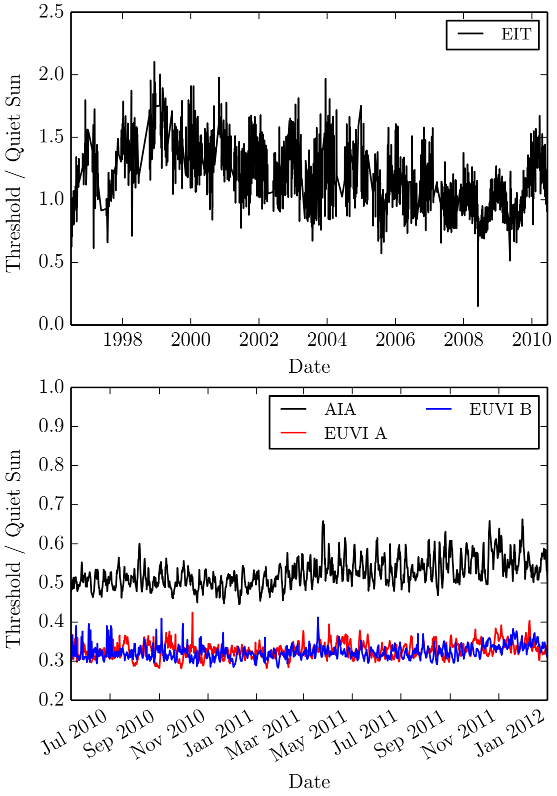

Figure 2.4. Ratio of the data number thresholding value to the quiet sun value for each instrument set. EIT data is displayed in the upper panel, and AIA, EUVI A/B in the lower panel.

in the calculation of coronal hole area and magnetic fluxes, which will be addressed later in the chapter.

Figure 2.5 shows the coronal hole boundaries detected in the EUV images obtained by different instruments, using this automated thresholding technique. The left panel displays a synoptic EUV image gathered from EIT 195 Å, with contours displaying the calculated coronal hole boundaries from EIT data (white) and AIA data alone (red). The right panel displays a synoptic EUV image gathered from AIA 193 Å, with contours of coronal hole boundaries from AIA data alone (red) and EUVI A/B data alone (white). The comparison of the two images as well as the two contours show evidently that the superior contrast of AIA and EUVI images allow better detection of coronal holes. The polar hole is captured in both images, but the AIA/EUVI polar hole is larger than the EIT hole. Smaller or weaker holes at lower latitudes are evidently present and detected in the AIA/EUVI image, but hardly seen in the EIT image. Therefore, AIA and EUVI measurements are crucial to study coronal holes in middle-low latitudes. As these holes may be located in stronger magnetic fields compared with polar holes, they may contribute significantly to the magnetic open flux. This will be further discussed in Section 4 when open flux measurements are compared.

Coronal Hole Determination

The thresholding technique is able to identify dark features in the EUV images, including both coronal holes and filaments or filament channels. To automatically distinguish coronal holes from filaments, we also incorporate magnetic field information from synoptic charts of radial magnetic flux. Coronal hole regions are most often clearly dominated by a single magnetic polarity over their entire area (Wang, 2009). Filament channels are characterized by depleted intensity in EUV wavelengths, similar to coronal holes. However, filament channels lie along a polarity inversion line, and

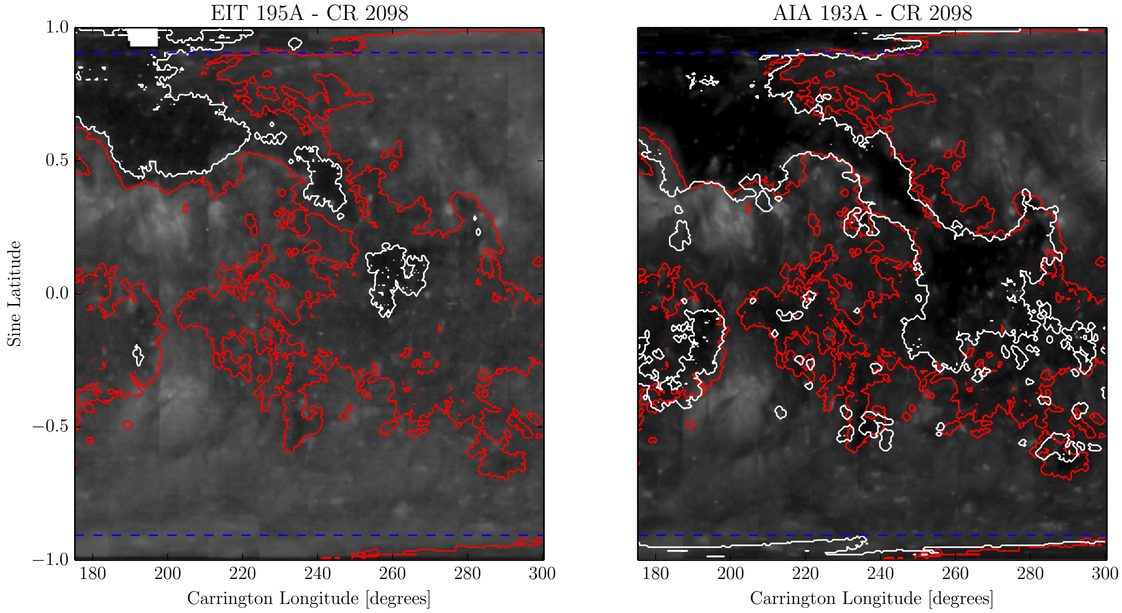

Figure 2.5. Left: EUV synoptic image from EIT 195 Å, with contours of calculated coronal hole boundaries from EIT data in white and AIA data in red. Right: EUV synoptic image from AIA 193 Å, with contours of calculated coronal hole boundaries from AIA data in red, and EUVI A/B data in white. The enhanced contrast of the AIA instrument is immediately apparent for the calculation of coronal hole boundaries.

thus lie atop a region which will tend to be magnetically neutral as a whole. Therefore, in addition to the criteria of EUV intensity, a coronal hole candidate region must also tend towards a dominating polarity. With the thresholding on each instrument completed for a particular time frame, each array is converted into a boolean array, with 0 indicating regions above the threshold value for that instrument at that particular time. A value of 1 in a pixel marks areas below the threshold value. These individual arrays are then projected into a Carrington equal area map, marked in longitude and sine latitude. Each of the suspect regions are overlaid with a synoptic map of radial magnetic field, as displayed in Figure 2.6. For each region in question composed of N pixels, there exist N values of magnetic flux, defined as Φ. We can define the skew of the magnetic flux as, denoting it as the variable γ,

$$\gamma = \frac{1}{N} \sum_{j=0}^{N-1} \left(\frac{\Phi_j - \bar{\Phi}}{\sigma} \right)^3 . \tag{2.1}$$

Here $\bar{\Phi}$ denotes the mean flux value within a particular region and σ denotes the standard deviation of the flux values within the region. The value of magnetic flux skew is calculated for each suspected coronal hole region in this way. Regions whose magnetic flux skew exceed 0.5 in magnitude are labeled as coronal holes. This value was chosen through a manual search of select regions, finding this value to accurately distinguish between the two phenomena.

Magnetic flux histograms are compared for the labeled coronal hole and filament channel in Figure 2.7. The histogram of magnetic flux in the filament channel shows a relative balance between positive and negative magnetic flux. The histogram for the magnetic flux in the coronal hole, however, is noticeably skewed towards negative magnetic flux values.

Figure 2.8 displays a histogram of the magnetic flux skew values for each of the suspected coronal hole regions. Vertical dashed lines display the cutoff value of ± 0.5. For EIT measurements, the MDI synoptic charts of radial magnetic field flux are used; and for AIA-EUVI measurements, the HMI synoptic charts of radial magnetic field flux are used.

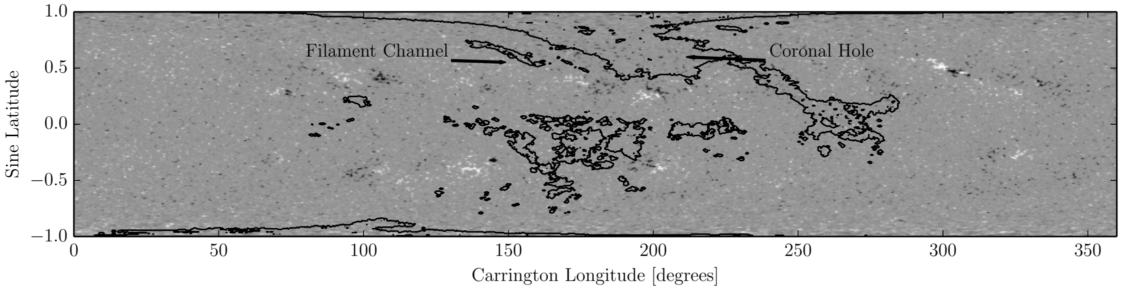

Figure 2.6. HMI synoptic map of radial magnetic field for Carrington rotation 2098, with contours of initially suspected coronal hole regions. Each source of data, AIA and EUVI A/B, were run through the thresholding routine, producing a DN threshold value for each source. Contours were produced of regions below this thresholding value, and projected into a Carrington equal area projection.

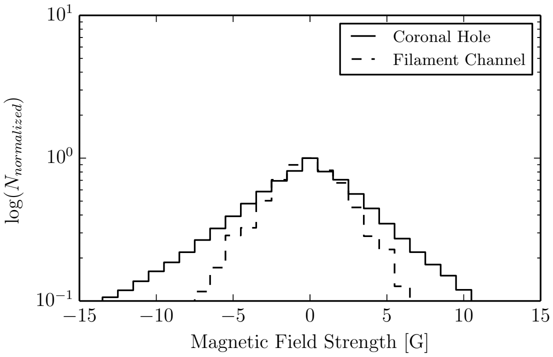

Figure 2.7. Example of the magnetic flux distribution within two suspected coronal hole regions. The solid line displays a histogram of magnetic flux for a positively identified coronal hole region. The magnetic flux within the coronal hole boundary is slightly unbalanced, tending toward negative polarity. The dashed curve is data from an identified filament channel, which is more balanced in flux distribution. Note that the distributions vary outside of the HMI noise level, ± 2.3 G.

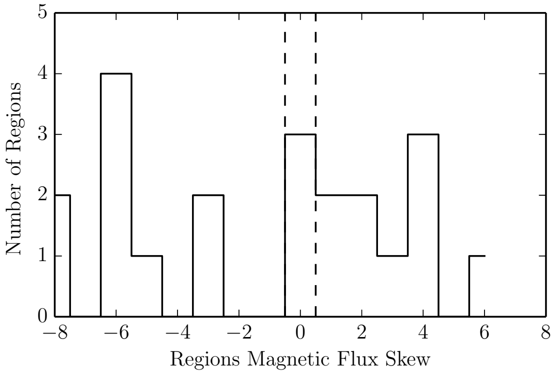

Figure 2.8. Histogram of the calculated magnetic flux skew values for the particular time frame under consideration. Vertical dashed lines indicate the magnetic flux skew cutoff value, 0.5. Regions whose calculated magnetic flux skew are less than 0.5 in magnitude are identified as filament channels.

Persistence, Area, and Open Flux of Coronal Holes

EUV images are analyzed with the above-mentioned technique to determine coronal hole boundaries. For a given dataset, each individual image frame is characterized by a discretized set of spatial and temporal coordinates, a set of latitudes, longitudes, and time frames, $\{\theta, \phi, t\}$. This set is discretized such that each is indexed by an integer value, $\{\theta_i, \phi_j, t_k\}$. For each of these values, a byte value is assigned that indicates the presence of a coronal hole, defined as a scalar function, $\psi(\theta_i, \phi_j, t_k)$. For a particular range of time, a 'persistence map' can be defined as the overall persistence of a coronal hole within a particular location. This map can be defined as

$$\Psi(\theta_i, \phi_j) = \sum_k \psi(\theta_i, \phi_j, t_k). \tag{2.2}$$

Note that this persistency is not continuous in nature, but totaled over the entire period under consideration. Nevertheless, the persistence map illustrates the overall distribution pattern and persistence of coronal holes, which, as a global property, can be compared for different instruments or models.

In considering the persistency array data, it is crucial to note that though the view from each instrument overlaps, the persistency data do not over-count pixels. After stitching the view from each instrument together, the coronal hole map array is flattened into a binary map, only noting the existence of a coronal hole without regard to the number of instruments that may have observed it. Coronal hole surface area is calculated by summing for each particular frame in the persistence array for the instrument set under consideration,

$$A_{CH}(t_k) = R_\odot^2 \sum_{i,j} \psi(\theta_i, \phi_j, t_k) \cos(\theta_i). \tag{2.3}$$

In addition to the spatial hole data, magnetic flux measurements are available. Using the persistence information previously mentioned, the magnetic flux can be defined via

$$\Phi_M(t_k) = R_\odot^2 \sum_{i,j} \psi(\theta_i, \phi_j, t_k) \cos(\theta_i) B_r(\theta_i, \phi_j, t_k). \tag{2.4}$$

Here, these flux measurements are obtained using calibrated synoptic charts of radial magnetic field strength. For coronal holes observed with EIT data from 1996 through the end of 2010, the MDI synoptic charts are employed. We sum the radial magnetic field in the coronal holes with a cutoff magnetic field strength at ± 5.0 G, which was determined to be the noise level of the MDI synoptic charts (Liu et al., 2012). For coronal holes measured with AIA-EUVI data from 2010 June to 2013 January, the HMI synoptic charts are used with a cutoff field strength at ± 2.3 G, the noise level for the HMI synoptic charts calculated by Liu et al. (2012).

Table 2.2 displays the standard deviation values for A_{CH} (surface area) and Φ_M (magnetic flux), and in each latitude region under consideration for each instrument / calculation set. Full, northern pole (NP), low-latitudes (LL), and southern pole (SP) regions are defined from latitudes of -90:90, 65:90, -65:65, and -90:-65 degrees, respectively. These values are calculated from the time series of each quantity, and represent the uncertainty in their calculation stemming from the variation in calculated thresholding value.

Whereas full surface map may help capture more coronal holes, one limitation is the partial magnetic field availability. The line of sight magnetic field measurements are only taken onboard the SDO spacecraft, and are therefore only for one vantage angle. The effects of possible changing magnetic fields on the back-side will be examined in the ensuing study. In this present study, we assume that for the course of one rotation the relevant magnetic field does not drastically change in the coronal hole interior regions, therefore a synoptic chart approach may be taken.

Table 2.2. Uncertainty in coronal hole / open field quantities

Dataset	Region	$\sigma_{A_{CH}}$ $[10^{20} cm^2]$	σ_{Φ_M} $[10^{21} Mx]$
EIT	Full	13.7	12.4
	NP	8.51	5.59
	LL	8.62	9.30
	SP	7.28	5.71
PFSS	Full	13.8	7.10
	NP	3.80	2.81
	LL	13.8	7.51
	SP	3.03	2.28
AIA/EUVI	Full	9.02	5.38
	NP	0.432	0.319
	LL	7.79	3.95
	SP	2.47	2.31

In the following section, we will compare the area and open flux of coronal holes and their latitude dependence using EIT and AIA-EUVI observations, as well as from the PFSS model.

Properties of Persistent Coronal Holes

EIT Observations

We have analyzed the entire EIT dataset in 195 Å. This dataset spans Carrington rotations 1920-2105, corresponding to the time period from 1996 May 31 to 2010 December 31, as referenced in Table 2.1. This dataset provides a unique opportunity to study coronal holes consistently throughout the activity variation along a solar cycle. The EIT data are analyzed at the cadence of one image per day; coronal holes detected with this cadence are rather long-lived features, or persistent coronal holes. Our analysis shows that, as one would expect, the majority of coronal hole persistence occurs near the polar regions above 60 degrees in latitude. Through the solar cycle from the solar minimum (1996 - 1997) to solar maximum (2000 - 2003), coronal holes gradually extend downward from the polar cap to lower latitudes. These variations can be better characterized by the evolution of the coronal hole area and open flux at varying latitudes.

Figure 2.9 displays the coronal hole area, as well as the total unsigned magnetic flux determined from these coronal hole boundaries by summing the radial magnetic field measured from the synoptic charts of MDI. To further distinguish contributions to the open flux from different latitudes, we also plot the areas and fluxes from the north polar holes (defined for latitudes from 65 to 90 degrees), the middle-low latitude region (defined from -65 to 65 degrees), and south polar holes (from -90 to -65 degrees), respectively. These are compared with the open flux and area computed using the PFSS model, as will be described later in the text.

The top panel of the figure shows the total area and total open magnetic flux, which are roughly correlated during the solar cycle. The total surface area measured from EIT (red dashed line) reaches more than 15% of the total solar surface area during the minimum between 1996 and 1997, and then rapidly decreases until 1999; after the solar maximum, the coronal hole area increases again to about 10% in 2003,

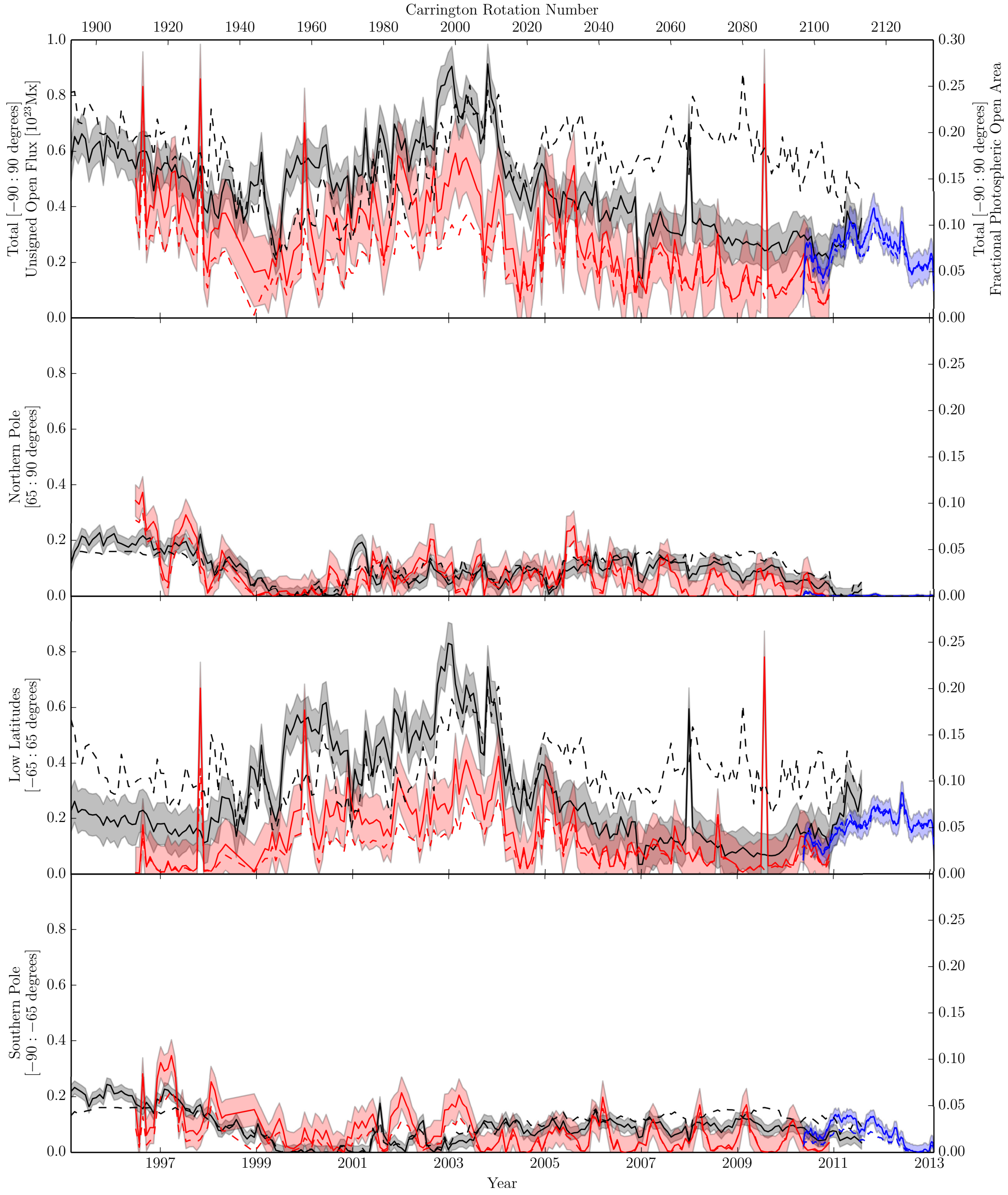

Figure 2.9. Unsigned open magnetic flux and fractional photospheric open area for calculated PFSS field, and observed coronal hole boundaries from EIT and AIA/EUVI. Unsigned open magnetic flux and open area are displayed with solid and dashed curves, respectively. PFSS, EIT, and AIA/EUVI results are color coded as black, red, and blue, respectively, with corresponding shaded regions displaying the standard deviation of the flux values.

and then gradually decreases to nearly 5% during the last extended minimum between 2006 - 2010. Correspondingly, the total open flux rapidly decreases from 5×10^{22} Mx (if we ignore the few spikes) in mid-1996, to the minimum of 2×10^{22} Mx in 1999, and then increases to be around 5×10^{22} Mx in 2003; the total open flux stays low at around 2×10^{22} Mx after 2006. The total open flux measured from EIT coronal holes vary by a factor of 2-3 from minimum to maximum.

The lower three panels show the latitude-dependence of the open flux. It is evident that contributions from the polar holes and middle-low latitudes vary in different ways during the solar cycle. Significant polar holes in both the north and south are captured in EIT observations during the minimum from 1996 - 1998, which then shrink until 1999, and then grow again afterwards. During the last minimum, the total polar hole area is relatively low covering less than 5% of the total solar surface. The open flux from the polar holes is strictly correlated with the hole area, reflecting the relatively smooth magnetic field distribution in polar holes. The middle-low latitude holes have the largest area coverage shortly after the solar maximum; from 2000 to 2004, these holes cover an area between 5-10% of total solar surface, and contribute to the total open flux more significantly because of the stronger magnetic field in these regions. During the solar minima, the total hole area is rather low at 1-2% on average. Note that there are larger holes in the middle-low latitudes during the past solar minimum between 2006 - 2008 than the previous one between 1996 - 1998.

Measurements of polar hole area and open flux were also conducted by Harvey & Recely (2002) using observations at the chromospheric He I 10830 line from National Solar Observatory / Kitt Peak (NSO/KP). These measurements cover the period from 1990 - 2000, partly overlapping with the EIT measurements in the present study. Comparing these two measurements during 1996 - 2000, it is seen that the annual variations in the two measurements are quite consistent for both the north polar holes and south polar holes. Both measurements show that the north polar holes cover up to 8% surface area and south polar holes cover up to 7% surface area between 1996 and 1997, followed by a decrease in area. Both measurements show, in both polar holes, a local minimum around 1997, a peak in middle 1997, another minimum around 1998, and then a peak afterwards. From 1998 to 2000, the north polar hole diminishes faster than the south polar hole, as shown in both observations. In terms of the open flux, Harvey & Recely (2002) used NSO/KP magnetograms, with MDI magnetograms used in the present study. Both measurements yield the maximum open flux of $3{\times}10^{22}$ Mx in either north or south polar holes between 1996 and 1998, which decreases in the same fashion as the area decreases. Therefore, the comparison between these two independent studies during this overlapping time period shows very good consistency in measuring polar holes using two different kinds of observations.

AIA-EUVI Observations

The EIT instrument onboard SoHO is limited to the view from the Earth-Sun line; furthermore, we have shown that EIT observations underestimate the area of low-latitude coronal holes, which we attribute to a higher level of instrument scattered light. AIA and EUVI provide a comparable dataset to that used on EIT, with higher sensitivity to coronal holes outside the polar caps, and with the added bonus of multiple viewpoints. AIA-EUVI data are obtained from Carrington rotations 2096-2133. This spans the time period from 2010 May to 2013 January, as referenced in Table 2.1. We analyze these data sampled at 12 hour cadence to capture persistent coronal holes.

From these data, we measure the coronal hole area and open flux, displayed by dashed and solid blue lines, respectively, in Figure 2.9. The top panel shows the total surface area and total unsigned flux. Coronal holes cover the total solar surface by 5-10% from 2010 - 2013, and the total flux in these holes is measured to range from 2×10^{22} Mx in late 2010 and late 2012 to 4×10^{22} Mx around 2012. The total flux is entirely correlated with the hole area, and varies by a factor of 2.

The latitude dependence of the open flux is examined in the following panels, showing that the north polar holes are present only for a short period during mid-2010, having diminished since then. The south polar holes persist for two more years and diminish in late 2012. These holes contribute to up to 1.7×10^{22} Mx open magnetic flux. Coronal holes in the middle-low latitudes contribute significantly, and account for twice as much open flux as from the south polar holes. After mid-2012, middle-low latitude holes dominate.

It is noted that, during the period of the second half of 2010 when both EIT and AIA-EUVI observations are analyzed, the hole area measured from AIA-EUVI observations is significantly greater than that measured in EIT observations. The figure suggests that, in both the south polar regions and middle-low latitude regions, AIA-EUVI sees larger holes than EIT, while in the north polar region, EIT holes cover a larger area than AIA-EUVI during the brief period of mid-2010. These differences lead to an overall greater open flux measured with AIA-EUVI observations during the overlapping period. We note that the open flux in EIT holes is measured using synoptic MDI magnetograms, and the open flux in the AIA-EUVI holes is measured using synoptic HMI magnetograms. Nevertheless, using different magnetograms does not change the total flux measured in the holes; the difference in the flux measurements is solely produced by the difference in the hole area measurements. These discrepancies will be further discussed in the next section, and also with respect to their comparison with model results.

PFSS Model Comparison

The widely used potential field source surface (PFSS) model, following the work of Wang & Sheeley (1992), is employed for this study to reconstruct the global coronal magnetic field. The PFSS model is an extrapolation method that assumes a potential field below a nominal source surface set at 2.5 solar radii (Schatten et al., 1969; Hoeksema, 1984), with field lines above 2.5 solar radii being open. The model uses monthly synoptic charts composed from photospheric magnetograms as the boundary condition to compute the potential field. This implies an underlying assumption that the large-scale magnetic field is static over one rotation. These assumptions ignore evolution of the photospheric magnetic field and the possibility that the solar corona is not entirely current free. To circumvent some of these problems, Schrijver & De Rosa (2003) used a few techniques to improve the boundary condition; they used a flux dispersal model to evolve the photospheric magnetic field, applied a data assimilation technique to update the synoptic chart by inserting newly emerging active regions on the disk, and inferred active region locations on the back side of the Sun with helioseismology approaches. Variations of the PFSS reconstruction methods and numerous MHD models have also been developed with their results compared against one another. These models are reviewed by Mackay & Yeates (2012). In this study, we focus on a first-order comparison of global patterns of persistent coronal holes, so the standard PFSS reconstruction is adopted despite various issues related to this model. In addition, the PFSS model has been widely used to calculate open magnetic flux, which is then compared with various other measurements or calculations by other models. Therefore, PFSS results can provide a baseline reference to compare our measurements to various other studies.

We compute the spherical harmonic coefficients from the longitudinal magnetograms obtained by Wilcox Solar Observatory to 29 orders, and use them to reconstruct the magnetic field at the solar surface as the boundary condition. For potential magnetic field, a magnetic scalar potential is defined which satisfies $\nabla^2\Phi_M = 0$. And the potential magnetic field below the source surface $2.5R_\odot$ is then calculated as $\mathbf{B} = -\nabla\Phi_M$.

A field-line tracking routine is then used to map the foot-prints of open field lines to the solar surface, namely the model computed coronal holes. Open field area and magnetic flux values are calculated at the photosphere in a manner similar to EIT and AIA/EUVI coronal hole observations, using the open field regions as a mask in this situation. The model computed coronal hole area and open flux are then compared with observations, as presented in Figure 2.9. In the figure, the model computed coronal hole area and open flux are plotted in dashed and solid black lines, respectively.

First, comparing EIT observations with the PFSS results, it is seen that the solar cycle variation of the total open flux is present in both measurements, but the total hole area and open flux from EIT measurements are consistently smaller than derived from the PFSS model throughout the solar cycle. The EIT flux is closest to the PFSS flux during the initial minimum period of solar cycle 23, until 1998, with $\Phi_{EIT} \approx 0.8\Phi_{PFSS}$. During the solar maximum, the EIT measured flux is only about 60-70% of the PFSS flux. The EIT flux temporarily matches the PFSS flux between 2005 and 2006, and then drops to about 50% of the PFSS flux since then. It also appears that, from 2005 to 2011, the total hole area measured using the PFSS model is significantly higher than measured in EIT data, when the correlation between hole area and total flux is not preserved in the PFSS measurements during this period.

A more detailed comparison of latitude-dependence shows that the model and observation are relatively consistent in measurements of polar holes. There is very good agreement between modeled and observed hole area as well as open flux in both the north and south polar caps during the previous solar minimum (1997 - 2001); during the maximum (2001 - 2005), the PFSS model and observation agree with each other for north polar holes, but do not compare very well in south polar holes. From 2005 - 2011, which covers an extended solar minimum, the model and observational measurements in both polar holes show the same temporal variations in the open flux, which roughly exhibit a one-year period caused by the solar B_0-angle variations, yet fluctuations in the EIT observation have greater amplitudes. During this period, the PFSS computed open surface area is significantly larger even in polar holes.

There is marked disagreement in middle-low latitude holes between model and EIT observations. During the solar maximum, the model computed hole area and open flux are systematically larger than EIT measurements by nearly a factor of two. During the minima, the PFSS model appears to produce significantly more coronal hole area than observed by EIT, even though the calculated open flux is not as much due to weak magnetic field during the solar minima. In comparison, the PFSS model uses a very coarse resolution, which may artificially amplify open field regions. Other studies have indicated that PFSS tends to over-estimate the steady-state open flux (Lepri et al., 2008).

Some insight can be gained by also comparing with the AIA-EUVI measurements plotted in blue lines in Figure 2.9. For one and one-half years from 2010 June to 2012 January, the AIA-EUVI measured total open flux appears to match the PFSS open flux in both the evolution trend and absolute amount. Looking into details, in the middle-low latitudes, although the AIA-EUVI open flux more closely matches with the model flux than EIT does, it is still smaller than the model flux, and the PFSS hole area is still much larger than observed.

As a short summary, these plots show that the PFSS model tends to produce larger hole areas during most of the solar cycle, as compared with EIT and/or AIA-EUVI observations. The model also produces more open flux primarily in middle-low latitudes than exhibited in both observations. To understand these discrepancies, Figure 2.10 shows, as an example, the comparison of coronal hole boundaries in three different measurements during CR 2098 in 2010 June.

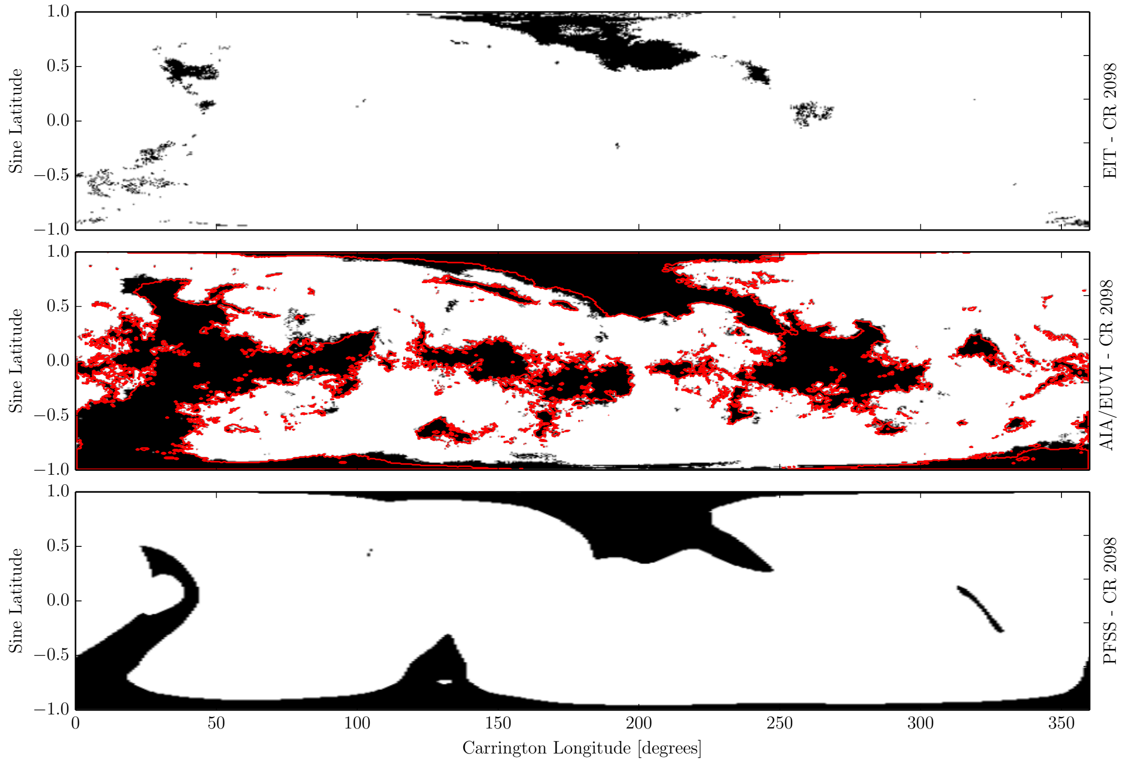

Figure 2.10. Coronal hole and open magnetic field boundaries for Carrington rotation 2098. The upper panel displays the observed coronal hole boundaries from EIT. The middle panel displays the observed coronal hole boundaries from AIA/EUVI in black, with a contour of AIA observations alone in red. The lower panel displays the open magnetic field boundaries from our PFSS calculation.

Seen in this comparison, all three measurements yield comparable hole boundaries in polar regions defined at greater than 65 degrees, excusing poor south polar coverage from EIT. It is evident that large discrepancies are present at middle-low latitudes. Compared with AIA-EUVI, EIT clearly cannot detect coronal holes to the same degree in this region, which explains the overall flux deficiency measured in EIT holes, particularly during the solar maximum, when low-latitude holes contribute more significantly. The comparison between PFSS holes and AIA-EUVI holes also shows that PFSS tends to over-estimate the areas of holes in the middle latitude region, which appear to extend from polar holes - these were called polar hole lobes by Harvey & Recely (2002). This is most evident at 130 degrees longitude in the southern pole and 210 degrees longitude in the northern pole. On the other hand, a series of smaller coronal holes at low-latitudes detected in AIA-EUVI images are missed by PFSS for this rotation. These discrepancies in middle and low latitude regions between PFSS and AIA-EUVI explain why the two measurements seem to yield a comparable amount of total open flux yet PFSS measures much larger hole areas than AIA-EUVI.

For a more complete comparison beyond one rotation, Figure 2.11 displays the observed and computed persistence maps for Carrington rotations 2096-2131, from 2010 May to 2013 January. The reconstructed open field map matches with observations only in very general global patterns. Both the reconstruction and observations show that coronal holes in the southern pole are the most persistent feature throughout this period. Discrepancies are present concerning the relative hole coverage at different latitudes. These persistency maps will aide studies that track the spatial and temporal evolution of coronal holes (Timothy et al., 1975; Miralles et al., 2001; McComas et al., 2002). However, the detailed study of evolution of coronal holes is

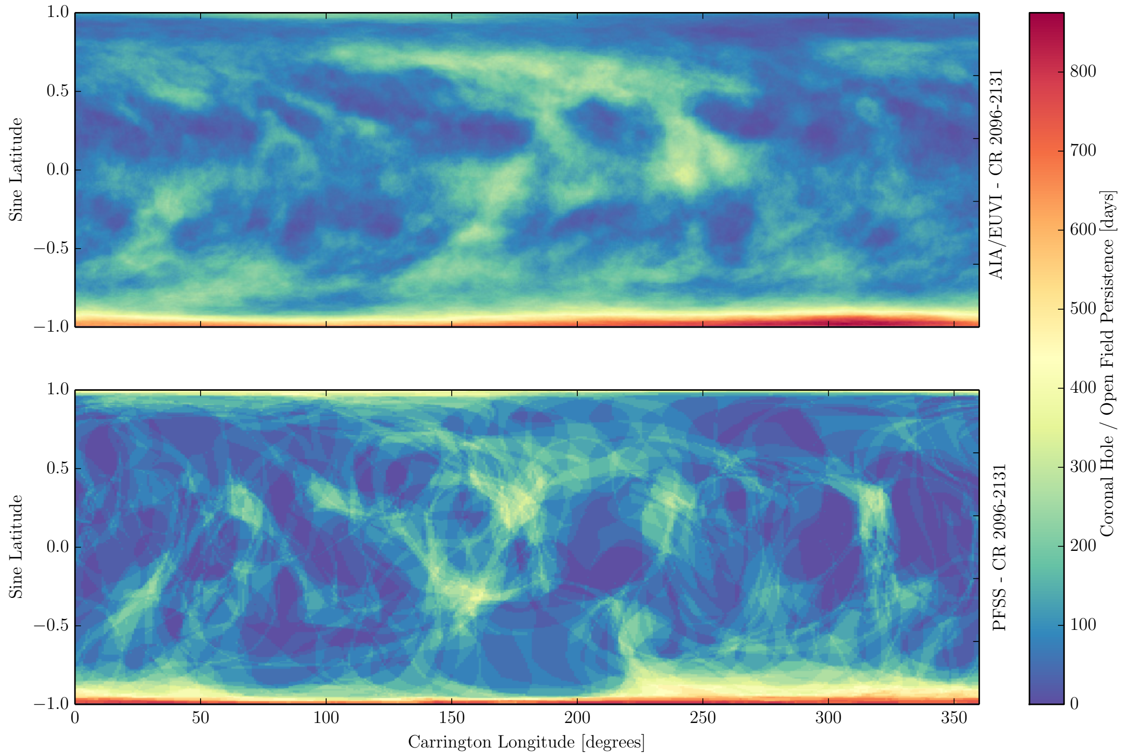

Figure 2.11. Coronal hole persistence map for a combination of AIA 193 Å and EUVI 195 Å datasets, along with a corresponding map generated using spherical harmonic coefficients obtained from the Wilcox Solar Observatory and a PFSS open field reconstruction. Persistence is scaled in days of non-consecutive persistence of coronal hole / open field for each pixel.

beyond the scope of the present work within this chapter, and will be conducted in the near future.

To further quantify the comparison, the persistence map is compressed along longitudes to yield a profile for coronal hole persistency as a function of latitude,

$$\lambda(\theta_i) = \sum_j \Psi(\theta_i, \phi_j). \tag{2.5}$$

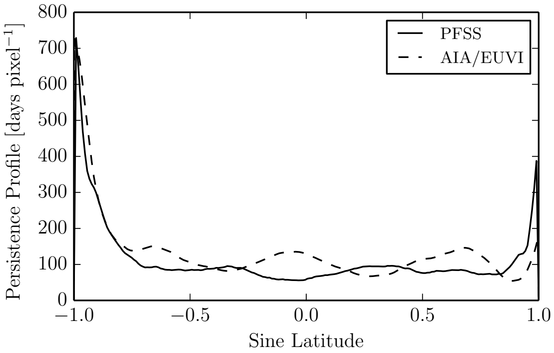

Figure 2.12. Coronal hole persistence map projected as a function of latitude. The two profiles are in units of *days pixel*$^{-1}$. The PFSS model calculates a further extension of open field persistence from the poles as compared with our AIA/EUVI observations. The persistence value at low latitudes agrees in value, but with variations in distribution visible in Figure 2.11.

Figure 2.12 illustrates this projection, reflecting the latitude dependence of the coronal hole coverage obtained by the two methods. Again, the plot shows similar global patterns with discrepancy in the relative hole distribution along the lower-latitudes. For the analyzed period, the PFSS reconstruction appears to have slightly over-estimated the northern polar hole area and the extension to middle latitudes. Caution should be taken, though, that the persistency in units of days in these maps is not directly proportional to the measured open flux, since the hole open fluxes are measured once per rotation for the potential field model.

Reversal of Magnetic Open Flux

Apart from the total unsigned flux from coronal holes, the total signed magnetic flux is also measured in coronal holes at different latitudes, namely the polar holes and middle-low latitude holes, as defined previously. Figure 2.13 displays signed magnetic flux in coronal holes measured from 1996 to 2013, first by EIT, and then by AIA-EUVI as well. Note that no correction has been made here for relative spacecraft B-angle, as is most apparent from the variation in polar data availability from the EIT dataset. Without making assumptions as to polar magnetic field data or coronal hole coverage, the overall trend is still visible.

Here, the temporal evolution of the flux reversal is evident. Whereas from 1996 until 2000 the northern pole is dominated by positive flux, and the southern pole dominated by negative flux, this trend reverses after 2000. Moreover, the overall magnitude of the signed flux indicates that the relative dominance of the respective polarities is much weaker after this reversal. Observations from AIA-EUVI maps have been displayed in dashed style. These values match well during the overlap with EIT.

During the period observed by AIA/EUVI, the southern pole is dominated by strong positive flux, the northern pole is weakly dominated by negative flux, and the low latitudes are more mixed, with a slight tendency towards negative fluxes. Here, the time evolution is more evident, as the low latitude regions are mostly negative for the first nine months of observation, where they transition to positive dominance. This then reverses back and forth a few times.

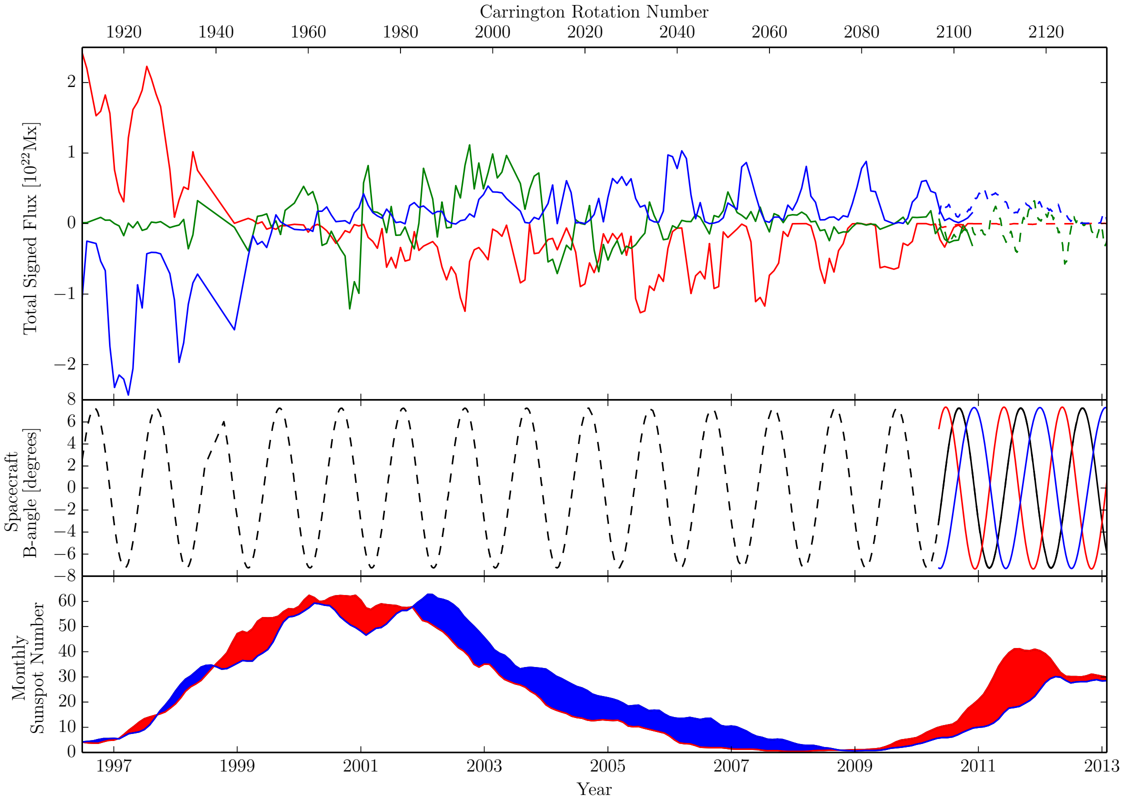

Figure 2.13. (top) Signed open magnetic flux from EIT/AIA-EUVI surface maps of coronal hole boundaries. Flux is subdivided into three segments depending on location. The southern polar, low-latitude, and northern polar regions extend between [-90,-65], [-65,65], [65,90] degrees latitude, and are displayed in blue, green, and red lines respectively. EIT-era observations are marked with a solid line, with AIA/EUVI observations marked with dashes. (middle) Spacecraft B-angle for the various instruments employed in the upper figure. SoHO, SDO, STEREO-A, and STEREO-B are displayed in dashed black, solid black, red, and blue, respectively. (bottom) Smoothed monthly sunspot number for the northern and southern hemisphere in red and blue, respectively. The area between curves is color-coded to indicate which hemisphere dominates. Sunspot data via WDC-SILSO, Royal Observatory of Belgium, Brussels.

Conclusions and Discussion

In this study, an automated method was devised and applied to detecting coronal hole boundaries using full-disk EUV imaging observations from a combination of instruments. SoHO:EIT, SDO:AIA, and STEREO:EUVI A/B data were considered over the respective instrument lifetimes. SoHO:EIT data was collected from 1996 through 2011, covering one and one-half solar cycles. The combined observations from SDO:AIA and STEREO:EUVI A/B provide nearly full-surface coverage, but over a shorter timespan from 2010 May to 2013 January. This combination of data provides a unique opportunity for continuous tracking of long-lived or persistent coronal holes. Aided with observations of photospheric magnetic field acquired by MDI and HMI, the magnetic flux is measured within defined coronal hole boundaries. Assuming that the magnetic flux within coronal hole boundaries largely represents magnetic open flux, we compare these results with a potential field source surface model.

The area, magnetic flux, and their latitude dependence of coronal holes are measured using EIT images from 1996 through 2011. The measured total area of coronal holes varies between 15% and less than 5% of total solar surface area, and the total unsigned open flux varies from 5×10^{22} Mx (1996-1997), to 2×10^{22} Mx (2000), back to 5×10^{22} Mx (2003), and then 2×10^{22} Mx since 2006. There is a good agreement between these results and the previous study by Harvey & Recely (2002) of polar holes using He I 10830 data during the period 1996 through 2000, when both data are analyzed. The two studies yield comparable measurements of polar hole area, open flux, and their annual variations. When compared with the PFSS model, it is shown that the model and EIT measurements exhibit similar global patterns of coronal hole coverage particularly in high-latitude (> 65 degrees) polar regions, as well as similar solar cycle dependence of open flux consistent with model results by Wang (2009) and IMF measurements by Yeates et al. (2010). However, the model yields larger area and more open flux than observed, particularly in lower latitude areas and during the solar maximum. There is also a large discrepancy in both area and flux during the extended past solar minimum from 2006 - 2011, even though the two measurements show the same evolution trend in general.

Measurements are made with AIA-EUVI observations from 2010 May through 2013 January, and compared with EIT observations as well as the PFSS model results. It is found that the better quality of EUV images by AIA-EUVI allows a more accurate detection of coronal holes in middle-low latitudes that are often under-represented or even missed by EIT. As a result, during 2010 - 2013, AIA-EUVI measures larger total hole area to be between 5-10% of the total surface area, with dominant contribution from middle-low latitudes; it also measures significantly enhanced total open flux in the range of $2\text{-}4 \times 10^{22}$ Mx, which is about twice the flux measured by EIT, and matches with the PFSS calculated open flux. Nevertheless, there is a large discrepancy between AIA-EUVI measurements and PFSS results in terms of the latitude-dependence of coronal holes and open flux. PFSS appears to over-estimate the areas of coronal holes in the middle-latitudes that are extended from the polar holes, yet does not recover adequately holes in the lower latitudes as seen by AIA-EUVI.

To summarize, this comparative study of three different measurements (EIT, AIA-EUVI, and PFSS) of persistent coronal holes and open magnetic flux suggests that coronal holes in low-latitudes are important to contribute to total open flux. On the other hand, these holes are not well measured with either the chromosphere He I 10830 line in the past or EIT EUV images shown in the present study. Neither does the static PFSS model adequately produce lower latitude holes observed by AIA-EUVI, even though the measured and computed total open flux happen to match.

It has been discussed in the past that there is ambiguity in determining weaker or smaller coronal holes in the lower latitudes with the He I 10830 observations (Levine, 1982), and that coronal (SXR and EUV) and chromosphere (He I 10830) observations of these low-latitude holes often do not agree (Kahler et al., 1983; Schrijver & De Rosa, 2003; Malanushenko & Jones, 2005). This discrepancy may result from an expansion of coronal holes with height. This study demonstrates that the AIA-EUVI EUV imagers are capable of uncovering many low-latitude holes compared with the EIT instrument. It should be noted that, given the analysis cadence of 24 hours for EIT and 12 hours for AIA/EUVI, most of these holes are long-lived persistent holes, as evidenced by the fact that the hole boundaries found in AIA images are very similar to those defined in STEREO-EUVI images.

From the point of view of models, Lepri et al. (2008) performed an MHD simulation of the steady-state magnetic field, and argued that PFSS reconstruction may have included active region contributions, and over-estimated the total steady-state open flux. Our observations comparing the latitude-dependence of open flux suggests that, whereas EIT measurements underestimate the low-latitude contribution, the PFSS may over-estimate this contribution by reproducing overall larger open areas than observed with AIA-EUVI. It was also put forward that the reconstructed total IMF, which is usually very large and comparable with the PFSS calculated flux, is due to the contribution of CME related open fluxes (Riley, 2007; Antiochos et al., 2012). These events tend to be short-lived and occur near active regions in low-latitudes. To appropriately capture their contribution, it will be important to analyze the AIA-EUVI full surface observations at higher cadence. Even though the full-surface EUV observations are still limited by the one-side view of the magnetic field, tracking coronal hole evolution and detecting short-lived holes on the backside will provide indirect constraint to models that are used to calculate the open flux. For example, as suggested by Mackay & Yeates (2012) in addition to other techniques to evolve the photospheric magnetic field (Schrijver & De Rosa, 2003), the boundary condition may be further controlled, or model assumptions varied, in advanced MHD models to reproduce observed coronal hole properties on the full surface.

CORONAL HOLES AND OPEN FLUX IN SOLAR CYCLES 23 AND 24

Contribution of Authors and Co–Authors

Manuscript in Chapter 3

Author: Chris Lowder

Contributions: Conceived and implemented study design. Constructed code to analyze data sets. Wrote first draft of the manuscript.

Co–Author: Dr. Jiong Qiu

Contributions: Helped to conceive study. Provided feedback of analysis and comments on drafts of the manuscript.

Co–Author: Dr. Robert Leamon

Contributions: Helped to conceive study. Provided feedback of analysis and comments on drafts of the manuscript.

Manuscript Information Page

Chris Lowder, Jiong Qiu, Robert Leamon
The Astrophysical Journal
Status of Manuscript:
_x_ Prepared for submission to a peer–reviewed journal
____ Officially submitted to a peer–reviewed journal
____ Accepted by a peer–reviewed journal
____ Published in a peer–reviewed journal

Introduction

Coronal holes are the observational signature of regions of open solar magnetic field. Early observations were conducted in extreme ultraviolet (EUV) wavelengths (Tousey et al., 1968). Magnetic field lines within the solar corona can either connect back down to the solar surface or extend outward into the heliosphere, denoting closed and open field respectively. In regions of open magnetic field, coronal plasma is free to follow these field lines outward, creating the solar wind and a plasma density depletion at the field footpoints. Appearing as dark regions in x-ray and extreme ultraviolet (EUV) images, coronal holes correspond with reduced emission from solar plasma localized to open magnetic field footpoints (Wang, 2009). Cranmer (2009) discusses a complete review of coronal holes in exhaustive detail.

The sun's open magnetic field and coronal hole structure varies alongside the overall solar activity cycle, running through a magnetic polarity swap every 11 years. The connection between coronal hole activity and open magnetic flux throughout the solar cycle has been considered by several studies (Harvey & Recely, 2002; Wang, 2009). Harvey & Recely (2002) assessed the properties of polar coronal holes throughout solar cycles 22 and 23. Using a series of He I 10830 Å spectroheliograms, polar coronal holes were identified over the period 1989 September to 2002 March, measuring area and enclosed magnetic flux. They found that polar coronal holes throughout this period develop initially at lower latitudes of about 50-60 degrees, and extend over within three subsequent rotations. These polar coronal holes then have a lifetime observed between 8.3 and 8.7 years. An asymmetry was observed in the timing of initial appearance and evolution, with a difference of several months between poles. This mirrors earlier observations by Webb et al. (1984), who found a lag of 9 and 6 months between polar coronal hole appearances between cycles 19-20 and 20-21, respectively. The relative areal extent of each polar coronal hole can also show an asymmetry from solar cycle to the next (Broussard et al., 1978; Sheeley, 1980). More recent work by McIntosh et al. (2013) explores the hemispheric asymmetry of photospheric magnetism throughout cycles 23 and the early stages of cycle 24. While He I 10830 Å observations of coronal holes can provide accurate results in polar regions, there is discrepancy at lower-latitudes (Kahler et al., 1983; Schrijver & De Rosa, 2003; Malanushenko & Jones, 2005).

Despite the relatively long history of observations of the solar activity cycle, continuous and full-disk magnetic field and solar corona observations extend back only to cover the previous two cycles. SOHO begin this observational campaign from 1995 through 2011, with results from SDO picking up since 2010 May. McIntosh et al. (2014) recently conducted a comprehensive analysis of observations by these spacecraft, showing that distributions of EUV bright points and structures of surface magnetic elements, characterized by the magnetic range of influence (MRoI), both migrate from high latitudes (±55 degrees) toward the equator in a time period of 19 years. In addition, the evolution of low-latitude coronal holes and records of coronal green line emissions also overlaps with this trend. Observing the progress of the activity bands formed by these very different features helps decipher the underlying solar magnetism in a cycle structure.

Among these features, coronal holes map the foot-prints of open magnetic field at locations that vary along with the solar cycle. McIntosh et al. (2014) show that low-latitude coronal holes migrate towards the equator as the cycle progresses, whereas during solar minimum holes exist primarily in polar regions, a spot where EUV bright points and coronal green line emission is sparse. These are the areas of crucial importance in the solar magnetic activity cycle. The polar region is usually dominated by magnetic field of one polarity, and each cycle begins with the reversal of this polarity at the end of the solar minimum, when meridional convective flow has recycled the field to the poles and flux cancellation takes place (Upton & Hathaway, 2014). Existing models of global solar magnetic field often make the point to focus on comparison of model computed open field with the observed coronal holes at the poles, or with the total heliospheric open magnetic flux (Mackay et al., 2002a,b; Yeates et al., 2010). On the other hand, much effort is also needed to examine coronal holes evolving across the latitudes. Tracking open magnetic flux on the Sun following coronal hole evolution from the poles to the low-latitudes adds a valuable piece to the puzzle of solar magnetic activity cycle.

The continuous full-disk coronal and magnetic field observations in the past two decades provide the opportunity to study evolution of coronal holes and open magnetic flux in solar cycles 23 and 24. Lowder et al. (2014, referred as Paper I hereafter) have developed an automated technique to detect persistent coronal holes and characterize their properties using a database of full-disk EUV images obtained by several spacecraft instruments over a time span from 1996 May to 2013 January. In this present study, we use the same technique and the same database which however is further extended to 2014 August. The extended database covers a significant portion of the current solar cycle 24, and hence provides an opportunity to compare coronal hole properties between the past cycle 23 and this special new cycle, which, after a much unexpected deep minimum, slowly set in around 2010 and dwelled into a low maximum in early 2014 (McIntosh et al., 2015).

Lowder et al. (2014) have also measured coronal hole areas, and the unsigned and signed total flux measured in these holes, distinguishing polar regions from low-latitudes with an arbitrary division at ±65 degrees. This chapter will present a more careful and detailed examination of the latitude dependence of coronal hole properties not illustrated in Paper I, and a contrast between the consecutive two cycles is apparent. In the following text, a brief review of the database and technique is presented in Section 2 for completeness. Section 3 presents the latitude dependence

Table 3.1. Data coverage for each instrument source

		Start		End	
Source	Observable	CR	Date	CR	Date
SOHO/EIT	EUV 195Å	1909.96	1996 05 31	2105.27	2010 12 31
SDO/AIA	EUV 193Å	2096.76	2010 05 13	2153.92	2014 08 19
STEREO/EUVI	EUV 195Å	2096.76	2010 05 13	2153.92	2014 08 19
WSO Harmonics	B_r	1893.00	1995 02 23	2140.00	2013 08 04
Synoptic *SOHO*/MDI	B_r	1911.00	1996 06 28	2104.00	2010 11 26
Synoptic *SDO*/HMI	B_r	2096.00	2010 04 22	2156.00	2014 10 14

of coronal hole properties and their variations from the last cycle to the current cycle, followed by conclusions and discussions in the last section.

Methodology and Data

The *Extreme-ultraviolet Imaging Telescope* (EIT; Delaboudinière et al., 1995), an instrument aboard the *Solar and Heliospheric Observatory* (SOHO), has provided fourteen years of nearly continuous EUV observations over the span of solar cycle 23. The *Solar Dynamics Observatory* (SDO) was launched in 2010, continuing the role of a provider of synoptic EUV observations through the EUV telescope *Atmospheric Imaging Assembly* (AIA; Lemen et al., 2012). Having launched a few years prior, the twin spacecraft *Solar Terrestrial Relations Observatory* (STEREO) A and B have swept out a significant portion of vantage points on the far-side of the sun. Employing the *Extreme Ultraviolet Imager* (EUVI; Howard et al., 2008) on each of the STEREO spacecraft, additional viewpoints are available in the EUV. The particular combination of EUV data from *SDO*/AIA and *STEREO*/EUVI A&B allows for a unique observational opportunity. As the STEREO spacecraft have swept out in their orbits, expanded heliographic longitude coverage in EUV was made possible. Additionally, polar EUV coverage was expanded through more staggered B-angle for each of the spacecraft in use. Joint observations by the three spacecraft complement one another to provide better coverage of the polar areas, important regions contributing to the evolution of solar open magnetic flux. The joint AIA/EUVI coverage makes possible continuous, consistent, and nearly-full solar surface observations of coronal hole boundaries over solar cycle 24. Table 3.1 displays the relevant datasets used in this study, and the corresponding availability ranges. Using these data ranges, coronal hole boundaries are characterized over one and one half solar activity cycles, and compared between cycles 23 and 24.

To provide context of the solar cycle dependence of coronal hole properties, Figure 3.1 displays the observational spacecraft B-angle in comparison with position in the solar activity cycle. Some of this data was featured in the prior study, however, here this range is extended to cover through 2014 August (Lowder et al., 2014, Figure 13). The upper panel displays the monthly hemispheric sunspot number (WDC-SILSO, Royal Observatory of Belgium, Brussels), with the northern and southern sunspot counts in red and blue, respectively, with the dominant pole shade filling

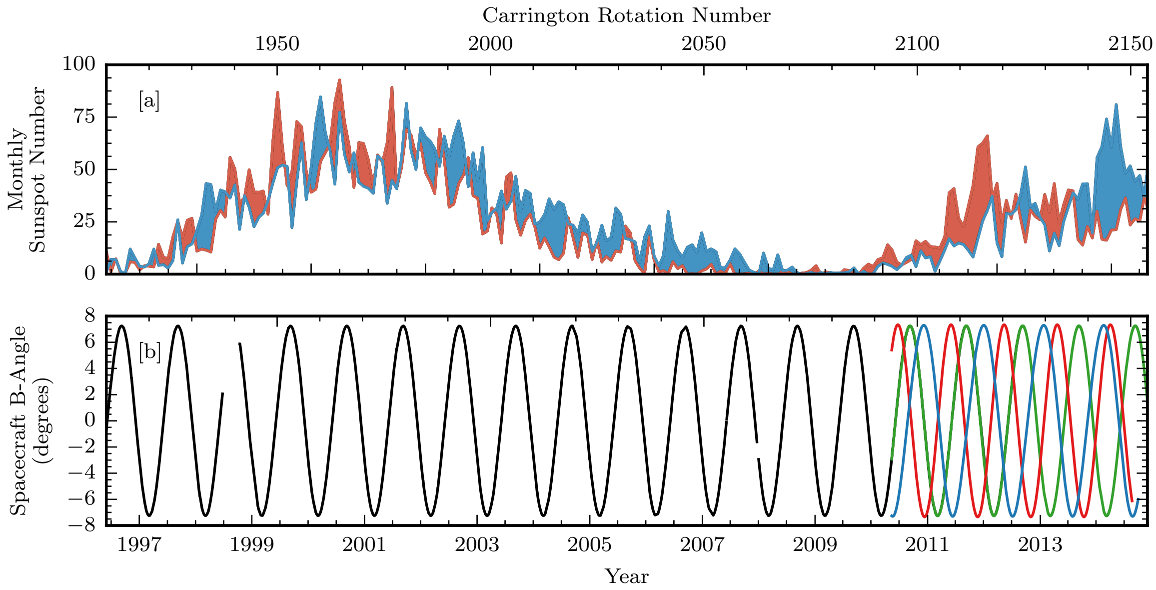

Figure 3.1. [a] Hemispheric sunspot number for northern and southern hemispheres in red and blue, respectively. (WDC-SILSO, Royal Observatory of Belgium, Brussels) [b] Spacecraft solar b-angle over the course of observations in Table 3.1. *SOHO*/EIT (black), *SDO*/AIA (green), *STEREO*/EUVI A (red), and *STEREO*/EUVI B (blue) angles are displayed.

between. The bottom panel displays the spacecraft B-angle for *SOHO*/EIT (black), *SDO*/AIA (green), *STEREO*/EUVI A (red), and *STEREO*/EUVI B (blue). Using the single vantage point of *SOHO*/EIT, our polar observations are limited by this angle. This will become apparent in subsequent figures. Rather than attempting a convoluted methodology to correct or estimate for this lack of coverage, results are displayed unmodified. With the combination of *SDO*/AIA and *STEREO*/EUVI A/B, this polar coverage gap is greatly reduced. In comparing with our gauge of solar activity cycle, note that our EIT observations span over the entire first solar cycle under consideration here. Our improved polar coverage from STEREO begins conveniently just as the next solar cycle gets underway.

With these data, techniques have been developed and documented for the automated detection of coronal hole boundaries, detailed in the previous chapter and in literature (Chapter 2: Lowder et al., 2014). In brief, each frame of EUV data is analyzed via an instrument-independent intensity thresholding method to mark out coronal hole boundaries. Boolean maps of suspected coronal hole regions are generated and mapped into a Carrington Equal Area (CEA) projection, and then segmented and catalogued into individual regions through a watershed method. For our SOHO-era (solar activity cycle 23) data, this process is repeated for each time-step, with half of the solar surface not visible. Full rotation maps are built by summing these individual EIT hole maps over each Carrington rotation, and then flattening into a boolean map. For the SDO-era (solar activity cycle 24) data, thresholded projections are made individually for each of our three datasets (*SDO*/AIA and *STEREO*/EUVI A/B), and then summed and flattened into one resulting boolean map.

This initial mapping detects both coronal holes and filament channels, which both appear as dark features in EUV. Here we use the underlying magnetic flux density information to distinguish the two. Filament channels stride along magnetic polarity inversion lines, encompassing roughly equal distributions of positive and negative flux. In the encompassed area of a coronal hole, a single magnetic polarity dominates

(Cranmer, 2009). Therefore, we calculate the skew of magnetic flux density in each candidate coronal hole region, using magnetograms by Michelson Doppler Imager (MDI, Scherrer et al., 1995) in conjunction with *SOHO/EIT*, or (HMI, Scherrer et al., 2012) with *SDO*/AIA and *STEREO*/EUVI A&B. Regions with a relatively small skew are considered to be filament channels and are therefore ‘sieved’ out, leaving behind a boolean CEA map of coronal hole pixel locations.

For the current application of this routine for the consideration of long-duration coronal hole evolution, EUV data cadence is as follows. *SOHO*/EIT data are assimilated daily, with a resulting daily coronal hole map. These daily maps are then summed and flattened to provide an upper estimate over an entire solar rotation, to account for missing far-side data. *SDO*/AIA and *STEREO*/EUVI A&B data are gathered at a cadence of 12-hours, providing two full-surface coronal hole maps per day. Note that with the expanded longitudinal and polar coverage, these maps are considered individually, without the requirement of summing over an entire solar rotation.

For more details and intermediate results on this process, see Lowder et al. (2014). While this code and methodology was until now unnamed, a graduate student must name a code. Henceforth, for the sake of brevity, this code and methodology will be referred to as the Global Automated Coronal Hole Detection routine (GACHD). In the present chapter, the techniques have been further refined, and applied to the complete data range from 1996 May 31 to 2014 August 19, the furthest data available until the recent communication loss with one of the STEREO spacecraft. These data cover the entire past cycle 23 as well as a large portion of the current solar cycle 24.

Coronal Hole Properties in Solar Cycles 23 and 24

Using this dataset of coronal hole boundaries, spanning over one and one half solar cycle in length, a few interesting quantities can be considered. Notably these include the area as well as the signed and unsigned magnetic flux enclosed by coronal hole boundaries. Rather than considering just the polar coronal hole properties, our data extend across all latitudes to characterize the latitude-dependence of these properties and their evolution.

In this section, we will first present the time-latitude maps of coronal hole properties. The total magnetic flux in the holes is then presented, comparing the polar regions with low-latitudes, and the past cycle 23 with the current cycle. For the following set of figures, there are two notes of importance. Figures 3.2, 3.3, 3.4, and 3.5 display quantities over the full time span from 1996 May to 2014 August, illustrating the solar cycle dependence of the measured properties. Figures 3.6, 3.7, 3.8, and 3.9 provide a ‘zoomed-in’ display of identical quantities from 2010 May onward, over the SDO and STEREO-era data for solar cycle 24. Over all of these plots, panel (a) displays the monthly hemispheric sunspot number in red and blue, for the northern and southern sunspot counts, respectively. This panel will lead some of the following figures for an easily markable solar activity cycle cross-reference tool.

It should be noted that a partial overlap with the results Lowder et al. (2014) exists within Figures 3.3, 3.4, and 3.5. However, results contained here use an alternative latitudinal definition of polar regions. Additional data extends the range of results to cover a more significant fraction of cycle 24.

Latitude Coronal Hole Profiles

Consider Figure 3.2, displaying the full latitude dependence of our coronal hole quantities over the full timespan of our datasets. Of immediate note, distributions of the coronal hole area (panel b), and the mean magnetic field (panel c) and total unsigned magnetic flux (panel d) in the holes all exhibit distinctive evolution patterns across ±55-degrees latitude, which are marked by two horizontal lines in the figures.

These particular latitudes, ±55-degrees, have been noted previously as a demarcation of certain solar activity. Thompson et al. (1996), using the Global Oscillation Network Group (GONG) set of observations, considered the internal rotation rate of the sun, from the surface deep into the convection zone. A slice through the convection zone reveals the internal structure of the differential rotation, beneath the photospheric surface flow. At ±55-degrees latitude, there is a distinct change in the behavior of these subsurface flows.

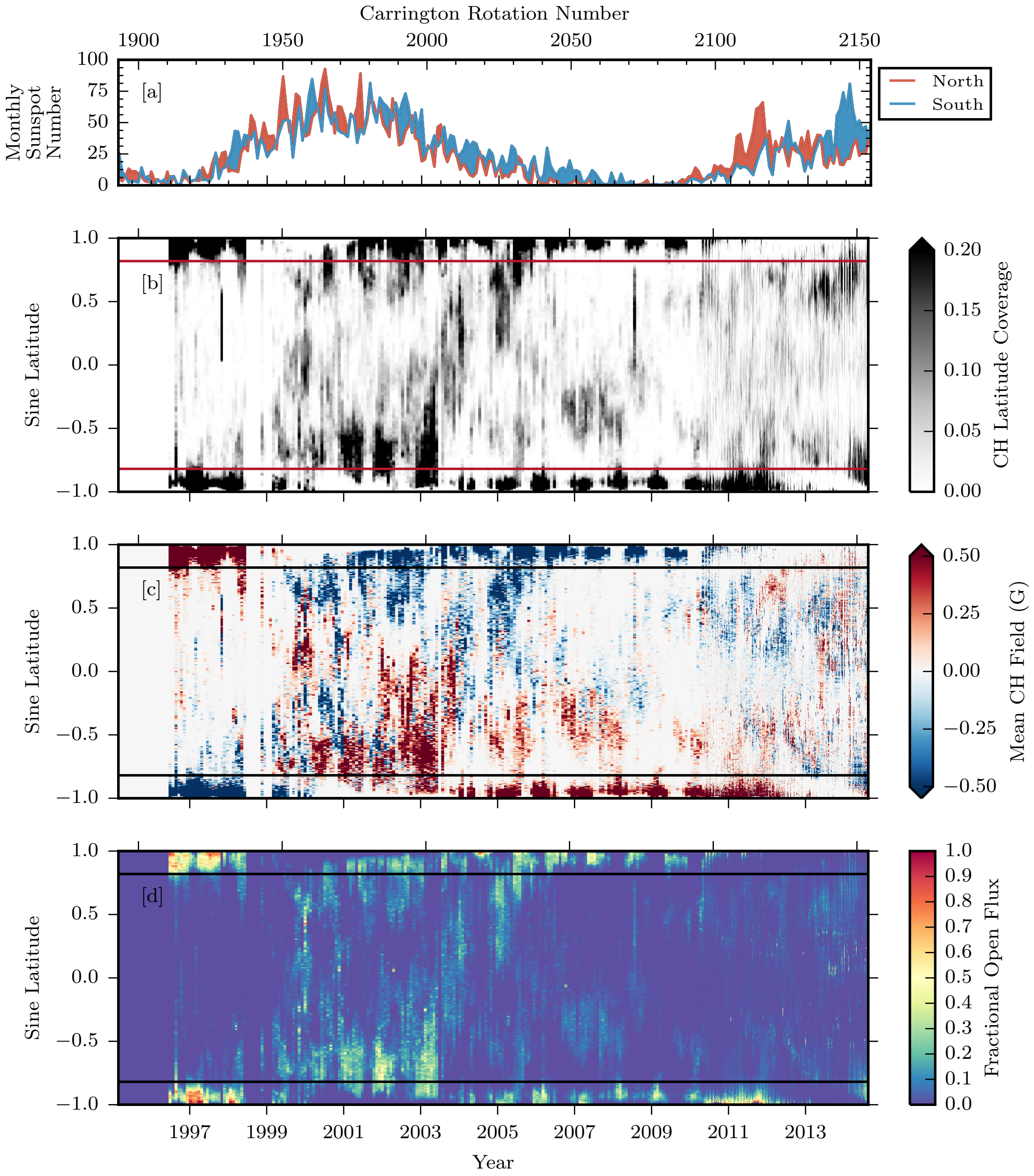

Figure 3.2. For the time period 1996 May 31 to 2014 August 19: [a] Monthly hemispheric sunspot number for the northern (red) and southern (blue) hemispheres (WDC-SILSO, Royal Observatory of Belgium, Brussels). [b] Coronal hole latitude profile of coverage, integrated over longitude. Horizontal red lines are marked at ±55 degrees latitude, to distinguish polar and low-latitude zones. [c] Latitude profile of coronal hole dominant polarity, integrated over longitudes. [d] Latitude profile of coronal hole enclosed magnetic flux, integrated over longitudes.

Spruit (2011), in an effort to sketch out a few theories of internal solar dynamo processes, devised a simple model. Starting with a uniform poloidal field, a differential rotation profile from observations was applied. This resulted in a shearing of the field, which can eventually lead to a buildup of azimuthal field and an instability. From this simple model, the azimuthal field builds as $\partial_t B_\phi \sim \sin 2\lambda(1 + 1.51 \sin^2 \lambda)$. As a function of latitude, this maximum shearing occurs right around ±55 degrees.

This latitude was further revealed as a zone of interest by McIntosh et al. (2014, 2015), who found a scarcity of EUV bright points above this latitude, as well as a distinct evolution pattern of the magnetic range of influence (MRoI) divided by this latitude. Therefore, in the following analysis, ±55 degrees latitude is chosen as the division between polar and low-latitude regions. Note that this distinction of polar regions differs from the previous study by Lowder et al. (2014), which used ±65 degrees latitude as a separator.

Panel (b) displays for each timeframe and bin of sine latitude the fraction of longitude bins that are characterized as coronal holes, with the color mapping truncated at 0.2 for display purposes. Note that this fraction varies from 0 (no coronal holes at any longitudes at that particular latitude) to 1.0 (complete coronal hole coverage at every longitude for that particular latitude). From 1996 to 1998, and from 2006 through 2012, coronal holes are concentrated in the polar regions above ±55-degrees. Apparent annual variation in the polar hole area is not a physical results, but rather a consequence of the solar B-angle modulation of the *SOHO* spacecraft (see Figure 3.1). The single vantage point of these observations results in alternating reduced polar coverage. From 2010, with the combination of the AIA/EUVI suite of data, staggered spacecraft B-angles allow for more comprehensive polar measurements. During the solar maxima from 1999 to 2003, and then from 2012 through 2014, coronal holes extend to low-latitudes below ±55-degrees, and are diminished in polar regions.

Figure 3.2-(c) displays the mean magnetic field strength encompassed by coronal hole boundaries, averaged over all longitude bins for each bin of sine latitude. Using synoptic magnetograms from *SOHO*/MDI and *SDO*/HMI, coronal hole enclosed magnetic flux (signed and unsigned) is integrated over all longitudes. To avoid the contribution of noise for both signed and unsigned flux calculations, instrument-specific noise levels are used to remove magnetic flux density measurements below this noise threshold. For MDI synoptic chart measurements of radial magnetic flux density this noise level is measured as ±5.0 G, while for similar synoptic measurements from HMI this noise is measured as ±2.3 G (Liu et al., 2012). While the range of integrated values ranges from -8.4 to 14.3 G, here the map is displayed truncated at ±0.5G to illustrate the often-weak polarity dominance at lower latitudes. The resulting map displays the distribution of the dominant polarity of coronal hole enclosed magnetic flux and its evolution over the solar cycle. These distributions of

dominant coronal hole polarity exhibit a hemispheric pattern over the course of the solar cycle. In the rise of the previous cycle before 1999, the northern polar coronal hole distribution is dominated by positive magnetic field, with the southern polar coronal hole dominated by negative field. At lower latitudes, this same general polarity trend is observed, albeit at a much lower strength, usually below 1 G, and not as spatially uniform across latitudes and time. During the 2001-2003 solar activity maximum, the hemispheric field reversal is observed in the swap of the polar coronal hole dominant polarity, persisting until 2012. For the current cycle, the reversal of the dominant polarity in polar regions begins in 2012 and 2013 for the northern and southern hemisphere, respectively. However, the resulting polar coronal hole coverage and polarity dominance have been very weak in comparison with the prior cycle. In lower latitudes during the current cycle, the distribution of coronal hole polarity dominance is much weaker in strength and spatially mixed.

Figure 3.2-(d) displays the fractional unsigned open flux, collected by summing all coronal-hole-encompassed-flux over longitude bins for each time and sine latitude bin. An identical noise cutoff of the synoptic magnetogram is used for this calculation to avoid including instrument noise. Note that the range of calculated open flux ranges from 0 to 4.7×10^{20} Mx, with displayed data represented as a fraction of the maximum measured. With a sine-latitude coordinate system, broken into 1440 pixel latitude bins, each pixel represents an equal solar surface area. This allows for comparison

of the relative strength of open flux sources at polar and low-latitude regions. From 1997-1999 the polar coronal holes contain the majority of the open magnetic flux. As the poles reverse as solar activity ramps up, larger concentrations of open flux appear at lower latitudes between 1999 and 2003. Past cycle 23 maximum, this pattern quickly returns to larger concentrations of open flux in the poles, until the next reversal around 2013. In the southern pole, concentration of coronal hole flux persists for the extended deep minimum until the next reversal around 2013. This particular cycle from 2009 onward has shown unique behavior in the early drop-off of the northern polar coronal hole signature. This in turn has resulted in almost nonexistent open-flux from the northern polar region.

In concluding this portion of the analysis, we note that McIntosh et al. (2014, 2015) has also reported the solar cycle dependence of coronal holes observed in much the same time range. However, their study has only captured coronal holes with area greater than 20,000 Mm^2 at the low latitudes (below ±55 degree). By employing joint observations by AIA/EUVI, our study not only provides a more complete coverage of polar holes from 2010 May, but also allows the assessment of polar hole measurements by EIT in the past cycle through comparison of measurements by different instruments, as will be further discussed in Sections 3.2 and 3.3.

Coronal Hole Area

Figure 3.3 breaks down the latitude dependence of the coronal hole areas in Figure 3.2 into the distinct ranges of Northern Polar (NP; 55:90 degrees), Low Latitudinal (LL; -55:55 degrees), and Southern Polar (SP; -90:-55 degrees). EIT and the combination of AIA/EUVI are displayed in red and blue, respectively. Note here that EIT measurements of area are integrated over each solar rotation, providing a measurement of area within observable regions. The brief overlap of EIT and AIA/EUVI observations in the second half of 2010 demonstrate that, as also discussed in Lowder et al. (2014), the joint AIA/EUVI observational coverage allows better estimates of polar coronal hole areas and fluxes.

Figure 3.3-(b) displays the entire range of latitudes, from -90:90 degrees. The total area of coronal holes over the course of this study varies between 1-7$\times 10^{21}$ cm^2, or from 2% to 12% of the total solar surface area. Of immediate note is the relative lack of coronal hole area throughout the current solar cycle, the maximum hole area being less than 70% of that in the past cycle.

Figure 3.3-(c-e) display the latitude zones under consideration, where we can note a few things. The northern coronal hole has dropped from 2011 onward, hovering around zero area, and has never recovered to the prior 2009 level. The southern pole area was still rising from 2011, and suffered a drop in middle 2012, but has since

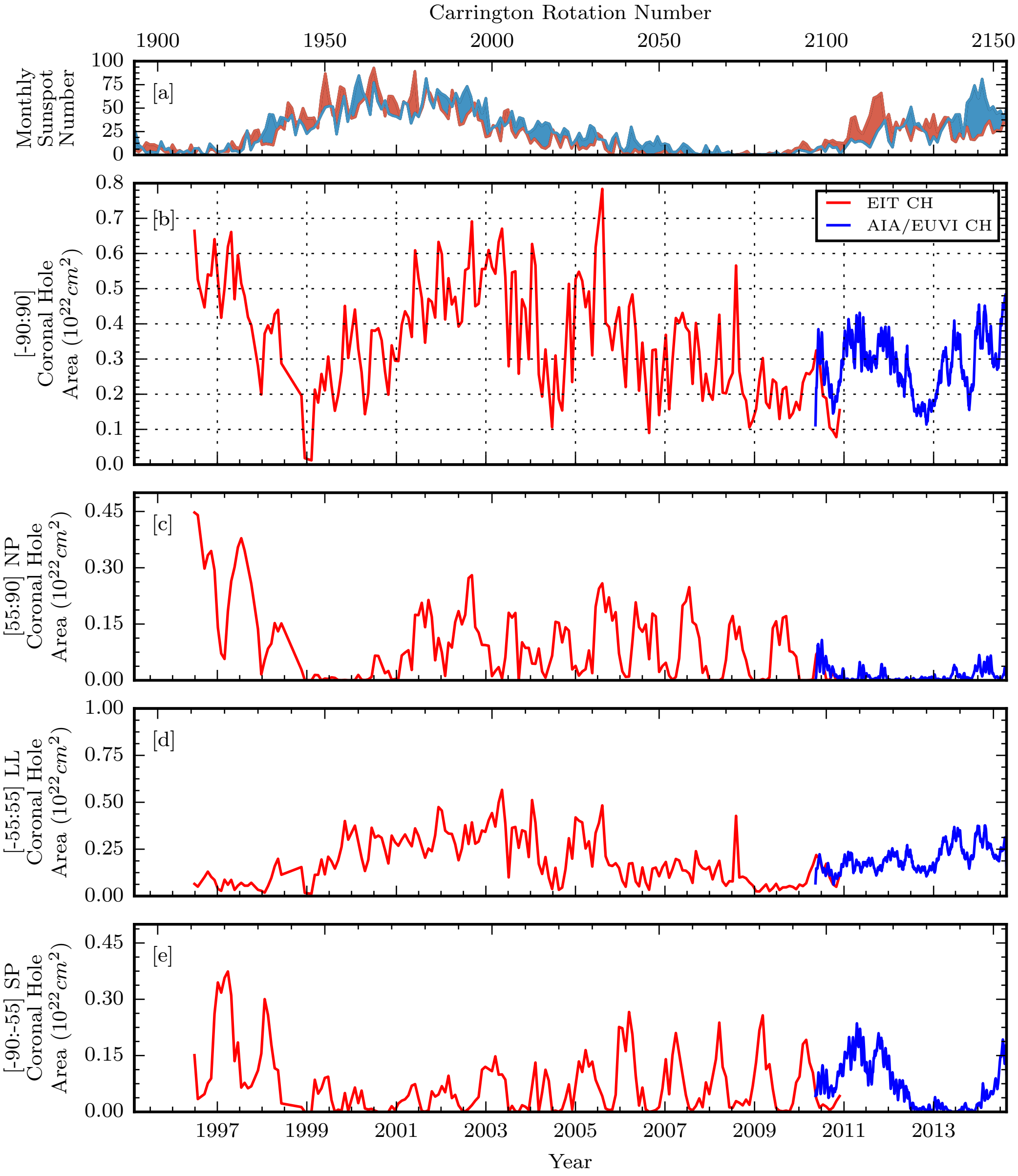

Figure 3.3. Comparisons of coronal hole area and associated quantities over the entire data span. [a] Hemispheric sunspot number for northern and southern hemispheres in red and blue, respectively. (WDC-SILSO, Royal Observatory of Belgium, Brussels) [b] Total coronal hole area, for a few sources. EIT and AIA/EUVI coronal hole boundaries are used to compute the coronal hole area in red and blue, respectively. [c-e] Coronal hole area computed for northern polar, low latitudinal, and southern polar regions.

recovered from 2014 onward. In comparing with the previous cycle drop in polar coronal hole area from 1999-2001, this behavior is highly asymmetric.

In both cycles, low-latitude coronal holes cover a large area during the solar maximum, and consequently is the source of a significant amount of total open flux on the Sun during the solar maximum. Again, in the current cycle 24, the low-latitude coronal hole area is notably smaller than in the last cycle.

Unsigned Magnetic Flux

In a similar manner, Figure 3.4 breaks down the latitude dependence of the unsigned open magnetic flux encompassed by our coronal hole boundaries. Figure 3.4-(b) displays the total unsigned open flux, with several datasets in place. EIT and AIA/EUVI coronal hole encompassed unsigned flux are plotted in red and blue, respectively. These direct measurements are compared with the open flux calculated by the potential field source surface (PFSS) model (Schatten et al., 1969; Wang & Sheeley, 1992). This model calculates the magnetic potential field using WSO spherical harmonics of photospheric radial magnetic field as the lower boundary, and with the source-surface defined at $2.5R_{\odot}$, where field lines are assumed open. An array of field lines are traced down from this source-surface to their photospheric origin, and are mapped out as the boundaries of open magnetic field. Magnetic fluxes are then computed by integrating the photospheric radial magnetic field within these open footpoint boundaries. Note that while WSO observations are used as a boundary

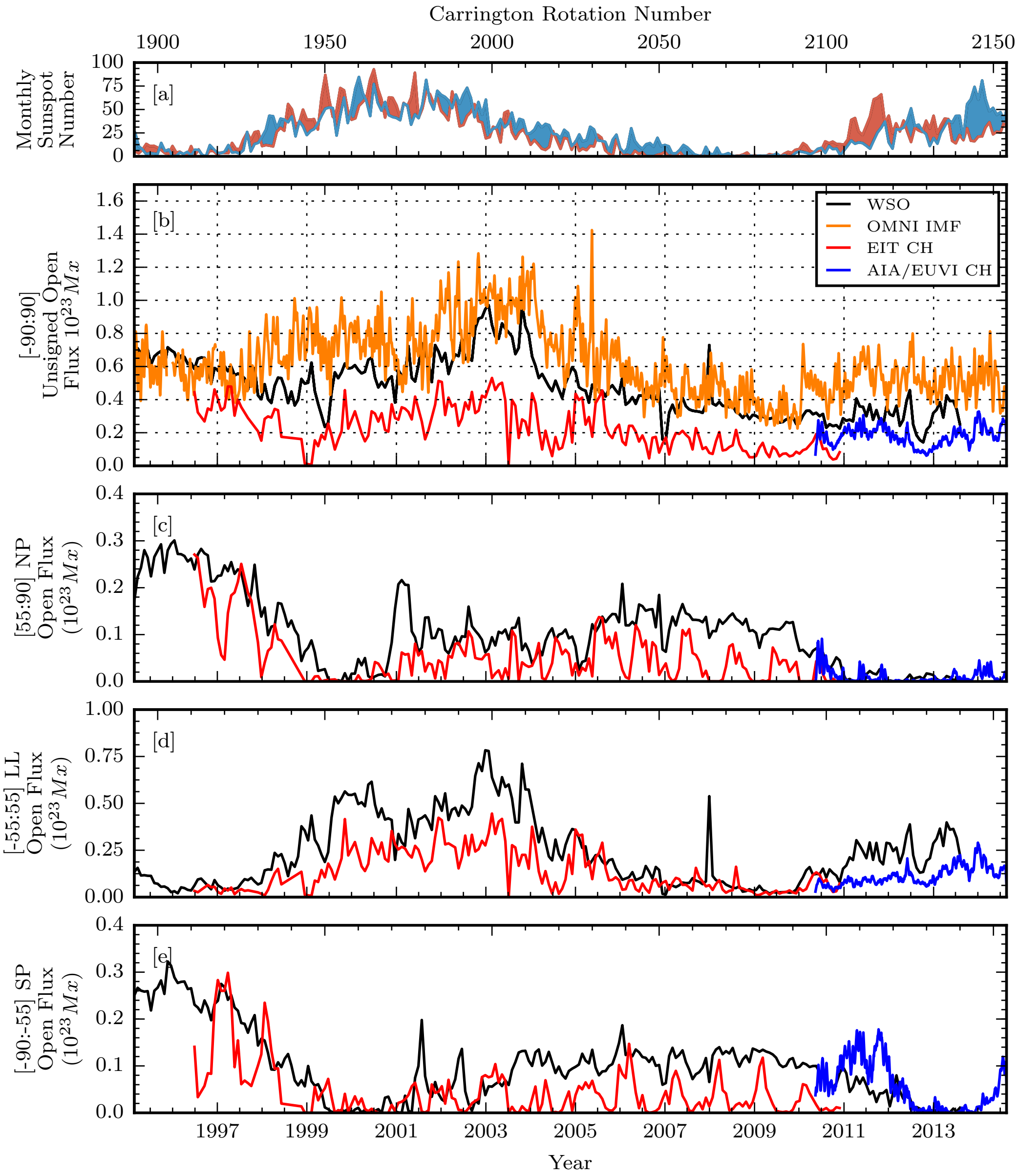

Figure 3.4. Comparisons of unsigned photospheric flux and associated quantities over the entire data span. [a] Hemispheric sunspot number for northern and southern hemispheres in red and blue, respectively. (WDC-SILSO, Royal Observatory of Belgium, Brussels) [b] Total unsigned open magnetic flux, for a few sources. WSO data in black is computed from total open field boundaries. EIT and AIA/EUVI coronal hole boundaries are used to compute the total enclosed magnetic flux in red and blue, respectively. OMNI $|B_r(r = 1AU)|$ is used to compute an equivalent open magnetic flux, displayed in orange. [c-e] Open magnetic flux computed for northern polar, low latitudinal, and southern polar regions.

condition, the calculated open flux is a PFSS model output using this observational input. For the purposes of comparison with other model results, this dataset may be referred to as 'observational' in comparison, referring to the observational basis of model input. The resulting unsigned open magnetic flux from this PFSS model is displayed in black.

The measured open flux from the EIT coronal holes undershoots the values predicted by the PFSS model, partially due to a contrast issue with *SOHO*/EIT (Chapter 2: Lowder et al., 2014). This issue is most prevalent in lower-latitude regions during periods of higher solar activity. AIA/EUVI measurements reveal additional open flux as compared with EIT alone during the overlapping period in the second half of 2010, as a result of more complete coverage of the polar regions by the AIA/EUVI dataset. This additional flux sets the AIA/EUVI dataset more in line with the PFSS model.

Finally, the OMNI dataset is used to compute an equivalent open magnetic flux. In-situ (Lagrange point L1) measurements of the B_x component (Geocentric Solar Ecliptic; GSE) of the magnetic field extend backward for decades through a cross-spacecraft calibrated dataset (King & Papitashvili, 2005). The OMNI data were obtained from the GSFC/SPDF OMNIWeb interface at http://omniweb.gsfc.nasa.gov. For this study we focus only on the previous two decades. If we make the assumption that our long-term interplanetary magnetic field is uniform and radial, the equivalent

OMNI unsigned open magnetic flux can be computed as $\Phi_{OMNI} = 4\pi R_{L1}^2 |B_x|$ (Lockwood, 2002). During solar minimum periods, the OMNI data and PFSS model are in better agreement than in periods of higher solar activity.

Figures 3.4-(c-e) display the coronal hole unsigned open flux for the latitude zones demarcated by ±55 degrees latitude. Similar evolution patterns are observed with regard to cyclic variation and latitudinal dependence, as compared with measurements of coronal hole areas. In the polar regions, the lack of coverage during the EIT-era dataset is apparent, as a consequence of B-angle variation. However, the peak values of EIT coronal hole area and unsigned open flux provide an upper bound on this value, fully observing each pole over an entire rotation. Considering the upper bounds of the EIT data, good agreement is found with the PFSS open flux in polar regions. This trend continues with AIA/EUVI data, albeit with more complete coverage of the polar regions. Such comparisons allow us to state as an immediate conclusion, that the magnetic open flux in polar regions computed with the PFSS model is generally consistent with direct measurements in both solar cycles.

In terms of the solar cycle dependence of open flux in the poles, for solar cycle 23, the unsigned open flux in the northern and southern poles evolved in a mostly symmetric manner. But an asymmetry presented itself with solar cycle 24, just as with the evolution of the coronal hole areas. For this cycle, the northern polar unsigned open flux drops off to nearly zero around 2011, and continues to hang there. Slight signs of the beginning of a recovery are apparent in 2014, but with no clear recovery trend. The southern pole open flux drops to zero in 2013, two years later than the northern poles, and then begins to rise once again.

Consideration of the low-latitude open flux reveals the discrepancy during periods of maximum solar activity, where low-latitude coronal holes border close to larger concentrations of magnetic flux.

Signed Magnetic Flux

Figure 3.5-(b-d) displays the signed open magnetic flux from each of the latitude zones demarcated by ±55 degrees. Considering the low latitude region of Figure 3.5-(c), the signed open flux hovers around zero. This is expected, as overall low-latitude extensions from polar coronal holes as well as low-latitude coronal holes themselves should appear from both magnetic polarities. One notable exception occurs around solar maximum for solar cycle 23 in 2001-2003. Here, our coronal hole (EIT) and PFSS open field (WSO) datasets both show a deviation from this behavior, with more pronounced variability. As solar activity progresses and peaks, it is expected that certain polarities will happen to dominate over some timescales. For the next solar maximum, note that the behavior of the signed open flux is much more subdued in this variation.

For the northern and southern polar regions, Figure 3.5-(b,d), the polarity dominance is more apparent. During the lull in solar activity around 1997 before cycle

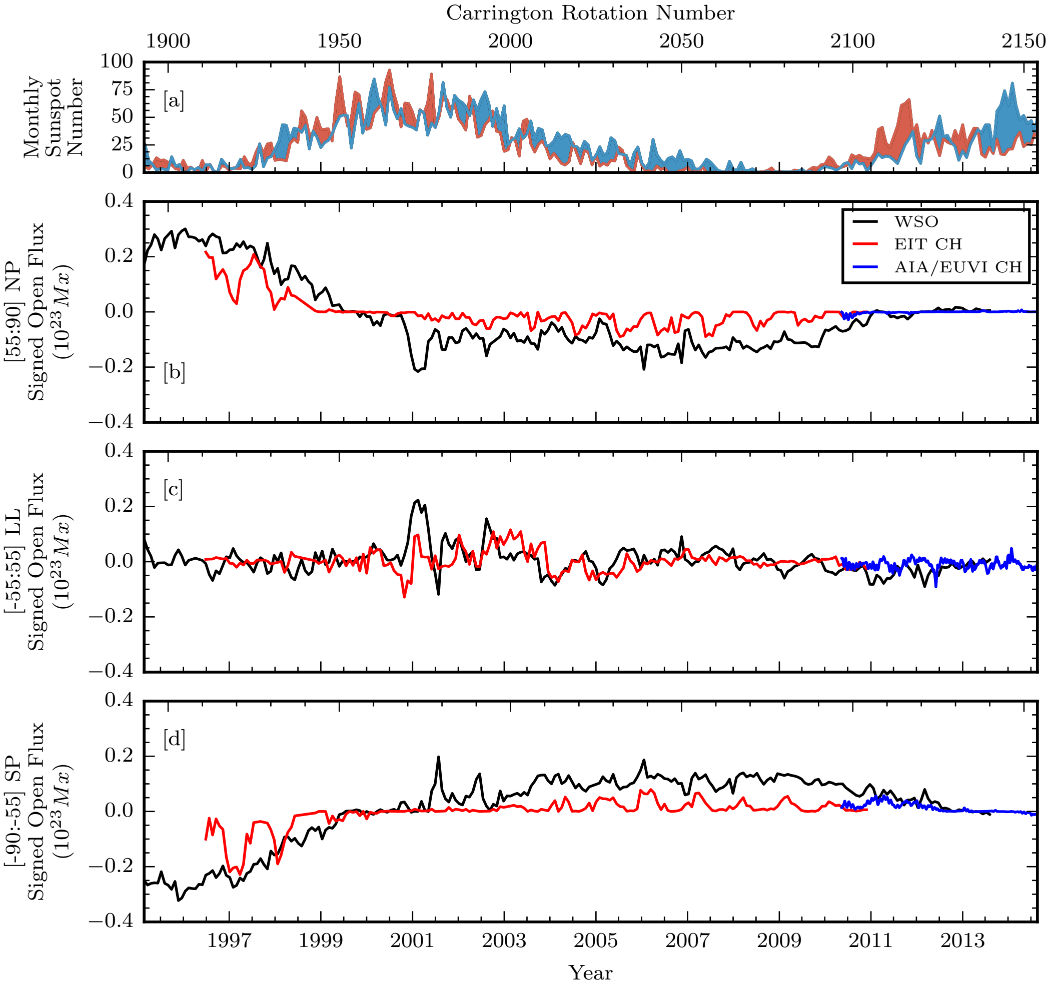

Figure 3.5. Comparisons of signed photospheric flux and associated quantities over the entire data span. [a] Hemispheric sunspot number for northern and southern hemispheres in red and blue, respectively. (WDC-SILSO, Royal Observatory of Belgium, Brussels) [b-d] Signed open magnetic flux, for a few sources, for the northern polar, low-latitudinal, and southern polar regions. WSO data in black is computed from total open field boundaries. EIT and AIA/EUVI coronal hole boundaries are used to compute the total enclosed magnetic flux in red and blue, respectively.

23 kicks off, each polar region is strongly dominated. The northern pole shows a strong dominance of positive magnetic polarity, while the southern pole shows a strong negative dominance. Both our EIT coronal hole and WSO computed open field measurements agree. As solar maximum for cycle 23 is reached, this polarity dominance drops off, and each pole becomes neutral around 2000. Throughout this next bout of minimal activity between cycles 23 and 24, a different story emerges. Here, the WSO computed open field shows a much weaker polarity dominance, this time of the opposite sign as expected. Our EIT measurements of coronal hole open flux show an even weaker polarity dominance. This stands in stark contrast with the heavy polarity dominance of the previous minimum. As cycle 24 reaches something resembling a peak around 2014, once again both poles have reverted to a neutral state. Here our AIA/EUVI observations fall more in line with the computed WSO open field measurements.

A Close Look at Cycle 24

To better illustrate details for solar cycle 24, we consider data only from 2010 May 13 - 2014 August 19, Carrington rotations 2096-2154. Here, many of the same trends and conclusions are evident, with some new details visible with scaling. Figures 3.6, 3.7, 3.8, and 3.9 display identical values to the larger dataset just discussed, but with a retracted viewpoint to only cover the range of data available from AIA/EUVI. Figure 3.6 gives maps showing latitude distribution of the coronal hole, mean magnetic field and total unsigned flux in the holes. Figures 3.7, 3.8, and 3.9 represent the measured coronal hole area, unsigned open magnetic flux, and signed open magnetic flux, respectively. These plots are identical in labeling to those spanning the entire dataset, with the addition of AIA/EUVI raw data displayed in the lighter shade of blue, compared with a 27-day running average in darker blue.

Figure 3.6-(b-d) displays the SDO-era data available using our coronal hole detection routine. While our SOHO-era coronal hole data was gathered at 24-hour cadence, the results were stacked and binned over a full solar rotation. This methodology allows for the calculation of an upper-bound of coronal hole area and enclosed unsigned magnetic flux, capturing the location of each earth-facing coronal hole location throughout that rotation. Our SDO-era methodology is slightly different, with the inclusion of *STEREO*/EUVI data. With the inclusion of EUVI data, far-side (opposite Earth) coronal hole observations are possible. This allows for our coronal hole mappings to be presented at full 12-hour cadence, without binning. This is immediately apparent with the coronal hole area latitude profiles in Figure 3.6-(b). In 2010 May, the beginning of our dataset, a regular gap in the data appears, coinciding with the solar rotation rate. At the beginning of our SDO-era data, 2010 May 13, the STEREO spacecraft had achieved an orbital separation of roughly 70-degrees ahead and behind, each with respect to Earth. This left roughly a 40-degree range of longitudes that were unobservable in EUV. As the STEREO spacecraft continued in

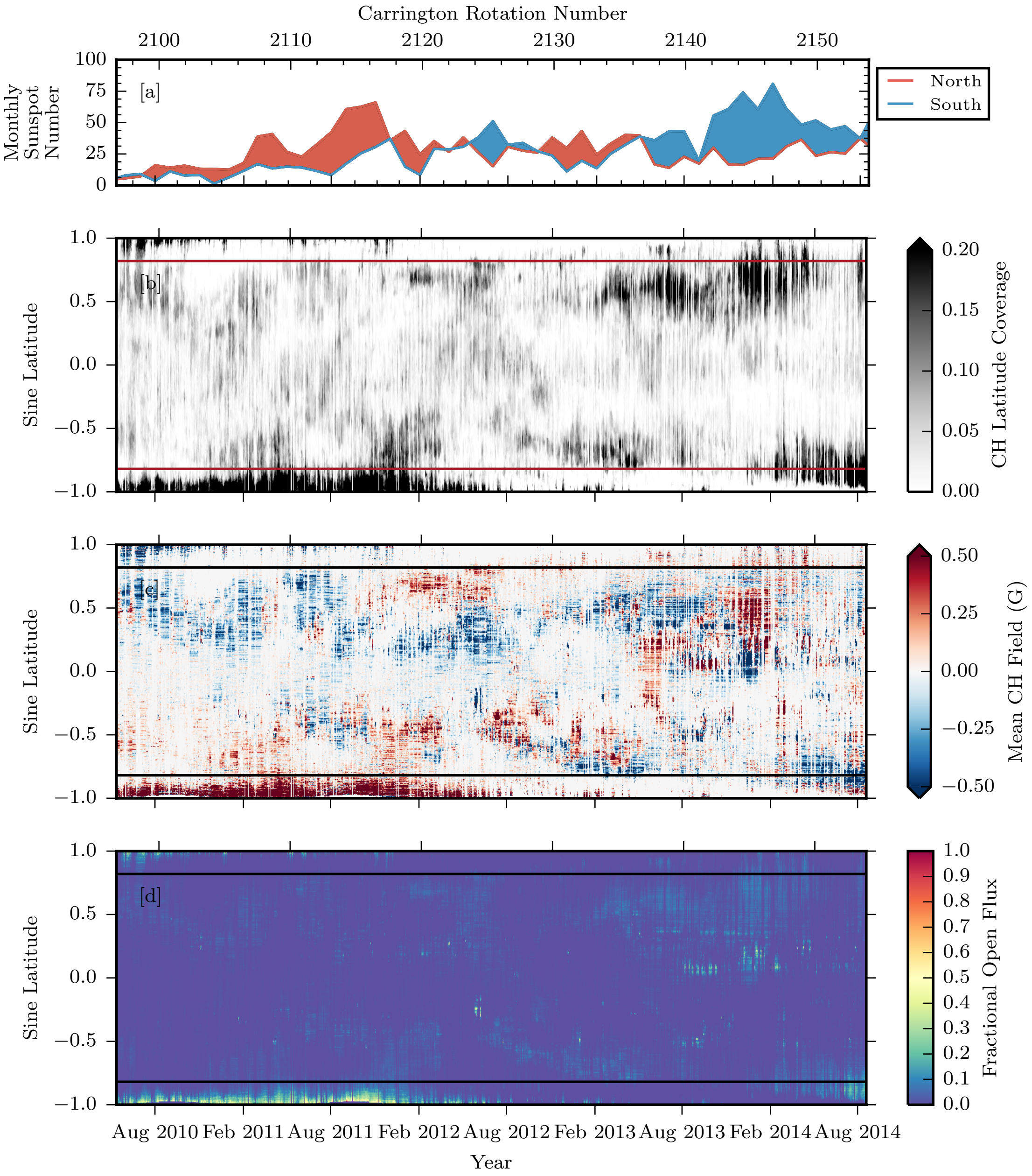

Figure 3.6. For the time period 2010 May 13 - 2014 August 19: [a] Monthly hemispheric sunspot number for the northern (red) and southern (blue) hemispheres (WDC-SILSO, Royal Observatory of Belgium, Brussels). [b] Coronal hole latitude profile of coverage, integrated over longitude. Horizontal red lines are marked at ±55 degrees latitude, to distinguish polar and low-latitude zones. [c] Latitude profile of coronal hole dominant polarity, integrated over longitudes. [d] Latitude profile of coronal hole enclosed magnetic flux, integrated over longitudes.

their orbital separation, this gap continued to shrink. With near-limb data truncated from each data source, higher frequency gaps appear further in the dataset as large holes rotate through these small blind-spots.

SDO-era latitude profiles of coronal hole area and signed/unsigned flux displayed in Figure 3.6 reveal a few items are of note. From 2010 May until 2014 January, the latitude demarcation of ±55 degrees continues to divide our polar and low-latitude coronal holes. From 2014 January until 2014 August, two large coronal holes develop on the upper edge of our low-latitude region, then drifting and extending beyond ±55 degrees, with the northern polar extension of this hole developing much weaker and diminishing earlier than that found in the southern pole. Referring back to Figure 3.2-(b), this same pattern of expansion into the pole is apparent with EIT data from 2001 until 2003. Here, however, this expansion occurs with much greater symmetry and nearly in phase; both the northern and southern extensions into the polar regions evolve and persist. The asymmetric coronal hole distribution within polar regions in cycle 24 is apparent in the total coronal hole area displayed in Figure 3.7.

The mean coronal hole field in Figure 3.6 shows the dominant polarity of each of our major coronal hole distributions. From 2010 May until 2012 August the northern polar coronal hole distribution is dominated by negative magnetic flux, with the southern polar coronal holes dominated by positive flux. Note that the northern polar coronal hole distribution has fallen off in area and resulting signed/unsigned flux as of 2011 February, with lingering traces thereafter until completely vanishing in 2012 February. Once again, this particular lead-in to a polar polarity inversion behaves in a much more asymmetric manner than the reversal observed with SOHO-era data in mid-1999. The total signed flux is plotted in Figure 3.9. Note that in these plots, the PFSS model computed signed flux is somewhat larger than observed in both the polar regions as well as at the low-latitudes before 2012. We suspect that these modeled measurements, based on spherical-harmonic generated radial magnetic field from WSO, lack the weaker and smaller scale magnetic flux elements present in observed coronal holes.

The unsigned open flux latitude distribution in Figure 3.6-(d) results from previous noted trends in the coronal hole area latitude profile. Here we see that the southern polar coronal hole distribution dominates the density of unsigned open magnetic flux, with smaller distributions at the northern pole and lower latitudes. The measured total flux is plotted in Figure 3.8. As described in the earlier text, as a whole the AIA/EUVI measured total flux is much closer to the model computed total flux, but there are variations in the latitude dependent comparison. The AIA/EUVI measured flux is comparable or higher than the model computed flux within polar regions. However, at lower latitudes the computed flux overshoots the measured flux.

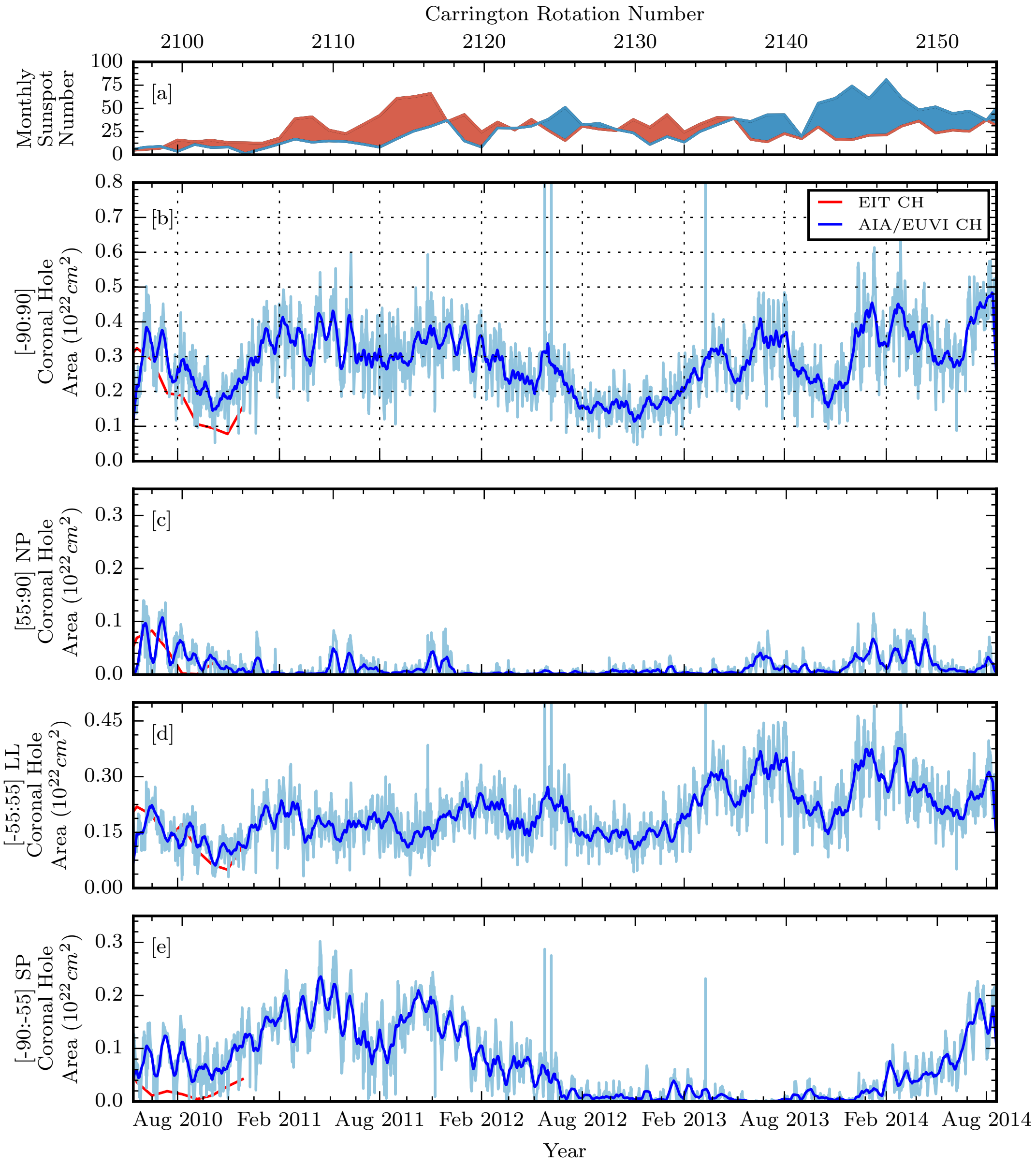

Figure 3.7. Comparisons of coronal hole area and associated quantities over the SDO-era data span. [a] Hemispheric sunspot number for northern and southern hemispheres in red and blue, respectively. (WDC-SILSO, Royal Observatory of Belgium, Brussels) [b] Total coronal hole area, for a few sources. EIT and AIA/EUVI coronal hole boundaries are used to compute the coronal hole area in red and blue, respectively. AIA/EUVI raw data is displayed in light-blue, with a 27-day running average displayed in dark-blue. [c-e] Coronal hole area computed for northern polar, low latitudinal, and southern polar regions.

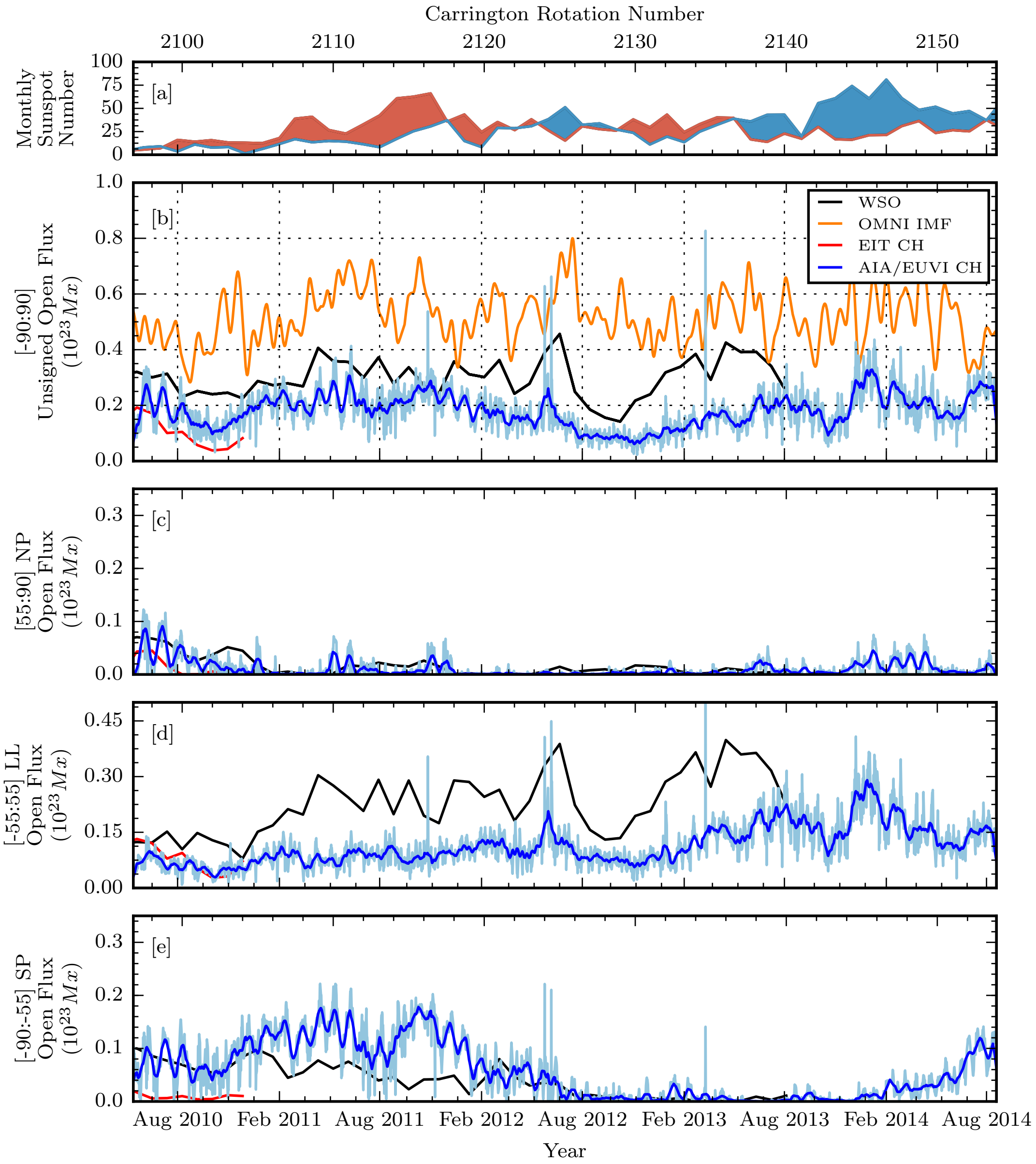

Figure 3.8. Unsigned photospheric flux and associated quantities over the SDO-era data span. [a] Hemispheric sunspot number for northern and southern hemispheres in red and blue, respectively. (WDC-SILSO, Royal Observatory of Belgium, Brussels) [b] Total unsigned open magnetic flux. WSO computed open flux is displayed in black. EIT and AIA/EUVI coronal hole boundaries are used to compute the total enclosed magnetic flux in red and blue, respectively. AIA/EUVI raw data is displayed in light-blue, with a 27-day average displayed in dark-blue. OMNI $|B_r(r = 1AU)|$ is used to compute an equivalent open magnetic flux (orange). [c-e] Open magnetic flux computed for northern polar, low latitudinal, and southern polar regions.

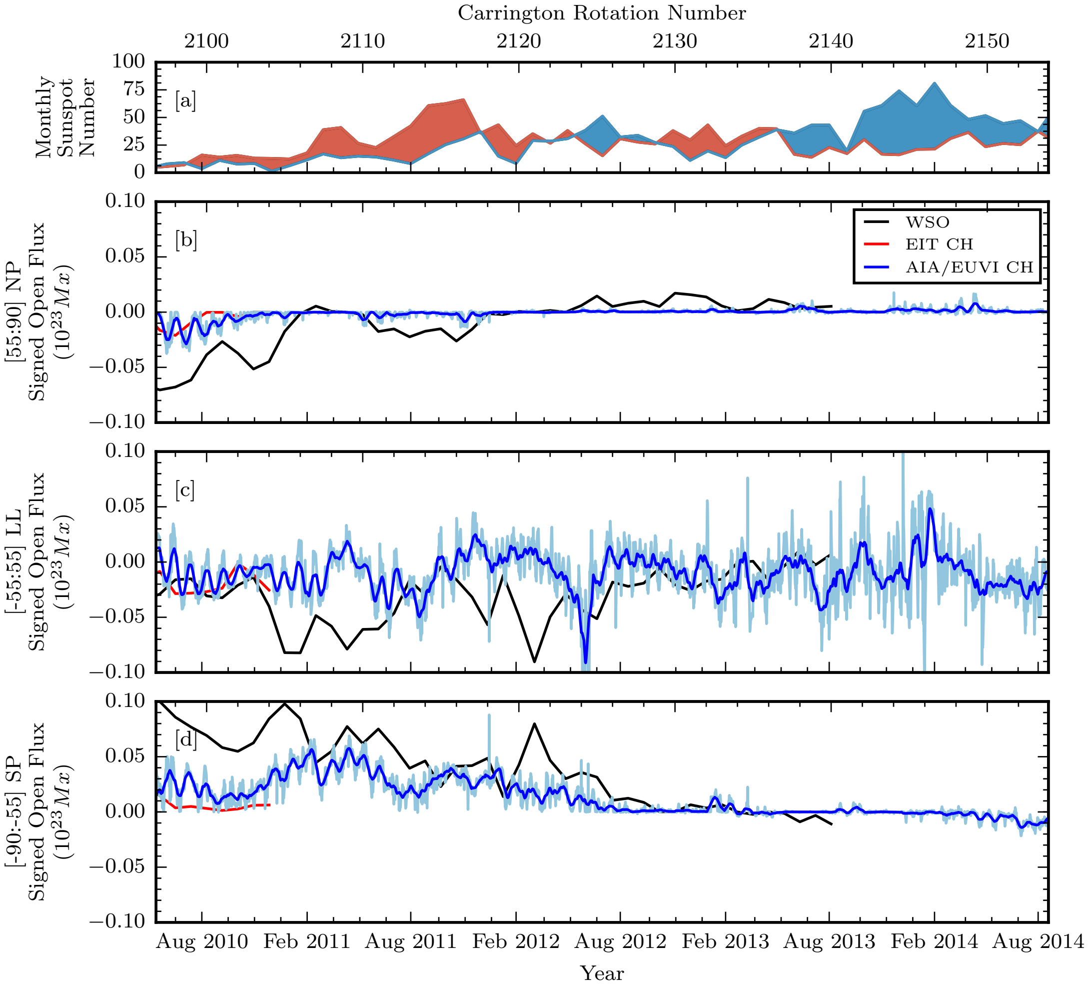

Figure 3.9. Comparisons of signed photospheric flux and associated quantities over the SDO-era data span. [a] Hemispheric sunspot number for northern and southern hemispheres in red and blue, respectively. (WDC-SILSO, Royal Observatory of Belgium, Brussels) [b-d] Signed open magnetic flux, for a few sources, for the northern polar, low-latitudinal, and southern polar regions. WSO data in black is computed from total open field boundaries. EIT and AIA/EUVI coronal hole boundaries are used to compute the total enclosed magnetic flux in red and blue, respectively. AIA/EUVI raw data is displayed in light-blue, with a 27-day running average displayed in dark-blue.

Conclusions and Discussions

Through the use of SOHO/EIT, SDO/AIA, and STEREO/EUVI A&B EUV data from 1996 until 2014 August, coronal hole boundaries have been tracked over the entirety of solar cycle 23, and a good portion of cycle 24. This extensive range allows for detailed analysis of coronal hole evolution in all latitudes, and comparison of the magnetic open flux, which is directly measured from the coronal holes, from the past cycle to the current cycle. The addition of STEREO/EUVI data allows for improved polar coverage in the current cycle, and also provides a reference to assess the polar hole and open flux measurements by EIT in the past cycle. A few trends in this data are apparent.

These data show that, coronal holes, and the signed and unsigned magnetic flux measured inside the holes, exhibit distinct evolution patterns across the latitude ±55 degree. This special latitude distinguishing polar regions from the low-latitude active bands was reported by McIntosh et al. (2014, 2015), showing the distinct progression of the magnetic range of influence (MRoI) below and above this latitude.They found this same latitude also marks the boundary of EUV bright point distribution, as well as the coronal green line (Fe XIV 5303Å) emission. Coronal holes map the foot-prints of solar open magnetic field, whose latitude profile is evidently modulated by the same intrinsic mechanism governing a variety of magnetic and radiative features.

Also observed is an asymmetry in the evolution of coronal holes in the northern and southern polar regions ($|\lambda| > 55°$), consistent with observations by McIntosh et al. (2014). This asymmetry manifests in both the rising of polar coronal hole coverage during solar cycle 23, and more distinctively in the decline and rise of polar coronal holes in solar cycle 24. By tracking the evolution of coronal holes across all latitudes, we see the appearance of large dominant-polarity coronal hole structures at lower-latitudes, migrating towards the polar regions. While these low-latitude signatures appear at roughly identical times, their push into the polar regions occurs at differing speeds, resulting in the northern polar coronal hole establishing itself much earlier.

When the two cycles are compared, the current cycle has much smaller coronal hole coverage and total open flux, by nearly a factor of two, than the last cycle. Further, the dominant magnetic field in the holes is much weaker in the current cycle, resulting from both the weak photospheric field as well as increased degree of polarity mixture in the holes in solar cycle 24. Most significantly, in cycle 24, the polar flux reversal exhibits a stark asymmetry compared with the last cycle. The northern polar holes have dropped off from 2009, two years ahead of the southern polar holes, and the open flux there has remained at a very low level since then, whereas the southern polar holes have recovered from the drop-off in 2013 with the open flux rising again in 2014.

Finally, the observed coronal holes, directly measured open flux in these holes, and their latitude dependence have been compared with the calculation by the PFSS model using the synoptic WSO data. It is shown that, on the one hand, this model has reasonably reproduced polar coronal holes and open flux in much agreement with observations in both cycles. On the other hand, as confirming the results in our earlier study (Chapter 2: Lowder et al., 2014), there is a clear discrepancy at low latitudes, which contributes significantly to the total open flux particularly during the solar maximum. The potential model appears to produce more open flux than observed at the low latitudes in both cycles, even though these regions are presumably better captured by the AIA/EUVI instruments in the current cycle. Therefore, such comparison indicates the importance of the latitude-dependent evolution of coronal hole boundaries, which provide an observational constraint to help advance models of the Sun's global magnetic field.

A FLUX TRANSPORT MODEL FOR COMPUTATION OF OPEN MAGNETIC FIELD

Contribution of Authors and Co–Authors

Manuscript in Chapter 4

Author: Chris Lowder

Contributions: Conceived and implemented study design. Constructed code to analyze data sets. Wrote first draft of the manuscript.

Co–Author: Dr. Jiong Qiu

Contributions: Helped to conceive study. Provided feedback of analysis and comments on drafts of the manuscript.

Co–Author: Dr. Robert Leamon

Contributions: Helped to conceive study. Provided feedback of analysis and comments on drafts of the manuscript.

Co–Author: Dr. Dana Longcope

Contributions: Helped to conceive study. Designed and supervised use of tool to gather active region data. Constructed flux transport model code. Provided feedback of analysis and comments on drafts of the manuscript.

Manuscript Information Page

Chris Lowder, Jiong Qiu, Robert Leamon, Dana Longcope
The Astrophysical Journal
Status of Manuscript:
_x_ Prepared for submission to a peer–reviewed journal
____ Officially submitted to a peer–reviewed journal
____ Accepted by a peer–reviewed journal
____ Published in a peer–reviewed journal

Introduction

As with any numerical modeling effort, observations provide a critical tool for confirmation. In particular, models of the evolution of photospheric and coronal magnetic field are often driven with Earth-side observations. This lack of incorporation of far-side data can leave a blind-spot in modeling efforts. Through the incorporation of far-side *STEREO* EUV data, coronal hole observations can provide a unique tool for validating the far-side evolution of coronal field models (Chapter 2: Lowder et al., 2014).

Potential magnetic field models provide one avenue of generating coronal magnetic fields for the calculation of open magnetic flux. These models compute a potential magnetic field from boundary conditions, solving for a magnetic field configuration that remains current-free. One model in particular, the potential field source surface (PFSS) model uses photospheric magnetic field data as an inner boundary condition, with the coronal field defined to be purely radial at a particular source surface height, often 2.5 $R_\odot$ (Schatten et al., 1969; Hoeksema et al., 1983; Wang & Sheeley, 1992). While these models lack a coronal current, which certainly is not the physical case, they do provide a fairly accurate map of the coronal field distribution and connectivity on a static case. Series of PFSS computations can be used to map the evolving coronal field connectivity through a series of potential field configurations.

With the addition of electric current in the modeled corona, non-potential models solve for a coronal field with conditions closer to reality. Often, however, PFSS models are able to solve for the global field configuration with reasonable accuracy, particularly with regard to open magnetic field (Chapter 2: Lowder et al., 2014). A number of non-potential models exist, including computation of open magnetic flux (van Ballegooijen et al., 2000; Yeates et al., 2010).

With regard to our prior work on the observation of coronal hole boundaries and comparison to computed open magnetic flux, a few points are of note. Our dataset of coronal hole locations spanning from 1996 to 2014 provides a useful tool for comparison with modeling efforts coinciding with this time period. As this dataset also spans almost all of solar activity cycle 23 and a decent portion of cycle 24, opportunities for comparison with modeling of an entire cycle are of importance. Through this prior study, comparison with the traditional PFSS model resulted in the conclusion that computed polar open magnetic field was accurate, despite the simplifications of the PFSS model. The discrepancy begins to unravel, however, in the low-latitude regions. Without accurate measure of low-latitude open magnetic flux, comparisons between modeling and observational efforts are lacking a piece of this puzzle. These concentrations of low-latitude open magnetic flux contribute significantly to the total heliospheric open magnetic flux, especially during periods of solar maximum.

The PFSS model employed here to generate coronal magnetic field has two major assumptions. The first is the lack of electric current in the corona. Prior work has hinted that this may not pose as large of a problem when considering the global field configuration. The second assumption is the static nature of the calculation. In our comparison with Wilson Solar Observatory (WSO) synoptic maps of radial magnetic field, we are able to generate one potential magnetic field configuration for the corona per solar rotation. Additionally, these observations are made from the Earth-side, ignoring field evolution on the far-side. To check where and how this model breaks, we approach the problem by first modifying the static nature of the problem. By generating a flux transport model, coupled with a calculation of the resulting coronal potential field, we are able to advance the photospheric boundary condition of the model.

Here we suggest modification of the parameters within the induction equation, notably the diffusivity and meridional flow profile. Several studies of this parameter space have been conducted in the past, either by observationally pinning-down these values or through comparison of model results with observables (Leighton, 1964; Wang et al., 1989; Baumann et al., 2004; Hathaway & Rightmire, 2010; Upton & Hathaway, 2014). A further description of these studies is given in Section 2.

If we then hold measured open flux from coronal hole observations as ground truth for comparison, we employ a flux transport model as our modifiable parameter.

This flux transport model uses observable active region data as the driving source term, evolving this resulting field with a given diffusion and flow field. A potential coronal field is then computed from the resulting boundary photospheric field, with the open magnetic field computed from this field. Our diffusion and flow field are then modified to explore the model output with observationally-driven calculations. While prior studies have considered the role of open magnetic field as a comparative tool, none have considered full-surface coronal hole observations as a tool, or span the range of time we consider here.

In the following sections, the basic methodology of the flux transport model, as well as the diffusion and meridional flow profiles used by prior literature are displayed in Section 2. Following this, Section 3 presents the results from our flux transport model. Notably, model calculated outputs are compared with observations and observation-driven calculations. Here we discuss the global solar dipole moment, the magnetic field surface distribution via a series of butterfly diagrams, and a latitude dependent calculation of open magnetic flux. Conclusions and discussions are exhibited in Section 4.

Methodology

The flux transport model developed here solves the induction equation to calculate a time-dependent magnetic field on the photosphere. Here we can employ a synoptic photospheric magnetogram as an initial boundary condition before allowing the field to evolve. This magnetogram is decomposed into a series of spherical harmonic coefficients for calculation, and then recomposed to provide a physical map for analysis. While the resulting evolved vector magnetic field has all three components, B_r, B_θ, and B_ϕ, for the boundary condition we employ only the radial field B_r reconstructed from the synoptic observational magnetogram. This input field is subsequently evolved forward in time using the induction equation,

$$\frac{\partial B_r}{\partial t} = D\nabla^2 B_r - \nabla \cdot (\mathbf{u}B_r) + S(t), \tag{4.1}$$

where D defines the diffusion coefficient, $\mathbf{u}$ defines the photospheric surface flows, including differential rotation and meridional flow. $S(t)$ represents the source term of new magnetic flux. A database is compiled of new magnetic field emergence, which this term references and inputs into the model as appropriate. Using results from an interactive tool developed to pinpoint and characterize active region emergence with *SOHO*/MDI data, our flux transport model can be run over the period 1996 November 13 to 2011 April 11.

To greatly reduce the computational time involved in evolving this equation forward, the problem can be approached from Fourier space. With the latitude coordinate λ spanning $-\pi/2$ to $\pi/2$, a coordinate μ can be defined as $\mu = \sin\lambda$. By decomposing the input field into Fourier-like coefficients,

$$B_r(\mu,\phi) = \Re\left[\sum_m \hat{B}_r(\mu,m)e^{im\phi}\right]. \tag{4.2}$$

These Fourier components can then be evolved forward using Equation 4.1. A resulting physical photospheric field map can then be reconstructed from the Fourier components.

Evolution of the photospheric magnetic field depends on plasma motions on multiple scales. The random walk of magnetic flux from supergranular convection patterns results in a diffusivity effect on the field, characterized by the diffusion coefficient D in the induction equation. Leighton (1964) first attempted to determine this diffusivity from observations, resulting in a value much too high in comparison with modern estimates. More recent measurements by Wang et al. (1989) narrowed down the observed values of D to 600±200 km^2 s^{-1}, studying the decay rate of active regions in addition to modeled polar field strengths. Following this result, our standard reference case was chosen with a constant of $D = 600$ km^2 s^{-1}. Additional diffusivity values were chosen above and below this value at 450 and 900 km^2 s^{-1}.

The differential rotation velocity profile as a function of the co-latitude θ was derived observationally from Snodgrass (1983),

$$\Omega(\theta) = 0.18 - 2.3\cos^2\theta - 1.62\cos^4\theta \text{ deg day}^{-1}, \tag{4.3}$$

resulting in a differential rotational flow at the photospheric boundary,

$$u_\phi(\theta) = \Omega(\theta) R_\odot \sin\theta. \tag{4.4}$$

A meridional circulation flow works to migrate magnetic flux elements from lower-latitude regions towards the poles. The amplitude of the flow is of much lower order of magnitude when compared with other processes, and can be difficult to observe and constrain. For this model a meridional flow profile was selected, following the profile of Wang et al. (2009),

$$u_\theta(\theta) = 2u_0 \cos\left[\frac{\pi(\theta_{max} + \theta_{min} - 2\theta)}{2(\theta_{max} - \theta_{min})}\right] \cos\theta. \tag{4.5}$$

For this simulation, the flow boundaries are set at $\theta_{min} = 0$ and $\theta_{max} = \pi$. By inserting these limits on the flow, and transforming into the latitude coordinate $\lambda = \pi/2 - \theta$ we arrive at

$$u_\theta(\lambda) = 2u_0 \cos\left(\frac{\pi}{2} - \lambda\right) \cos\lambda = u_0 \sin(2\lambda). \tag{4.6}$$

For comparison our meridional flow profile is plotted in Figure 4.1.

To explore the parameter space of our model, a range of values of diffusivity and meridional flow amplitude were selected. An exploration of prior work has guided our selection of parameters, displayed in Table 4.1. The range of values considered and the functional form taken by corresponding models are displayed where available in comparable form. Many prior studies employed constant parameters of diffusivity

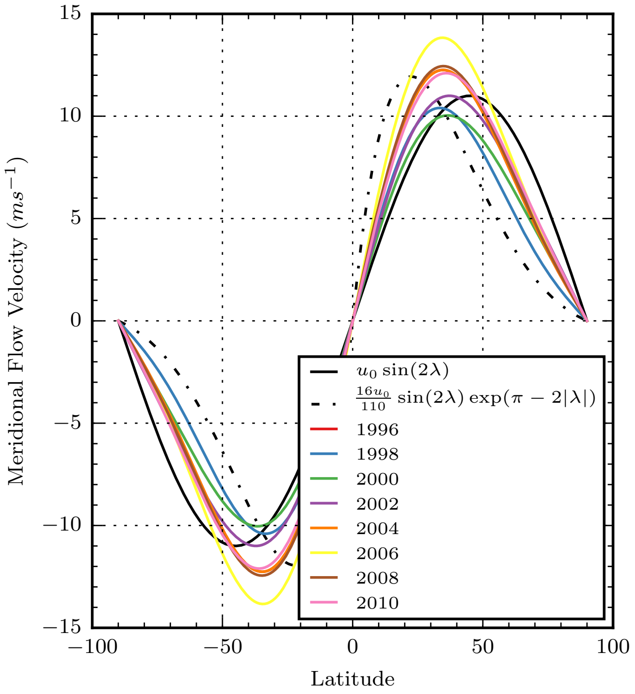

Figure 4.1. Comparison of meridional flow functional profiles for a product of two cosines (solid) and a product of a cosine and decaying exponential (dashed). Both profiles decay to zero at the poles and cross zero at the equator, but peak in differing locations. Additional curves display calculated time-dependent meridional flow profiles measured and employed by Upton & Hathaway (2014).

$D = 600$ km^2 s^{-1} and a sine-functional meridional flow with a peak of $u_0 = 11$ m s^{-1} and flow latitude boundary below 90°. Yeates (2013) employed a $\sin - \exp$ profile to more quickly diminish the flow toward the pole. These prior studies, in particular the parameter study by Baumann et al. (2004), show that the meridional flow profile plays the primary role in the generation and population of polar magnetic field. Given the slow time-scale of the meridional flow, this process can take an entire cycle to properly form a background field. One particular problem involves the over-abundance of modeled polar flux during solar activity cycle 23 (Wang et al., 2009; Jiang et al., 2011). In addition, Yeates (2013) and Baumann et al. (2004) have considered the modification of the diffusivity and meridional flow within flux transport models, and the resulting modifications to global solar magnetic field properties. More recently Hathaway & Rightmire (2010); Upton & Hathaway (2014), through photospheric magnetic element tracking, have measured cycle-dependent changes in the meridional flow profile and the result on polar field. A sample of these time-dependent flow profiles are displayed in Figure 4.1. For comparison the $\sin(2\lambda)$ form of the flow profile employed here, as well as the $\sin(2\lambda)\exp(\pi - 2|\lambda|)$ used by Yeates (2013), are displayed. The $\sin(2\lambda)$ form of the meridional flow peaks at higher latitudes than those observed, while the $\sin(2\lambda)\exp(\pi - 2|\lambda|)$ profile peaks at lower latitudes. Both profiles peak at values consistent with observations, with slight deviations at lower and higher latitudes. The $\sin(2\lambda)$ profile falls more in line with observations of the flow at lower latitudes, while overshooting towards the polar regions.

In this study, we start with a time-independent meridional flow profile in the form of Equation 4.5. This profile has the advantage of being adjustable in polar extension, transforming into the $\cos - \cos$ and equivalent $\sin(2\lambda)$ form with full extension to the poles in Equation 4.6. The magnitude of this flow will be varied, with meridional flow peaks (u_0) of 2.5, 5.0, and 11.0 m s^{-1}. Diffusivities (D) of 450, 600,

Table 4.1. Flux transport model parameters from prior studies.

	Diffusivity		Meridional flow	
Study	D ($km^2 s^{-1}$)	u_0 (ms^{-1})	Form	$\lambda_0(^\circ)$
Mackay et al. (2002b)	600	11	$u_0 \sin(\pi\lambda/\lambda_0)$	75
Baumann et al. (2004)	600	11	$u_0 \sin(\pi\lambda/\lambda_0)$	75
	50-1500	-	0-30	-
Wang et al. (2009)	-	14.5, 17	$u_0 \sin^{0.1}(\lambda) \cos^{1.8}(\lambda)$	-
Jiang et al. (2011)	250	11	$u_0 \sin(\pi\lambda/\lambda_0)$	75
Yeates (2013)	450	11, 35	$\frac{16u_0}{110} \sin(2\lambda)\cdot$	
			$\cdot \exp(\pi - 2\|\lambda\|)$	90
Upton & Hathaway (2014)	-	-	N/A	-

and 900 km^2 s^{-1} will be employed. In comparison with prior studies of this parameter space, this selection maps out well. This flux transport model is then run with these sets of parameters, with the model computed dipole moment and open magnetic flux compared with observations. In contrast with prior studies, we compare both the calculated and observed latitude-dependence of the open magnetic flux. Results are outlined in the following section, with a summary of model and observation comparison in Table 4.2.

Results

Magnetic Butterfly Diagram

For each time-step in our flux transport model simulation, the photospheric magnetic flux density is calculated, extracted, and integrated along longitude to yield a

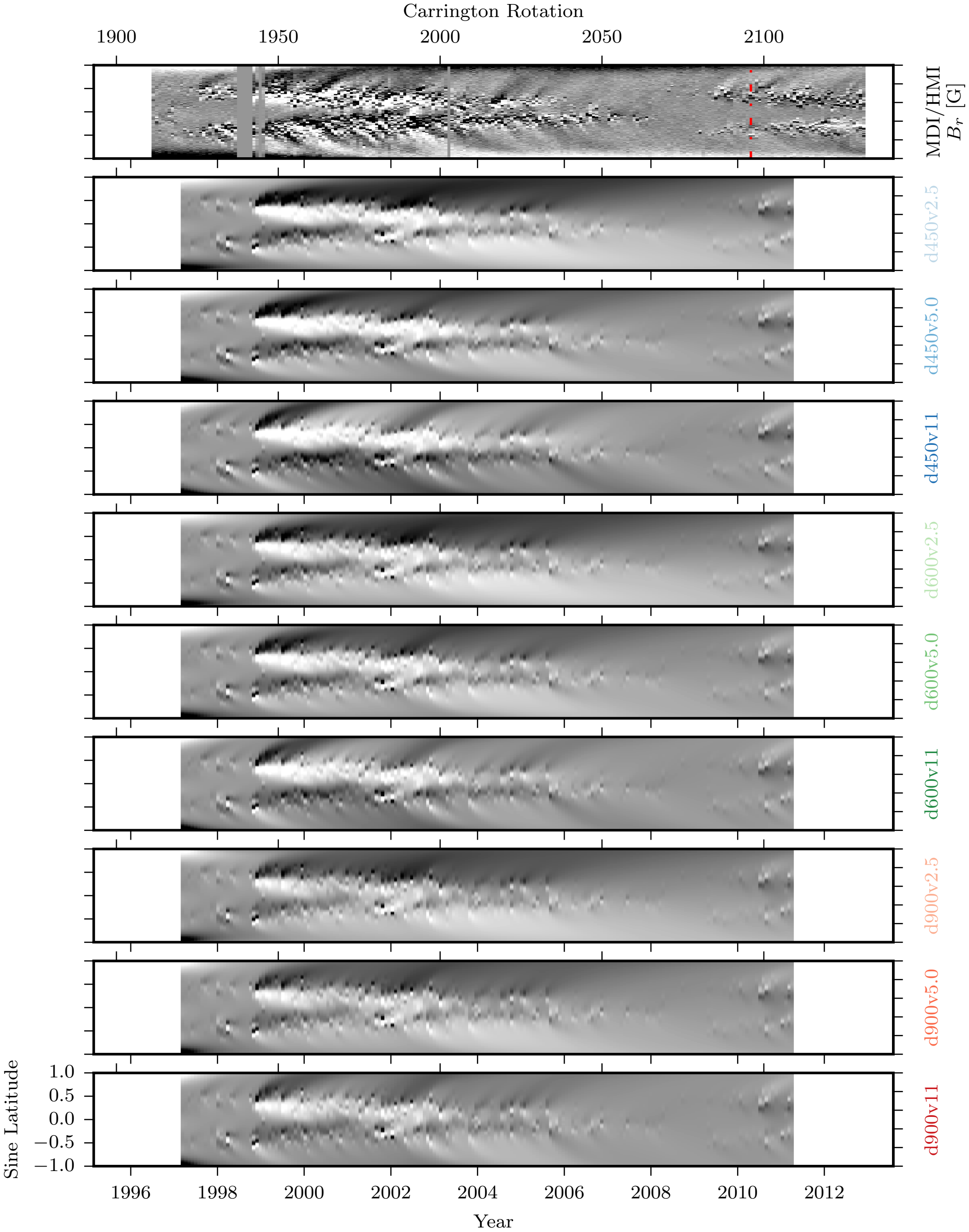

Figure 4.2. Observational and synthetic butterfly diagrams from model data, with magnetic field clipped at ± 5 G. A few example cases of various parameter values are shown. For the case of HMI/MDI observational data, the vertical red dashed line indicates the transition from MDI to HMI data.

slice of latitudinal magnetic field dependence. Here we capture for each latitude bin the average magnitude and polarity of the magnetic flux density from our model. These slices can then be stacked for each subsequent time-frame throughout the simulation, resulting in a map of signed magnetic flux density for each bin of time and sine-latitude. Figure 4.2 shows the results from this calculation. For an observational reference, the upper subpanel shows the MDI/HMI measurements of magnetic flux density, with a red dot-dashed line indicating the transition point from MDI to HMI observables. One synoptic chart of radial magnetic flux density is calculated for each rotation from each instrument. In the same manner as the simulations, we take this map and create a latitude profile of average magnetic flux density. These are then stacked in an identical fashion to track this latitude profile over time.

Considering this observational reference, we see the traditional butterfly diagram pattern as magnetically active regions appearing at higher latitudes and then migrating towards the equator. During this period, the polar regions have an established dominant polarity. During cycle 23, the northern and southern polar regions have a negative and positive dominating polarity, respectively. As the magnetic activity cycle reaches a minimum, active latitudes have migrated down to the equator, with a subsequent disappearance of active latitudes. As cycle 24 begins to rise, active regions appear at higher latitudes, and begin to migrate towards the equator once again. McIntosh et al. (2014) have noted the appearance of these ‘chevron’ patterns, and have used their timing and asymmetry to track and predict the upcoming solar activity cycle progress.

The remaining sub-panels of Figure 4.2 plot the magnetic flux density butterfly diagrams for the flux transport model runs. For ease of comparison, all sub-panels display the longitudinally-averaged magnetic flux density with a color-scaling cutoff of $\pm 5\ G$. The span of the simulation is shorter than that of the joint MDI/HMI observations. The start of the simulation occurs after a sufficient active region emergence rate occurs to drive the simulation field, early in 1997. The end of the simulation coincides with the end of MDI observations, in early 2011.

One immediate observation is the effect of increasing meridional flow on this magnetic flux density distribution. For each set of diffusion values, increasing the meridional flow profile speed results in a faster migration of flux density to the polar regions. Increasing meridional flow also results in flux being pushed towards the poles before diffusion processes allow a dominant polarity flux to establish. This results in a more dominant polarity in the polar regions for a lower meridional flow profile.

In comparing the results of a higher diffusivity value, the effect can be mainly seen at the poles. For a lower diffusivity value, 450 $\mathrm{km}^2\ \mathrm{s}^{-1}$, the buildup of a dominant polar polarity is apparent, especially for lower meridional flow amplitude. With increasing diffusivity, this dominant polarity in the polar regions becomes less and less apparent, especially in comparison with observational signatures from MDI/HMI.

Solar Dipole Moment

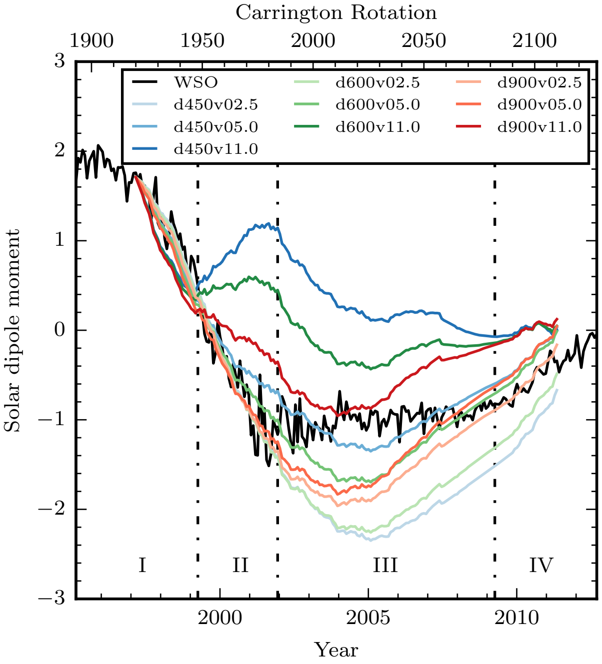

Figure 4.3. The modeled solar dipole moment plotted for comparison with a magnetogram-derived observational measure (solid black curve). Model derived results are displayed with diffusion values of 450, 600, and 900 km^2s^{-1} and combinations with meridional flow amplitudes, 5 and 11 ms^{-1}.

Figure 4.3 displays the solar dipole moment from our flux transport model. The observed dipole moment from WSO data is plotted in black, with our flux transport models in a color scheme. With increasing darkness representing an increase in meridional flow profile amplitude from 2.5, 5, to 11 m s^{-1}, diffusivity values of 450, 600, and 900 km^2 s^{-1} are plotted in blue, green, and red, respectively.

Our observational signature of the solar dipole moment begins in 1995, with our flux transport model picking up in late 1996. During this period of minimum solar activity, the solar dipole moment is peaking quite strongly. As the magnetic activity cycle evolves into a maximum phase around 2000, the solar dipole moment has effectively been killed off, dropping down near zero. During the ensuing declining phase of the solar cycle from 2000 until 2009, the solar dipole moment remains negative, with a much weaker magnitude than during the rising phase of cycle 23. Reaching the supposed peak of cycle 24, the solar dipole moment has risen back up towards zero.

Our flux transport model explores this portion of the observable parameter space in comparison with the dipole moment. For the sake of simplification, sets of diffusivities and meridional flow peak values are referred to via their reference code found in Table 4.2. As seen in the figure, there are several outliers here that do not match our observable dipole moment in any sense of the word, notably the parameter sets d450v11.0, d600v11.0, d450v02.5, and d600v02.5.

The remaining model dipole moments have varying degrees of success. During the rising phase of cycle 23, as the solar dipole moment drops off, a higher meridional flow profile amplitude results in a sharper drop in dipole moment than is observed. With lower flow profiles, the model dipole moment drop lies more in line with observations. The next key differentiating moment is at the start of the declining phase of cycle

23. Here, the dipole moment has reached a maximum amplitude, and begins to return towards zero. For the parameter sets d900v11.0, d450v05.0, and d600v05.0 this return towards zero begins in a reasonably correct time, with preference for the latter two cases. For the remaining cases, the dipole moment continues to evolve in the negative direction, extending far too powerfully in that direction. The eventual return towards zero occurs far too late. For the two outlying cases of very low meridional flow profile, this amplitude results in a lag effect before changes in flux emergence at lower latitudes propagate towards the poles. For the outlying cases of very high meridional flow profile amplitude, these changes at low latitude are propagated far too quickly towards the polar regions. Increasing diffusivity value brings these curves closer in line, as the flux is given a stronger motivation to cancel. Otherwise, the flow profile pushes this emerging flux to the poles before being given a chance to diffuse away significantly. These factors work in conjunction to effectively neutralize the dipole moment, by not allowing for significant diffusion of flux to establish a dominant polarity before being pushed into the polar regions.

To summarize these comparisons, the time-averaged relative difference between the observed and model calculated dipole moment is calculated and listed in Table 4.2. It is shown that, the peak flow speed at 5 m s^{-1} with the given flow profile produces the dipole moment best matching the observed.

Open Magnetic Flux

To continue our analysis of this flux transport model, the unsigned open magnetic flux is another useful tool of consideration and comparison. To explore the range of model calculated open magnetic flux, a potential field can be computed using the PFSS model and the evolved boundary photospheric radial magnetic field. Here, we compare this open flux with that calculated using the same PFSS model but with the synoptic WSO data, and also with the open flux directly measured in coronal holes (Chapter 2: Lowder et al., 2014). These results are displayed in Figure 4.4.

For the flux transport model, our open flux is calculated as follows. For each time step, the driven field is decomposed into a series of spherical harmonics. These harmonics then provide the boundary condition at $1R_\odot$ to construct a potential field between 1-2.5 $R_\odot$, with a purely radial field imposed at the outer boundary. With a potential field calculated at each time step, here once per Carrington rotation, open magnetic field is traced down from the outer to inner boundaries.

Note that while it would be far simpler to tally up the total open flux from the potential field at 2.5 $R_\odot$, all information regarding the mapping of this open field structure would be lost. For the purposes of breaking open flux down into polar and low-latitudinal contributions, this mapping must be preserved.

For each of our parameter set simulation runs, the open flux was computed as a mapping of open field structure at 1 $R_\odot$, from which the standard polar boundaries

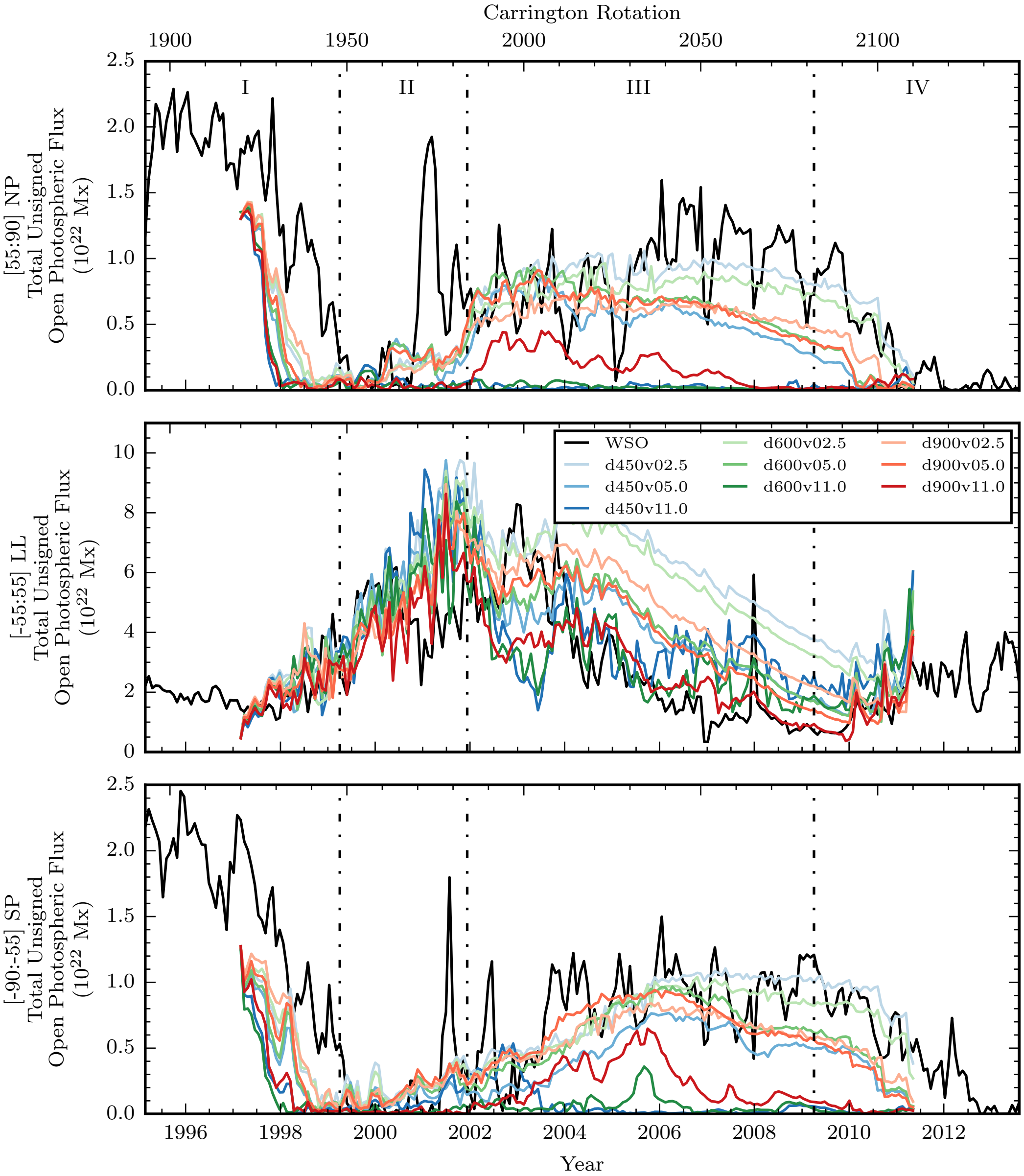

Figure 4.4. Total photospheric unsigned open magnetic flux, calculated from the flux transport model. Comparison is made with calculated total unsigned photospheric flux from WSO data, input into our PFSS calculation. Several combinations of diffusion coefficient and meridional flow velocity.

were drawn at ±55 degrees. Flux was integrated over these distinct regions, at a cadence of one mapping per Carrington rotation.

The center subfigure of Figure 4.4 displays the low-latitude open flux for our set of parameter runs. Time-span ranges and color-coding are identical to prior figures in this series. Within our first time-span, $\mathcal{T}_I$, changes in our parameters make slight changes to the overall course of the low-latitude open magnetic flux. All of these parameter runs meander around the values calculated from our WSO values. During this time-period, the simulation is still allowing the effects of new flux emergence to propagate throughout the simulation domain via meridional flow. However, at low-latitudes, where the open flux is driven by new flux-emergence, this has much less of a prominent effect. $\mathcal{T}_{II}$ begins a more interesting timespan, where our simulation begins to diverge more rapidly and distinctly from our WSO values. By mid-2000 the low-latitude open flux continues to rise for all parameter sets, while a drop-off begins in WSO data. $\mathcal{T}_{III}$ begins a period of low-latitude open flux slowly declining. By $\mathcal{T}_{III}$, the simulation has had more than sufficient time for this initial 'breaking-in' period to have ended, resulting in the largest divergence from observation. Throughout this span, higher meridional flow magnitudes result in an overall lowering of low-latitude open magnetic flux. Newly emerging flux is quickly pushed out of the way towards the poles, not being given as much time to linger at lower latitudes. With lower meridional flow this low-latitude open flux rises to higher values, as this flux is allowed to hang around at low-latitudes. Overall, meridional flow profiles of 11 m s^{-1} best match the WSO data, with parameter set d900v11.0 matching best of all. Within $\mathcal{T}_{IV}$ low-latitude open flux begins to rise once again. Once again higher meridional flows result in lower open flux throughout this period, better matching WSO data. Again, the parameter set d900v11.0 best matches our WSO computed open flux.

The polar regions paint a much different picture for the role of our parameter space regarding open magnetic flux. Within the first time domain, $\mathcal{T}_I$, the polar regions exhibit a far more severe 'breaking-in' period. Here, the initializing dipole field defines our polar field, with new flux emergence slowly migrating upward and defining this region. As is expected, these initial polar open fluxes rapidly drop off, far faster than WSO data. Higher meridional flow during this period results in a faster drop-off in these polar fluxes. This is the result of new flux migrating into the polar regions before being given a chance to diffuse to establish a dominating polarity at lower latitudes. This diffusion then occurs in the polar regions, diminishing existing flux elements.

The next span, $\mathcal{T}_{II}$ has two distinct phases in the polar regions. After our observationally-driven open flux has dropped off to near-zero values, a sudden and large increase in polar open flux occurs. In the northern pole this jump carries onward, whereas in the southern pole this jump in polar open flux diminishes before rising again. For our flux transport model, for all combinations of diffusivity with meridional flow of 11 m s^{-1} the polar open magnetic flux hovers around zero. For other parameter sets with lower meridional flow magnitude, rises in both polar fluxes are generated, though not quite of the magnitude observed with WSO.

Throughout the next span, $\mathcal{T}_{III}$, polar flux slowly rises, maintaining a significant value. A decay in this polar flux begins towards the end of $\mathcal{T}_{III}$ in the northern pole, with a similar decay beginning in the southern pole during $\mathcal{T}_{IV}$. Throughout $\mathcal{T}_{III}$, the higher meridional flow value of 11 m s^{-1} once again results in a diminished polar open magnetic flux. The parameter set d900v11.0 makes a valiant effort at matching our polar fluxes, but is just unable to reproduce the overall 'Nessie' like hump in the polar open magnetic fluxes. The remaining parameter sets with lower meridional flow are able to better match the polar open flux within the first half of $\mathcal{T}_{III}$, but diverge in the latter half. In particular, the sets d450v02.5 and d600v02.5 excellently match the polar open magnetic flux throughout this span.

$\mathcal{T}_{IV}$ shows the decline of observed polar open magnetic flux. Note that this decay begins at least one year prior in the northern pole as compared with the southern pole. Once again the higher meridional flow profiles fail to capture sufficient build-up of polar open flux. The same parameter sets d450v02.5 and d600v02.5 best match in this span. The remaining parameter sets simply have too low of a polar open flux. Note that our WSO computed open flux decays to zero in the northern pole in early

Table 4.2. Flux transport model parameters

Reference	$D\ (km^2 s^{-1})$	$u_0\ (ms^{-1})$	Dipole	NP/SP Φ_O	LL Φ_O	Total Φ_O
d450v02.5	450	2.5	0.79	**0.42**	1.70	0.73
d450v05.0	450	5.0	**0.27**	0.56	**0.79**	**0.28**
d450v11.0	450	11.0	1.23	0.89	0.93	0.31
d600v02.5	600	2.5	0.67	**0.40**	1.47	0.60
d600v05.0	600	5.0	**0.30**	0.50	0.79	**0.31**
d600v11.0	600	11.0	0.87	0.89	**0.61**	0.35
d900v02.5	900	2.5	0.40	**0.46**	0.99	0.35
d900v05.0	900	5.0	**0.33**	0.50	0.66	**0.29**
d900v11.0	900	11.0	0.50	0.78	**0.38**	0.35

Note. — Matrix of mean relative error between modeled parameters and observable-derived values. The lowest relative errors are displayed in bold.

2012, with a similar bottoming out of open flux in the southern pole occurring in mid 2012.

To summarize these results, the time-averaged relative difference between the open flux calculated by the flux transport model and by the static PFSS model is calculated and displayed in Table 4.2. Comparison of the latitude-dependent open flux indicates that a low flow speed of 2.5 m s^{-1} generates polar open flux most comparable with the reconstruction by the PFSS model using synoptic WSO magnetograms, found to be in good agreement with directly measured polar open flux from coronal holes (Chapter 2: Lowder et al., 2014). On the other hand, a high flow of order

11 m s^{-1} is required in the flux transport model to produce the open flux in low-latitudes most comparable with the result by the static PFSS model. Lowder et al. (2014) have shown that PFSS model using WSO synoptic magnetograms tends to over-estimate the open flux at the low latitudes compared with direct measurements from coronal holes. The implication is, therefore, that a still higher flow would be needed in the flux transport model to further bring down the low-latitude open flux.

Time-Dependent Meridional Flow

To adapt this model to more realistically portray meridional flow profiles, a time-dependent profile is employed. Using the observed flow profiles from Upton & Hathaway (2014), two time-dependent model meridional flow profiles were computed. Figure 4.5 displays the constant meridional flow values of 2.5, 5.0, and 11.0 m s^{-1} (dotted), as well as the observationally-driven two profiles. The first profile (solid) is generated from the observed profile by calculating the peak meridional flow at each time-step of one Carrington rotation. The second profile (dashed) is calculated by computing the amplitude of the observed meridional flow profile at a latitude of 55-degrees. Both of these observed amplitudes are then used in conjunction with the model meridional flow profile (Equation 4.6). The model then continues driving the coronal magnetic field forward in time, updating the meridional flow profile as needed throughout the course of the simulation.

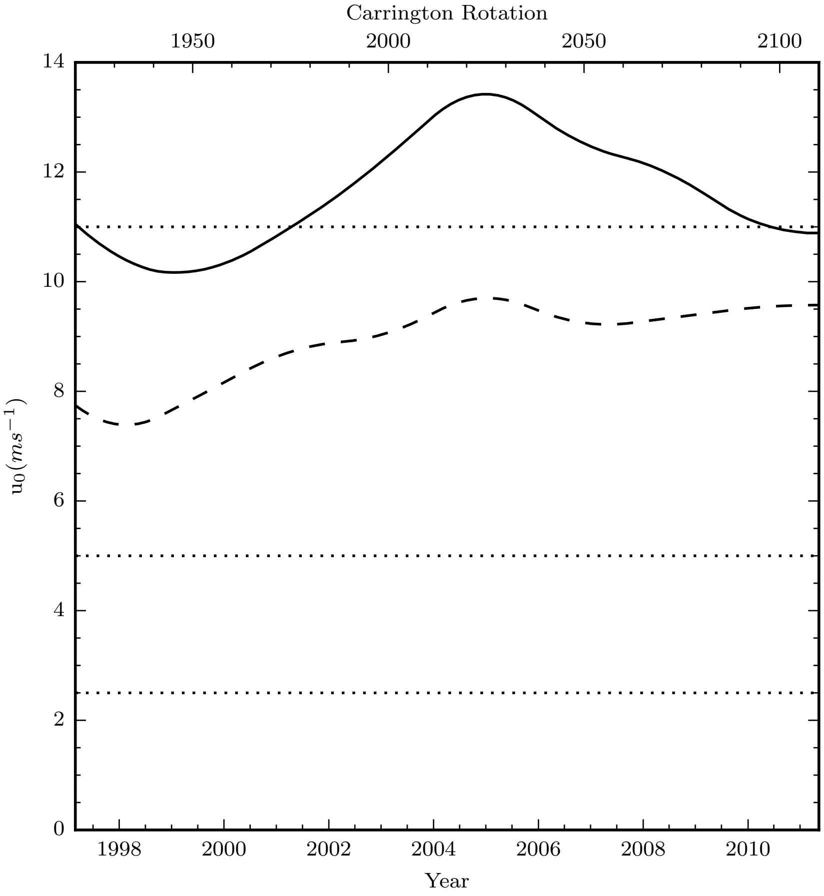

Figure 4.5. Observational time-dependent meridional flow profile for the peak (solid) and the observed value at a latitude of 55-degrees (dashed). The constant values of 2.5, 5.0, and 11.0 m s^{-1} are displayed for comparison (dotted).

Note that the observed peak meridional flow value lies fairly close to 11.0 m s^{-1} near the beginning and end simulation times, a coincidence. This peak flow begins by dipping down to nearly 10.0 m s^{-1} around 2000, and then rising steadily to a peak of 13.2 m s^{-1} around 2005. From here, a nearly steady decline persists until the end of the simulation in 2011.

For the observational profile calculated from the value at 55-degrees latitude, the behavior is starkly different. Beginning around 7.7 m s^{-1}, the flow profile drops down to 7.2 m s^{-1} in mid-1998. A slightly bumpy rise leads to a peak value of 9.5 m s^{-1} in 2005. After this, there is a slight dip downward in the flow magnitude. However, the value remains fairly steady in comparison with the observational peak value.

Figure 4.6 displays the total photospheric unsigned open magnetic flux generated by the flux transport model. This flux is divided into the latitude zones bounded by ±55-degrees. For this set of model runs, the peak meridional flow amplitude was selected for each time-step of one Carrington rotation. This peak value was then coupled with the standard form of the flow used by this model. Varying over time, this meridional flow then drives the simulation forward in conjunction with other effects. The priorly used diffusion values of 450, 600, and 900 km^2 s^{-1} were selected once again to explore the role of diffusion with a time-dependent meridional flow. For comparison, latitudinally zoned photospheric open flux derived from WSO data is displayed (black).

For this set of simulations, the higher meridional flow results in behavior in the polar regions that resembles earlier uses of a static meridional flow amplitude of 11.0 m s^{-1}. With flux elements being pushed into polar regions before diffusion allows adequate consolidation of a dominant flux, the results open polar flux is quite low in comparison. For the case of low-latitude open flux, here we observe slightly differing behavior. During the periods $\mathcal{T}_I$, $\mathcal{T}_{II}$, and the first third of $\mathcal{T}_{III}$, the model computed flux lies mainly below WSO-derived open fluxes. In the last two-thirds of $\mathcal{T}_{III}$ and all of $\mathcal{T}_{IV}$, the generated open flux lies more in line with WSO values. During the second half of $\mathcal{T}_{III}$ and all of $\mathcal{T}_{IV}$, lowering diffusion values results in higher open fluxes at lower-latitudes, with the opposite effect in the polar regions. Higher diffusions result in flux consolidation earlier at lower-latitudes.

Figure 4.7 displays the total photospheric unsigned open magnetic flux, broken into the standard latitude zones demarcated by ±55-degrees. For this particular set of model runs, the observed meridional flow at 55-degrees was used to compute a model input meridional flow. The diffusion values were varied across the standard set of 450, 600, and 900 km^2 s^{-1} used previously. Again, for comparison, the latitudinally zoned photospheric open flux derived from WSO data is displayed (black) for comparison.

In comparison with the meridional flow profiles derived from peak observed values, the overall lower flow values result in a higher open flux within the polar regions. This is to be expected, as the overall lower amplitude in flow results in a higher polar open

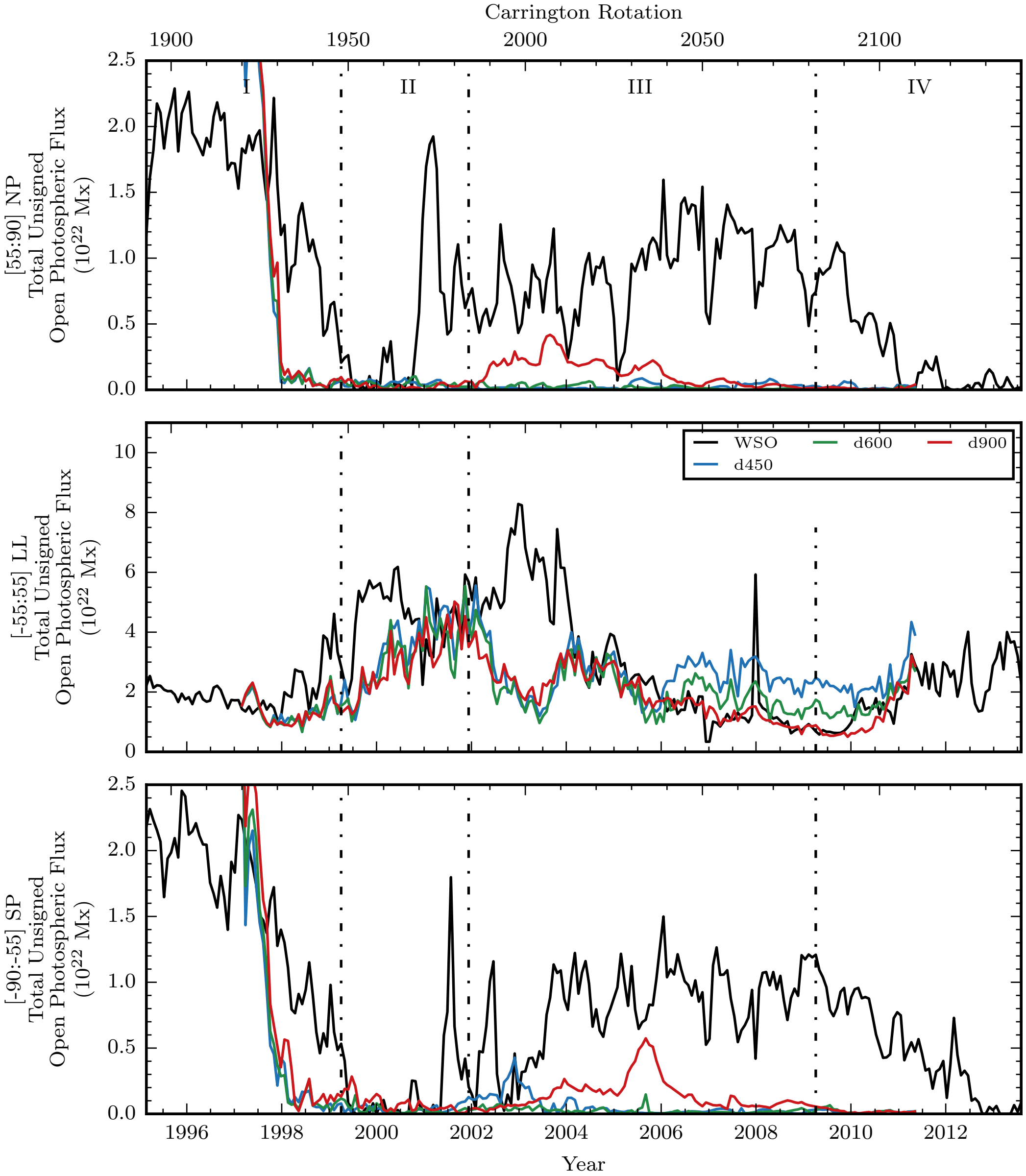

Figure 4.6. Total photospheric unsigned open magnetic flux, calculated from the flux transport model, using the peak observed meridional flow. Comparison is made with calculated total unsigned photospheric flux from WSO data, input into our PFSS calculation. Several combinations of diffusion coefficient and meridional flow velocity.

flux for previously discussed reasons. Here, however, the drop in flow results in curious behavior in low-latitude regions. Here, during $\mathcal{T}_I$, $\mathcal{T}_{II}$, and the first half of $\mathcal{T}_{III}$ the low-latitude unsigned open flux remains largely unchanged. The majority of change in behavior occurs during the second half of $\mathcal{T}_{III}$ and $\mathcal{T}_{IV}$. Here, the open flux is reduced, better matching our WSO data.

In comparison with the time-dependent meridional flow profiles over time, the shift becomes apparent. While both the peak and 55-degrees derived flow profiles share similar behavior in rise and falls from 1997 until 2005, here the behavior diverges. While the peak flow begins a decline back from a maximum value, the 55-degree value continues along reasonably steadily. As the effects of these changes to the flow can take multiple rotations to propagate their affects into the polar regions, the long-term evolution of these flows are of primary importance.

With these modifications to the meridional flow profile over time through the simulation, light is shed on the influence of this factor on the resulting field and open/closed configuration. Clearly, to match observations of surface flows a model time-dependent flow is required. However, the nature of how best to match these two is a subject of careful consideration. Beginning with a matching of the peak observed meridional flow value over time, the resulting polar open fluxes are far too low in comparison with WSO data. Through the modification to match meridional flows at 55-degrees, the behavior of the open flux distribution changes in a unique way. Polar open fluxes rise closer to observed values in comparison, without a major modification to the low-latitude open flux. With a time-independent meridional flow profile, changes to the flow amplitude resulted in a mismatch between latitude zones. Attempting to fix one zone would result in a severe change to other latitude zones. Through the introduction of a time-dependent meridional flow profile, a portion of this problem appears to have been alleviated. More careful modification of this profile over time suggests the ability to hone a set of parameters to best match our model results to observationally-driven data.

Conclusions

A flux transport model was developed and employed to explore the evolution of computed open magnetic flux over a comparable timespan to coronal hole observations. Both our coronal hole observations and flux transport model computed open field use as a comparison our potential field open flux, driven by WSO observations. This allows for a cross-comparison of our open flux / coronal-hole-enclosed-flux datasets, both observational and modeled.

By comparing the latitude-dependent open flux distribution from this model, we arrive at a unique opportunity to consider both the structural form and time-dependence of the meridional flow profile. Through comparison of modeled open flux

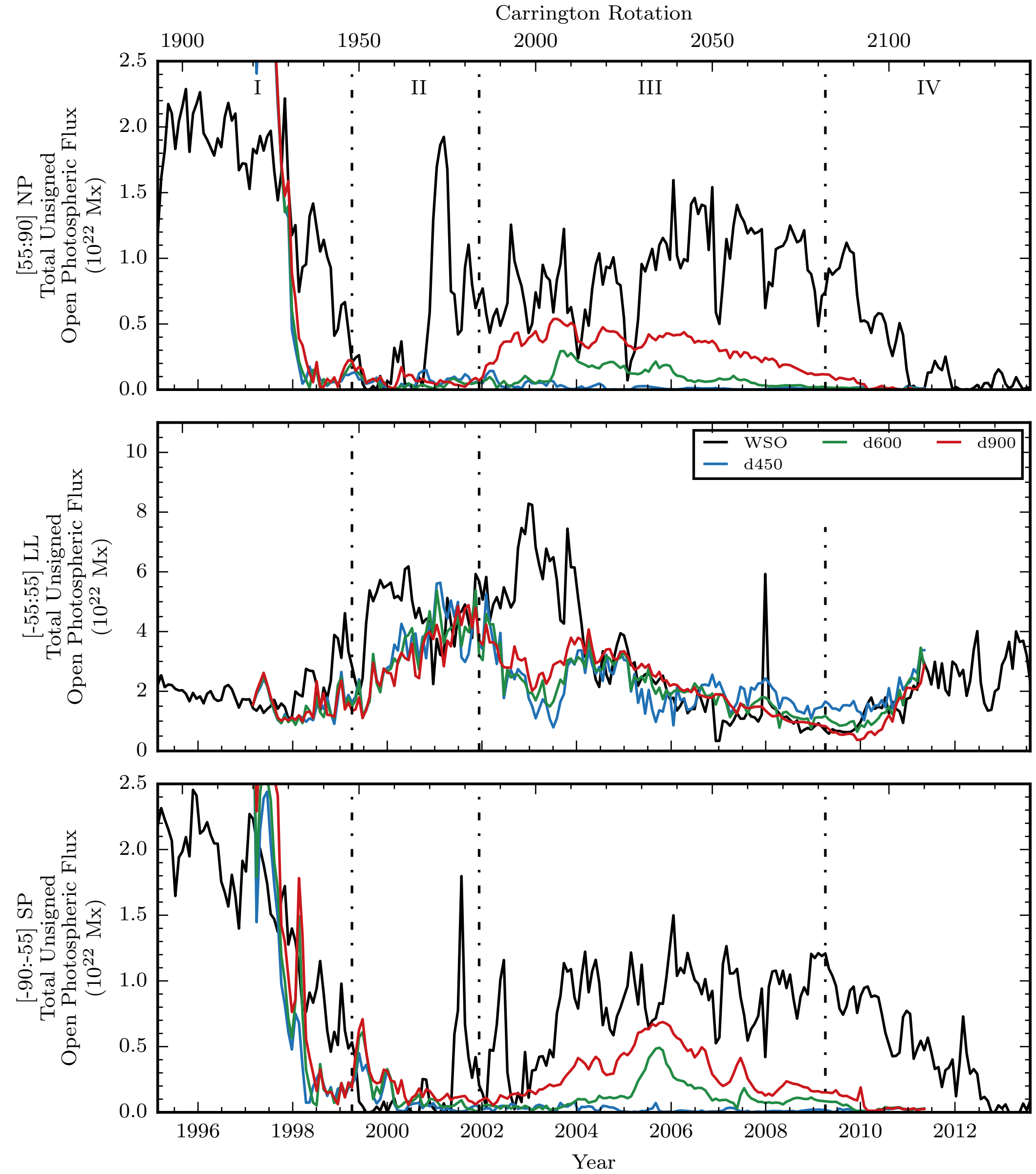

Figure 4.7. Total photospheric unsigned open magnetic flux, calculated from the flux transport model, using the observed meridional flow at 55-degrees latitude. Comparison is made with calculated total unsigned photospheric flux from WSO data, input into our PFSS calculation. Several combinations of diffusion coefficient and meridional flow velocity.

with observational-driven calculations, we see that the meridional flow profile plays the dominant role in differentiating the distribution of open flux.

The evolution of polar open flux is of particular interest. Significant agreement is found in the evolution of polar open flux, both from WSO potential open field and coronal hole enclosed flux, when compared with particular flux transport model runs. A lower meridional flow profile magnitude of 2.5 m s^{-1} coupled with a relatively low diffusion of 450 or 600 km^2 s^{-1} provides the best agreement. While this model parameter set best matches the measured polar open magnetic flux, this particular combination results in an overshooting in low-latitude open magnetic flux during the declining phase of cycle 23. For the low-latitude zones, a higher meridional flow profile of 11 m s^{-1} best matches WSO data. However, this higher meridional flow profile results in model polar open magnetic flux being nearly completely killed off. Considering the meridional flow profile of 5 m s^{-1}, lying between the two extrema here, the resulting modeled open flux in both polar and low-latitude regions fails to match observed values. Although this medium flow speed may produce both a good fit of the total open flux and a best overall fit for the calculated dipole moment, it does fail to produce a reasonable representation of the latitude-dependent flux. Therefore, results from these experiments point to the need to re-adjust the meridional flow profile to boost speeds at lower latitudes while reducing speeds near the poles.

Furthermore, in comparing our meridional flow profile with observational time-dependent measures, we see much less variation in higher latitudes above 55-degrees. Most of the time-dependent variation occurs at lower latitudes, below 55-degrees. This result suggests that the flow, particularly in low-latitudes, could have a time-dependent component.

The observed flow profiles by Upton & Hathaway (2014), displayed in Figure 4.1, in effect allow this very compromise, with a flow peak shifted equatorward, allowing for higher flow at low-latitudes and similar polar flows. The meridional flow profile employed in this study has a peak at 45-degrees, with observed peaks around 35-degrees. Observed magnitudes show a much higher meridional flow in lower latitudes than at the pole. As comparisons of latitudinal open flux would suggest, this higher flow at lower-latitudes, coupled with lower flows at higher latitudes, would result in a better match with WSO data. The observed flow profiles are also time-dependent with a larger variation in the low-latitude flow amplitude during the solar cycle, consistent with the suggestion from our model experiments.

The introduction of a time-dependent meridional flow profile results in some stark changes to the behavior of the model open flux throughout the course of the simulation. Through matching the peak observational meridional flow, the modeled open flux in low-latitudes reasonably matches observations, with a deficiency in the polar regions. However, by adjusting the model meridional flow to match the observed values at 55-degrees, polar open fluxes rise, without majorly adjusting the low-latitude open fluxes. Adjusting one latitude-zone without affecting the others was the primary issue observed with a time-independent meridional flow profile. This result suggests that further refinement of a time-dependent model meridional flow will result in a open flux distribution in better agreement with reality.

CONCLUSIONS AND FUTURE WORK

Conclusions

Considering the work outlined in the prior chapters, there are a few points of particular note.

For the first time, systematic observation and characterization of coronal holes and open flux evolution over the entire solar disk exists, with a database spanning back over nearly two complete solar activity cycles. This alone proves a powerful tool for the comparison of modeled open magnetic flux over the range of solar variability. Through the combination of AIA/EUVI data we find an added bonus, more complete coverage of the solar surface. For observations of solar cycle 24, not only do we have more complete coverage of heliographic longitude, enabling study of the far-side evolution of coronal holes, but also polar coverage is greatly enhanced. These more complete measurements allow the back-calibration of our EIT dataset, filling in the gaps in observations. Furthermore, in comparison with prior observations of coronal hole databases, particularly the polar studies by Harvey & Recely (2002), agreement is found in overlapping time-spans.

Through these observations, we observe and confirm details of the polar evolution of coronal holes throughout the solar activity cycle. Polar coronal holes peak in area and enclosed flux during the lulls of solar magnetic activity. However, here we present the evolution of low-latitude coronal holes throughout the cycle in far more detail. As a whole, coronal hole enclosed open flux peaks in low-latitudes during periods of higher solar activity, mirroring this cycle. Systematic observations reveal the migration of low-latitude coronal holes towards the polar regions, establishing a dominant polar coronal hole and swapping polarity with the old cycle. Details presented here outline the nature of this process, particularly the asymmetry observed in this reversal.

With these observational data in hand, comparison with models of the global coronal magnetic field prove the next logical step. Through the use of a flux transport model to drive the global photospheric field, this boundary condition was used as input for a potential field source surface model to calculate the global coronal field between 1 $R_\odot$ and 2.5 $R_\odot$. This global field was then used to trace down the footprints of open magnetic field lines. Using this detailed information about not only the total open flux, but also the latitudinal dependence of this open flux, critical details were uncovered throughout the course of the solar cycle. Through exploring the parameter space of this model, we show that through the standard meridional flow profiles employed in the field, large discrepancies exist between the computed and observed open fluxes and polar and low-latitudes. By selecting meridional flow parameters that match polar open magnetic flux, low-latitude open fluxes are entirely incorrect. By then attempting to match open flux within low-latitudes, all semblance of reality at the polar regions is lost. The introduction of a time-dependent meridional flow suggests a solution to this coupled behavior. This clearly motivates the need to further consider the nature of the meridional flow with regard to best matching open magnetic flux across all latitudes.

Future Work

While observations here were completed at 24 and 12-hour cadence for EIT and AIA/EUVI, respectively, this routine is capable of analyzing coronal hole boundaries at a much higher time-cadence, down to the native instrument cadence. Detailed observations in a higher cadence over a few select rotations would provide a unique look at the evolution of far-side and low-latitude open flux. These two areas can provide details into discrepancies in measured flux from these regions.

While studies of OMNI and Ulysses data suggest that measurement of the IMF from a single location at L1 provide a uniform picture of the radial field strength at 1 AU as a whole, there is perhaps more detail here to uncover. In particular, more detailed studies in comparing polar and low-latitude open field might shed some light on the uniformity of this field as it extends into the heliosphere.

In comparing our observations with models of open magnetic field, there are a few avenues of improvement. Modification of the meridional flow profile seems the first step, with the introduction of a time-dependent component. This better matches observations of the flow itself, and provides a better tool for matching open flux across the entire solar surface, and not just at the poles. Further efforts with employing non-potential models will be employed, especially regarding high-cadence studies.

With regard to the future of solar cycle 24, much is unknown. While our observations of coronal hole activity span a good portion of this cycle, a large chunk remains unobserved. With far-side data from *STEREO* data being temporarily unavailable, and the future of one of the spacecraft unknown, this dataset was truncated at this particular time. Extending data beyond this point is certainly possible, and observations of the declining phase of cycle 24 are possible, even with only one functional *STEREO* spacecraft. While these observations are possible, they will require more careful consideration and calibration, especially during the period of reduced far-side observations. Nevertheless, extending coronal hole observational coverage to include a further portion of cycle 24 would be a valuable asset.

REFERENCES CITED

Antiochos, S. K., Linker, J. A., Lionello, R., et al. 2012, SSRv, 172, 169

Antiochos, S. K., Mikic, Z., Titov, V. S., Lionello, R., & Linker, J. A. 2011, ApJ, 731, 112

Aschwanden, M. J., Nitta, N. V., Wuelser, J.-P., et al. 2009, ApJ, 706, 376

Balogh, A., Beek, T. J., Forsyth, R. J., et al. 1992, A&AS, 92, 221

Baumann, I., Schmitt, D., Schüssler, M., & Solanki, S. K. 2004, A&A, 426, 1075

Broussard, R. M., Tousey, R., Underwood, J. H., & Sheeley, N. R. J. 1978, SoPh, 56, 161

Cranmer, S. R. 2009, LRSP, 6, 3

de Toma, G. 2011, SoPh, 274, 195

Delaboudinière, J. P., Artzner, G. E., Brunaud, J., et al. 1995, SoPh, 162, 291

Freeland, S. L., & Handy, B. N. 1998, SoPh, 182, 497

Gallagher, P. T., Phillips, K. J. H., Harra-Murnion, L. K., & Keenan, F. P. 1998, A&A, 335, 733

Hale, G. E. 1908, ApJ, 28, 315

Hale, G. E., Ellerman, F., Nicholson, S. B., & Joy, A. H. 1919, ApJ, 49, 153

Harvey, J. W., & Sheeley, N. R. J. 1979, SSRv, 23, 139

Harvey, K. L., & Recely, F. 2002, SoPh, 211, 31

Hathaway, D. H., & Rightmire, L. 2010, Science, 327, 1350

Hoeksema, J. T. 1984, PhD thesis, Stanford Univ., 5

Hoeksema, J. T., Wilcox, J. M., & Scherrer, P. H. 1983, JGR, 88, 9910

Howard, R. A., Moses, J. D., Vourlidas, A., et al. 2008, SSRv, 136, 67

Huber, M. C. E., Foukal, P. V., Noyes, R. W., et al. 1974, ApJL, 194, L115

Jiang, J., Cameron, R. H., Schmitt, D., & Schüssler, M. 2011, SSRv, 176, 289

Kahler, S. W., Davis, J. M., & Harvey, J. W. 1983, SoPh, 87, 47

King, J. H., & Papitashvili, N. E. 2005, JGRA, 110, 2104

Krista, L. D., & Gallagher, P. T. 2009, SoPh, 256, 87

Leighton, R. B. 1964, ApJ, 140, 1547

Lemen, J. R., Title, A. M., Akin, D. J., et al. 2012, SoPh, 275, 17

Lepri, S. T., Antiochos, S. K., Riley, P., Zhao, L., & Zurbuchen, T. H. 2008, ApJ, 674, 1158

Levine, R. H. 1982, SoPh, 79, 203

Liu, Y., Hoeksema, J. T., Scherrer, P. H., et al. 2012, SoPh, 279, 295

Lockwood, M. 2002, in In: Proceedings of the SOHO 11 Symposium on From Solar Min to Max: Half a Solar Cycle with SOHO, 507–522

Lowder, C., Qiu, J., Leamon, R., & Liu, Y. 2014, ApJ, 783, 142

Luhmann, J. G., Li, Y., Arge, C. N., Gazis, P. R., & Ulrich, R. 2002, JGRA, 107, 1154

Mackay, D., & Yeates, A. 2012, LRSP, 9, 6

Mackay, D. H., Priest, E. R., & Lockwood, M. 2002a, SoPh, 207, 291

—. 2002b, SoPh, 209, 287

Malanushenko, O. V., & Jones, H. P. 2005, SoPh, 226, 3

Maunder, E. W. 1904, MNRAS, 64, 747

McComas, D. J., Elliott, H. A., Gosling, J. T., et al. 2002, GeoRL, 29, 1290

McIntosh, S. W., Leamon, R. J., Gurman, J. B., et al. 2013, ApJ, 765, 146

McIntosh, S. W., Wang, X., Leamon, R. J., et al. 2014, ApJ, 792, 12

McIntosh, S. W., Leamon, R. J., Krista, L. D., et al. 2015, Nature Communications, 6, 6491

Miralles, M. P., Cranmer, S. R., & Kohl, J. L. 2001, ApJL, 560, L193

Neugebauer, M., Liewer, P. C., Smith, E. J., Skoug, R. M., & Zurbuchen, T. H. 2002, JGRA, 107, 1488

Neugebauer, M., Forsyth, R. J., Galvin, A. B., et al. 1998, JGR, 103, 14587

Parker, E. N. 1958, ApJ, 128, 664

Petrie, G. J. D., & Haislmaier, K. J. 2013, ApJ, 775, 100

Priest, E. 2014, Magnetohydrodynamics of the Sun

Riley, P. 2007, ApJL, 667, L97

Rotter, T., Veronig, A. M., Temmer, M., & Vršnak, B. 2012, SoPh, 281, 793

Rust, D. M. 1983, SSRv, 34, 21

Schatten, K. H., Wilcox, J. M., & Ness, N. F. 1969, SoPh, 6, 442

Scherrer, P. H., Bogart, R. S., Bush, R. I., et al. 1995, SoPh, 162, 129

Scherrer, P. H., Schou, J., Bush, R. I., et al. 2012, SoPh, 275, 207

Schrijver, C. J., & De Rosa, M. L. 2003, SoPh, 212, 165

Schwabe, M. 1844, Astronomische Nachrichten, 21, 233

Shearer, P., Frazin, R. A., Hero, A. O. I., & Gilbert, A. C. 2012, ApJL, 749, L8

Sheeley, N. R. J. 1980, SoPh, 65, 229

Snodgrass, H. B. 1983, ApJ, 270, 288

Spruit, H. C. 2011, The Sun, 39

Sun, X., Liu, Y., Hoeksema, J. T., Hayashi, K., & Zhao, X. 2011, SoPh, 270, 9

Thompson, B. J., Cliver, E. W., Nitta, N., Delannée, C., & Delaboudinière, J. P. 2000, GeoRL, 27, 1431

Thompson, M. J., Toomre, J., Anderson, E. R., et al. 1996, Science, 272, 1300

Timothy, A. F., Krieger, A. S., & Vaiana, G. S. 1975, SoPh, 42, 135

Tousey, R., Sandlin, G. D., & Purcell, J. D. 1968, Structure and Development of Solar Active Regions. Symposium no. 35 held in Budapest, 35, 411

Upton, L., & Hathaway, D. H. 2014, ApJ, 780, 5

van Ballegooijen, A. A., Priest, E. R., & Mackay, D. H. 2000, ApJ, 539, 983

Wang, Y. M. 2009, SSRv, 144, 383

Wang, Y.-M., Hawley, S. H., & Sheeley, N. R. J. 1996, Sci, 271, 464

Wang, Y. M., Lean, J., & Sheeley, N. R. J. 2002, ApJ, 577, L53

Wang, Y. M., Nash, A. G., & Sheeley, N. R. J. 1989, Sci, 245, 712

Wang, Y. M., Robbrecht, E., & Sheeley, N. R. J. 2009, ApJ, 707, 1372

Wang, Y. M., & Sheeley, N. R. J. 1992, ApJ, 392, 310

Webb, D. F., Davis, J. M., & McIntosh, P. S. 1984, SoPh, 92, 109

Yang, L.-H., Jiang, Y.-C., & Ren, D.-B. 2008, ChJAA, 8, 329

Yeates, A. R. 2013, SoPh, 152

Yeates, A. R., Mackay, D. H., & van Ballegooijen, A. A. 2007, SoPh, 245, 87

Yeates, A. R., Mackay, D. H., van Ballegooijen, A. A., & Constable, J. A. 2010, JGR, 115, 9112

Zhao, L., & Landi, E. 2014, ApJ, 781, 110

Zirker, J. B. 1977, RvGSP, 15, 257